Engineering of Nano Cavities for Quantum Light Sources

Wang, Yujing

Publication date:
2023

Document Version
Publisher's PDF, also known as Version of record

Doctor of Philosophy
Doctoral thesis in Photonics Engineering

DTU ELECTRO
Department of Electrical and Photonics Engineering

Engineering of Nano Cavities for Quantum Light Sources

Yujing Wang

DTU

Project period: August 2020 - July 2023
Supervisor: Prof. Niels Gregersen
Co-supervisors: Assis. Prof. Luca Vannucci & Dr. Sven Burger
Contact: yujingwang19@outlook.com

DTU Elektro
Department of Electrical and Photonics Engineering
Technical University of Denmark
Ørsteds Plads
Building 343
2800 Kongens Lyngby, Denmark

Preface

This thesis is submitted as partial fulfillment of the requirements for a Ph.D. degree. The project was conducted in the Quantum Light Sources group at the Department of Electrical and Photonics Engineering at the Technical University of Denmark (DTU). The study was supervised by Prof. Niels Gregersen, Assis. Prof. Luca Vannucci, and non-local supervisor Dr. Sven Burger from JCMwave, Zuse Institute Berlin (ZIB).

This Ph.D. project was funded by the European Union's Horizon 2020 Research and Innovation Programme under the Marie Sklodowska-Curie Grant Agreement No. 861097, QUDOT-TECH project.

Three times external research and academic visits were separately completed in Prof. Stephan Reitzenstein's group at the Technical University of Berlin (TUB) in October and November 2021, in Dr. Sven Burger's group at ZIB and JCMwave company in May 2022, and in Dr. Jean-Michel Gérard and Dr. Julien Claudon's group at CEA Grenoble in June 2022.

The QUDOT-TECH project aims to build a fully integrated photonic chip for quantum information processing. This Ph.D. project focuses on the "source" of this problem: a highly efficient single-photon source.

Kongens Lyngby, 30$^{\text{th}}$ July 2023

Yujing Wang

Abstract

As a basement for quantum computing, quantum cryptography, and quantum information processing, the research on a quantum dot (QD)-based, highly-efficient single-photon source (SPS) becomes the main topic of this thesis. Although this Ph.D. project is entirely based on numerical analyses, we still consider the experimental perspectives and aim to propose beneficial cavity designs contributing to more excellent SPSs.

The first part of this thesis is devoted to illustrating the motivation of our work by introducing the applications and requirements for SPSs, the superior properties and challenges of QDs, the implementation of nano-cavities for the improvement of SPS, and the importance of emission tuning and charge control for realizing the SPSs with more practical values. The main methods adopted to analyze the physical problems in our works are also disclosed in this part in a general way.

At the start of the central part, three types of vertical-emission SPSs are investigated. We propose a design procedure for the nanopost cavity and discuss the spatial misalignment of the emitter. We also explain the asymmetric behavior that appears on the spectrum. To get a high-quality cavity, our attention is turned to the new-type bullseye structures, where we demonstrate the optimization strategies in the hole-bullseye device and apply the optimizer to a chirped-bullseye cavity. The last vertical-emission device is developed in a fiber-coupled tunable open double cavity, which consists of a bottom planar cavity and a top metal/dielectric mirror. The suitable cavity length is selected to provide a Gaussian-like far-field profile, aiming for a reasonable single-mode fiber collection efficiency.

The second section is launched from a design procedure for the champion nanobeam cavity with a near-unity on-chip coupling efficiency. The problems in the cavity design in scale-up waveguides are appropriately analyzed and solved, according to which other fabrication-tolerant cavities are carried out. Collaborating with the experimental Ph.D. student in the MSCA QUDOT-TECH project, we implement the superconducting single-photon detector to the on-chip waveguide and provide our predictions of detector length via numerical simulations.

Finally, from a realistic consideration, the electrical contact strategies for QD emission tuning and charge environment stabilization are investigated in different nano-cavities, including Micropillar, bullseye, nanopost, and on-chip nanobeam structures. We provide perspectives on the impacts of additional sections for implementing the contacts in the abovementioned nano-cavities on the SPS performances.

Resumé

Hovedemnet for denne afhandling er højeffektive kvantepunktbaserede enkeltfotonkilder (EFK'er), som udgør fundamentet for kvantecomputere, kvantekryptografi og kvanteinformation. Selvom dette ph.d. projekt udelukkende er baseret på numeriske analyser, vil vi stadig tage de eksperimentelle perspektiver i betragtning og sigte mod at foreslå gavnlige kavitetsdesign, der bidrager til fremragende EFK'er.

Den første del af denne afhandling er viet til at illustrere motivationen af vores arbejde ved at introducere anvendelserne af EFK'er, kravene til EFK'er, de overlegne egenskaber samt udfordringer ved kvantepunkter, implementeringen af nanokaviteter til forbedring af EFK'er og vigtigheden af emissionsafstemning og ladningskontrol for at realisere EFK'er til praktiske formål. De vigtigste metoder, der anvendes til at analysere de fysiske problemer i vores arbejde, er også generelt beskrevet i denne del.

I starten af den centrale del af afhandlingen undersøges tre typer EFK'er med vertikal emissionsretning. Vi foreslår en designprocedure for nanopost-kaviteten og diskuterer den rumlige forskydning af emitteren. Vi forklarer også den asymmetriske opførsel, der optræder på spektret. For at opnå en kavitet af høj kvalitet er vores opmærksomhed rettet mod den nye type bullseye-strukturer, hvor vi demonstrerer optimeringsstrategierne for hul-bullseye-strukturen og anvender optimeringsstrategien på en chirped-bullseye-kavitet. Den sidst undersøgte struktur med vertikal emission er udviklet i en fiberkoblet afstembar åben dobbelt-kavitet, som består af en plan kavitet i bunden og et metal/dielektrisk spejl øverst. Den passende kavitetslængde er valgt til at give en Gaussisk-lignende fjernfeltprofil, der sigter mod en hæderlig opsamlingseffektivitet til en enkelt-mode fiber.

Den anden sektion af afhandlingen lancerer en designprocedure for den mesterlige nanobjælke-kavitet med en on-chip koblingseffektivitet på næsten 1. Problemerne for opskaleringen af bølgeleder-kavitetsdesigns er passende analyseret og løst, hvorefter andre fremstillingstolerante kaviteter præsenteres. I samarbejde med den eksperimentelle ph.d.-studerende i MSCA QUDOT-TECH-projektet implementerer vi den superledende enkeltfoton-detektor til on-chip bølgelederen og giver vores forudsigelser af detektorlængden via numeriske simuleringer.

Til sidst vil vi ud fra en realistisk betragtning undersøge de elektriske kontakt strategier for kvantepunkts emissionsafstemning og ladningsmiljøstabilisering i forskellige nanokaviteter, herunder mikrosøjle-, bullseye-, nanopost- og on-chip nanobjælkestrukturene. Vi giver perspektiver på virkningerne af yderligere sektioner til implementering af kontakterne i de ovennævnte nanokaviteter på EFK-præstationen.

Acknowledgments

In the first place, I would like to express my sincere gratitude to my supervisors, Niels Gregersen, Luca Vannucci, and Sven Burger. All the valuable meetings, discussions with Niels and Luca, and their insightful suggestions gave me incredible power and support when I felt bewildered by the research. Special thanks to Niels for his guidance at every stage of the project. Likewise, I'm profoundly grateful to Sven, who always provided inspiring help to my study, and for hosting me during the secondment in ZIB.

It's also my great pleasure to work with Jean-Michel Gérard and Julien Claudon, not only during my external stay at CEA but also in our close collaborations. In addition, I would like to extend my sincere thanks to Stephan Reitzenstein for hosting me at TUB, where I had the great opportunity to learn the knowledge of fabrication and characterization.

I would like to take the chance to thank Ditte Wachs, and Leah Strauss for their kind and heartwarming help before and during my study at DTU. I also wish to thank all my colleagues in Quantum Light Sources group, Battulga, Martin, Claudia, Abdulmalik, José, Christine, and Benedek for the precious moments and memory in my Ph.D. study. Specially thank Battulga and Claudia for their effort and valuable contributions to our collaborative work. My special appreciation also goes to Martin, not only for translating the Danish abstract for this thesis but also for his kind help throughout my Ph.D. study.

I want to appreciate and also apologize to my parents. I appreciate their tremendous understanding and mental support, and I apologize for my absence when they suffered pain from the body or mind. Ultimately, I would like to thank the company of my girlfriend, Shuyi. I will never forget those days when she sacrificed sleep for me due to the time difference and when she traveled across the ocean to stay by my side.

List of publications

Journal publications presented in this thesis

- **Yujing Wang**, Luca Vannucci, Sven Burger, and Niels Gregersen. "Near-unity efficiency in ridge waveguide-based, on-chip single-photon sources." Materials for Quantum Technology 2.4 (2022): 045004.
- **Yujing Wang**, Claudia Piccinini, Martin Arentoft Jacobsen, Luca Vannucci, Sven Burger, Battulga Munkhbat, Niels Gregersen. "The tunable quantum-dot-based single-photon source: Strategies for implementing electrical contacts." Manuscript under preparation.
- Martin Arentoft Jacobsen, **Yujing Wang**, Luca Vannucci, Julien Claudon, Jean-Michel Gérard and Niels Gregersen. "Performance of the nanopost single-photon source: beyond the single-mode model." Nanoscale, 15 (2023), 6156-6169.
- Saptarshi Kotal, Alberto Artioli, **Yujing Wang**, Andreas Dyhl Osterkryger, Matteo Finazzer, Romain Fons, Yann Genuist, Joël Bleuse, Jean-Michel Gérard, Niels Gregersen and Julien Claudon. "A nanowire optical nanocavity for broadband enhancement of spontaneous emission." Applied Physics Letters 118.19 (2021): 194002.

Journal publications not presented in this thesis

- Uğur Meriç Gür, Yuhui Yang, Johannes Schall, Ronny Schmidt, Arsenty Kaganskiy, **Yujing Wang**, Luca Vannucci, Michael Mattes, Samel Arslanagić, Stephan Reitzenstein and Niels Gregersen. "Design and fabrication of ridge waveguide-based nanobeam cavities for on-chip single-photon sources." Optics Express 30.7 (2022): 11973-11985.

Contributions to the conferences

- **Yujing Wang**, Andreas Dyhl Østerkryger, Julien Claudon, Jean-Michel Gérard and Niels Gregersen. "Strong Purcell Enhancement in a "Nanopost" Single-Photon Source." 2021 Conference on Lasers and Electro-Optics (CLEO), Poster. Published in CLEO: QELS_Fundamental Science (pp. JW1A-124).
- **Yujing Wang**, Luca Vannucci, Sven Burger and Niels Gregersen. "How to achieve near-unity coupling efficiency in on-chip single photon source." Oral presentation at 15th Annual Meeting Photonic Devices (AMPD2022).
- **Yujing Wang**, Luca Vannucci, Sven Burger and Niels Gregersen. "Highly efficient on-chip single photon sources." WE-Heraeus Seminar on Photonic Quantum Technologies, Poster.
- **Yujing Wang**, Claudia Piccinini, Battulga Munkhbat, Luca Vannucci and Niels Gregersen. "Electrical Contact Strategies Applied to Micropillar Single Photon Sources." BENASQUE Quantum Nanophotonics 2023, Poster.
- **Yujing Wang**, Luca Vannucci, Sven Burger and Niels Gregersen. "Design and simulations of a highly efficient on-chip SPS." Oral presentation at QUDOT-TECH & QCLUSTER workshop, Paris, 2023.

Abbreviations

BCB	Benzocyclobutene
BS	Beam splitter
CBG	Circular Bragg grating
DA	Dipole approximation
DBR	Distributed Bragg reflector
FEM	Finite element method
FMM	Fourier modal method
FWHM	Full width at half maximum
HBT	Hanbury Brown and Twiss
HOM	Hong–Ou–Mandel
ITO	Indium tin oxide
LDOS	Local density of states
MBE	molecular beam epitaxy
NA	Numerical aperture
PC	Photonic crystal
PML	Perfectly matched layers
PSB	Phonon side band
QCSE	Quantum-confined Stark effect
QD	Quantum dot
QLS	Quantum light source

QNM	Quasi-normal modes
SE	Spontaneous emission
SEM	Scanning electron microscope
SMF	Single-mode optical fiber
SMM	Single modal method
SNSPD	superconducting nanowire single photon detector
SPS	Single photon source
TE	Transverse electric
TM	Transverse magnetic
ZPL	Zero phonon line

Contents

Part I

Background and methodologies

CHAPTER 1

Introduction

1.1 Quantum light sources and applications

Quantum light sources, especially the on-demand Single photon source (SPS)s have already been reckoned as one of the most vital components in the applications of quantum computing [1–4], quantum communication network [5–7], quantum metrology [8, 9], and quantum cryptography [10–12]. Contrary to coherent light sources and thermal light sources, the basic definition of SPS is a source that can only emit one photon or particle within a time interval [13]. The difference between the three types of light sources regarding the photon separation in time is depicted in Fig.1.1, where thermal light tends to emit in bunching, while the strength distribution of coherent light is caused by interference. Then why is the SPS of such importance and what are the requirements for it in quantum applications?

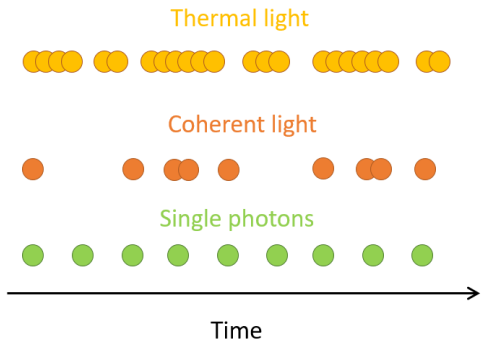

Figure 1.1. Photon separation displayed in time in three types of light sources

Here, we take quantum computing as an example to demonstrate the functional role of single photons. The quantum bit or qubit is the most fundamental element that can carry the information in quantum computing. Thanks to the quantum superposition property, a quantum computer is able to perform the calculations in parallel by producing the superposition states for all the

possible results. Compared to the linear switch of 0 or 1 in classical computers, a "knob-type" switch in quantum computers [14, 15] enables an exponential improvement in saving computational time. The single photon is a promising candidate due to its naturally weak interaction with the surrounding environments, thus leading to good protection from decoherence [16], which is known to be harmful to the quantum computing success rate.

Thus we are brought to the first requirement of the SPS: single-photon purity, which can be characterized by Hanbury Brown and Twiss (HBT) experiment [17] with the setup shown in Fig.1.2. The photons generated from the source are separated by a 50/50 Beam splitter (BS) and independently travel toward the photon detectors D1 and D2. Then the coincidence of the two paths is measured as a function of the time delay τ. $\tau = 0$ means D1 and D2 detect a photon individually but simultaneously. Considering the requirement of a pure SPS, two photons should not trigger D1 and D2 simultaneously; thus, the coincidence measurement ideally equals zero at $\tau = 0$.

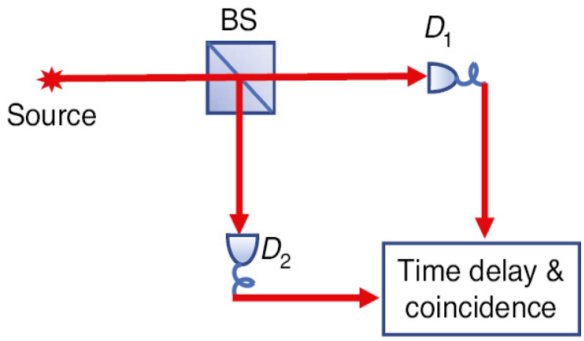

Figure 1.2. Sketch of the HBT experiment [17].

Two-photon interference effect or the so-called Hong–Ou–Mandel (HOM) effect is another crucial factor in quantum computations, without which the qubits are hard to communicate with each other [18]. The perfect fidelity of the interference highly requires a complete wave-packet overlap of the single photons at the BS [19], meaning that the two photons should be indistinguishable in terms of frequency, polarization, bandwidth, and arrival time.

The single photon indistinguishability is characterized by HOM experiment sketched in Fig.1.3, where $\Delta\tau$ describes the time interval between two single photons. After being transmitted or reflected by the first 50/50 BS, the two photons separately travel through two arms and then recombine at the second 50/50 BS. One premise of the interference is that $\Delta\tau$ is shorter than the

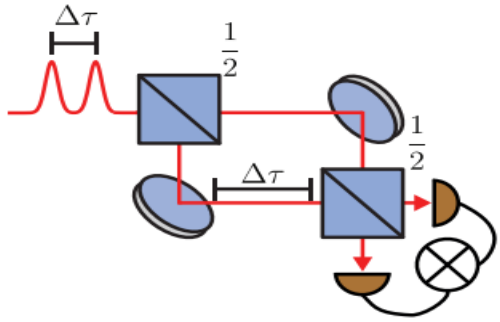

Figure 1.3. Sketch of the HOM experiment [16].

photon coherence time. The photons are expected to arrive simultaneously at the second BS since different path lengths in two arms are implemented to compensate $\Delta\tau$. If the two photons are distinguishable, then the possibility they finally trigger the same detector or different detectors is 50% for each. On the contrary, if they are indistinguishable photons, the destructive interference prevents the arrival at two separate detectors. Ultimately, the correlation measurement shows no coincidence at zero time delay.

Beyond the high requirements for single photon purity and indistinguishability, another obstacle to realizing linear and scalable optical quantum computing is the need for large amounts of single photons from highly efficient sources [1, 20, 21]. The success probability of N-photon quantum computation is evaluated by $P = (\epsilon\eta)^N$, where ϵ is the SPS efficiency and η is the indistinguishability. For a significant demand of photon number N, the success possibility will dramatically decrease if the product $\epsilon\eta$ is less than 1. The near-unity indistinguishability has already been demonstrated in many works [19, 22–27]. However, we are still eager for a comparable high value on source efficiency. In other quantum applications mentioned above, the performance requirements for SPSs can also be classified as high purity, high indistinguishability, and high efficiency or brightness.

1.2 Semiconductor quantum dot and its properties

As introduced in Chapter 1.1, high quality and high quantity SPSs are urgently needed to develop quantum technologies. Some of the candidates are 2D materials [28–30], nitrogen-vacancy centers in diamonds [31–33], and semiconductor Quantum dot (QD)s [34–37]. The material of our interest is the

semiconductor QD, which stands out with its features of narrow linewidth [38], high single photon purity [23], ease of integration with nano-cavities [27], and a good chance of being electronically controlled [39].

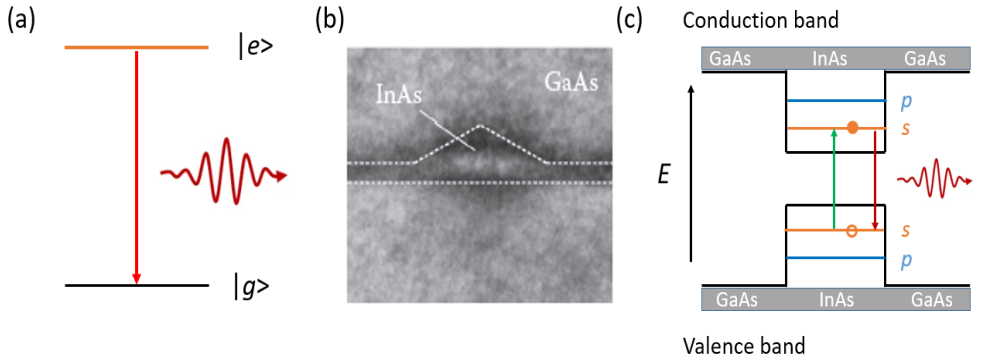

Figure 1.4. (a) Sketch of the energy level in a two-level system. (b) Cross-sectional Scanning electron microscope (SEM) image [40] and (c) the band diagram of the InAs QD.

The QD emitter can be reckoned as a two-level system consisting of a ground state $|g>$ and an excited state $|e>$, as depicted in Fig.1.4(a). The system initially stands at the ground state. Then the electron absorbs the energy from the excitation pulse and transitions to the excited state. After the spontaneous emission, the electron returns to the ground state and simultaneously emits a photon. Since the transition takes a certain amount of time, another electron will not occupy the excited state before the radiated photons return to the ground state, therefore, the photons produced by the two-level system are strictly single photons.

The semiconductor InAs/GaAs QDs discussed in this thesis are grown via Stranski-Krastenow molecular beam epitaxy (MBE). The lower bandgap material InAs is deposited on top of GaAs, which has a $\sim$7% lattice mismatch with InAs [41]. During the growing process, InAs adapt to the lattice mismatch by elastic deformation until the thickness of the grown InAs layer exceeds several monolayers. Then the stress is released by forming an island-like structure on the surface of GaAs, which is called the InAs QD [42], as visualized in Fig.1.4 (b). Since the lower bandgap material is encapsulated by higher bandgap material, the electronic confinement around the QD is formed from three dimensions. Thus the energy levels of the allowed states are discrete [43] in the QD band diagram depicted in Fig.1.4 (c), where the s state with the lowest energy in the conduction band is the mainly considered excited state.

Now let's look into what happens during the generation of single photons from the InAs QD. When the QD is resonantly excited by the laser pulse, the electron in the valence band will absorb the power and travel toward the s state in the conduction band, following the green arrow in Fig.1.4 (c) and leave a hole behind. The quantum confinement potential traps the electron and the hole, while the Coulomb potential between them forms an exciton. After the exciton is relaxed via the radiative process, indicated by the red arrow in Fig.1.4 (c), a photon is emitted. This is a rough and simple illustration of the single photon generation in QD. In reality, this process would be more complicated when introducing other excitation schemes, for instance, the phonon-assisted cascaded decay process [44–46] and p-shell excitation [47–49].

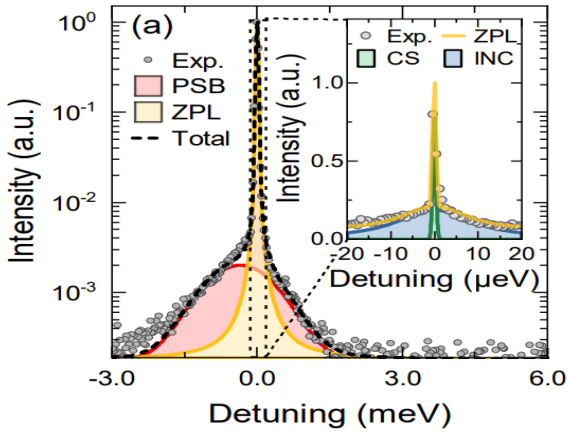

Figure 1.5. Spectrum of the QD emission [50], Exp. are the experimental data, PSB means the phonon side-band, ZPL is zero phonon line, CS and INC are the abbreviations of coherence scattering and incoherent resonance fluorescence, respectively.

Returning our attention to the requirements for the SPS, the QD-based system naturally promises a high purity. However, the bulk QD photon signal is weak. Thus, we need to consider the implementation of nano-cavities for larger photon collections, which is discussed in Chapter 3 and 4 in this thesis. On the other hand, photon indistinguishability from QD is negatively affected by two main factors. Here, the influences of the excitation scheme, for instance, the non-radiative decay in the phonon-assisted scheme is likely to reduce the photon purity and indistinguishability, are excluded.

The first main factor is the Phonon side band (PSB), visualized in the red area of Fig.1.5. Due to the funneling of QD to the lattice vibrations of the host material, even at cryogenic temperatures, phonon emissions are still hard to

avoid, and the corresponding PSB modifies the total spectrum. The dephasing induced by the interaction between photon and phonon is a primary source of decoherence [51–53], which is harmful to the single photon indistinguishability. Although the PSB is almost impossible to be entirely erased, increasing the Local density of states (LDOS) around the QD by the implementation of nano-cavities is considered an effective way to improve the proportion of photons emitting at the region within Zero phonon line (ZPL). The second main factor affecting indistinguishability is the interaction between QD and nuclear spins [54] or charge noise [55]. Such interaction hurts the coherence of the photons. Eventually, these noises bring a broadening phenomenon to the ZPL on the spectrum [40], which makes the photons distinguishable in terms of spectral distribution. Our investigations of implementing electric contacts to the SPSs displayed in Chapter 5 is a promising approach to reducing the spectral wandering caused by the lack of charge stabilization.

1.3 Different types of nano-cavities

In the past two decades, aiming for a higher quality SPS, integrating QDs with nano-cavities has become a research hotspot. We roughly classify these cavities in two directions: vertical emission and on-chip emission.

State-of-the-art Micropillar cavity is undoubtedly one of the strongest candidates in vertical emitted QD-based SPSs. The sketch of a standard Micropillar cavity is revealed in Fig.1.6 (a), which typically consists of a λ-cavity sandwiched by two asymmetric Distributed Bragg reflector (DBR) mirrors. In 2016, Somaschi *et al.* [26] realized a record-breaking Micropillar SPS revealing real near-unity indistinguishability of 0.9956, almost perfect single photon purity, and source efficiency of 15% with the help of electric contacts implementation. In the same year, Ding *et al.* [25] observed similarly excellent indistinguishability of 0.985 with an efficiency of 33%. Both results were carried out under the resonant excitation scheme, which is good for photon indistinguishability but limits the source efficiency. Due to the rotational symmetry in the standard Micropillar cavity, the horizontally (H) and vertically (V) polarized modes are equally coupled with the QD, meaning that half of the generated photons are filtered by the post-polarization-selection to ensure the photon indistinguishability. One possible solution is breaking the symmetry of the structure. In 2019, Wang *et al.* [23] proposed a reshaped elliptical Micropillar device, as depicted in Fig.1.6 (b). Such a structure led to a spectral separation of H and V modes. For instance, the elliptical device is designed to

couple with the QD at the H-mode while the emitter is resonantly excited by a V-polarized pulse. Although the V-photons are not entirely suppressed, the proportion of H-light is enhanced, leading to a 60% source efficiency [23] after filtering all the reflected excitation pulse and the small-portion V-polarized photons generated by the QD.

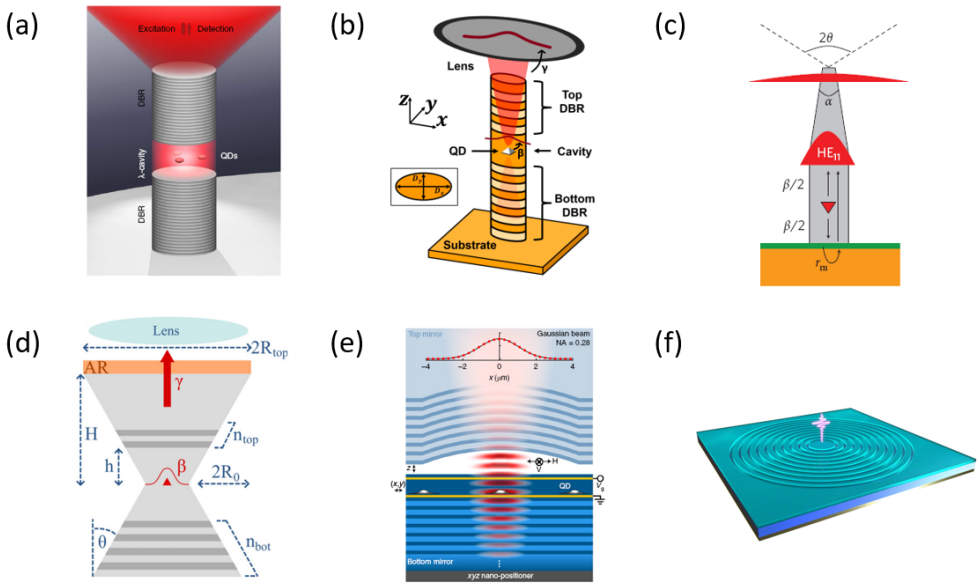

Figure 1.6. Sketches of nano-cavities supporting vertical emission of single photons. (a) Micropillar cavity [56], (b) Elliptical Micropillar cavity [57], (c) Needle nanowire cavity [58], (d) Hourglass cavity [59], (e) Open cavity [27], (f) bullseye Circular Bragg grating (CBG) cavity [60].

In the earlier stage, Claudon *et al.* [58] fabricated a needle-shape nanowire SPS, where the cavity was formed between the top air-facet and the bottom metal mirror, as indicated by the sketch in Fig.1.6 (c). The highlight of this work was the more straightforward fabrication excluding the growth of DBRs and an impressive source efficiency of 72% attributed to the dielectric screening effect, combined with pure single-photon emission under the non-resonant excitation. Inspired by this structure and the classical Micropillar cavity, Gaál *et al.* [59] proposed an hourglass device based on the asymmetric DBRs in 2022, sketched by Fig.1.6 (d). In such a device, the reduced radius in the cavity region was to optimize the dielectric screening effect [61, 62], while the planar extensions at the top and bottom areas were designed to focus the output beam and to ensure a solid bottom reflectivity, respectively. In

Chapter 3.1, we will introduce another nanowire-based simple but effective vertical emission SPS and discuss its unusual spectral property.

Considering the tunability of the cavity and the ease of positioning QDs, Tomm *et al.* [27] brought the open cavity SPS to the public. As visualized in Fig.1.6 (e), the top curved dielectric lens and the bottom planar DBR, which is beneath a very thin QD layer, made up the cavity. The tuning of cavity resonance and the searching for QDs were carried out by moving the top lens. This work demonstrated a 57% efficiency combined with indistinguishability of 0.97, which were both comparable to the champion performances in elliptical Micropillar device. A similar cavity also contributed to the collection of single photons produced by the emitters in 2D material monolayer [63]. In Chapter 3.3 we will present our perspectives on the open cavity designs and implement the fiber coupling simulations during the optimizations.

The last vertical emitted SPS introduced in this chapter is the well-known bullseye or so-called CBG cavity. As sketched in Fig.1.6 (f), the QD is embedded in the central disk, surrounded by the discrete outer rings. The bottom mirror beneath the disk and rings ensures the photons' upward propagation. In experiments, the record source efficiency of this fabrication-friendly cavity was 56%, realized by an elliptical modification to the CBG [23]. By careful design for the mesa height, the bullseye structure also enabled the coupling between cavity mode and the 2D material single photon emitter attached on top of a tiny pillar standing on the central disk [30]. In general, the broad bandwidth of the bullseye cavity allows more tolerance to the QD-cavity spectral misalignment. However, pursuing more near-unity indistinguishability, we are more interested in the new-type CBG [64] which is expected to strengthen the LDOS at the QD position while maintaining the robust vertical source efficiency. The corresponding designs and optimizations are discussed in Chapter 3.2.

Now we turn our attention to the on-chip SPSs. Almost all the candidates in this group are based on waveguide integration. State-of-the-art PC waveguide cavities (see Fig.1.7 (a)) [65, 68–71], can offer a near-unity source efficiency. However, the material loss prevents a straightforward extension to the large-scale PC chip [72]. One solution is embedding the QD into a semiconductor ridge waveguide, which features low propagation loss [73, 74] and another superiority on the selective guidance of photons with specific polarization orientation [75]. Applying this strategy, the coupling efficiency from an InAs QD to a bare GaAs ridge waveguide located on the top of a low-index silica substrate has achieved ∼60% [75]. More recently, researchers presented a

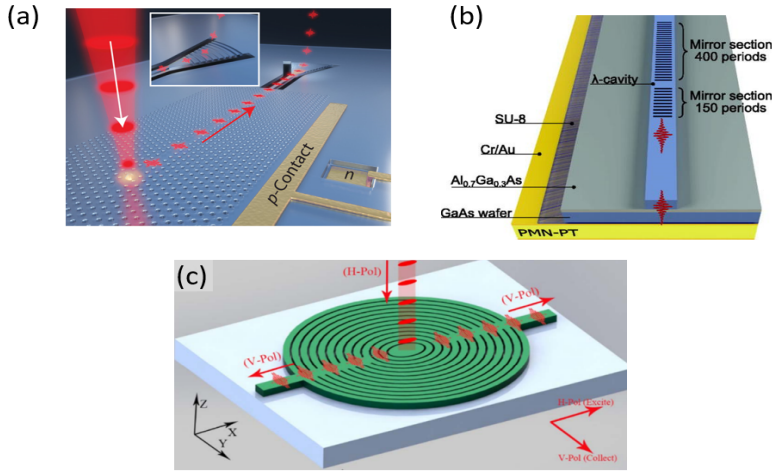

Figure 1.7. Sketches of nano-cavities supporting on-chip emission of single photons. (a) Photonic crystal (PC) waveguide cavity [65], (b) semiconductor ridge waveguide cavity [66], (c) Combination of CBG and waveguide cavity [67].

rectangular-holes-based SPS, depicted in Fig.1.7 (b), featuring an efficiency of 86% [76], and another value of 73% in a circular-holes-based device [77]. How to realize a near-unity efficiency in a semiconductor ridge waveguide platform becomes one of the main topics argued in this thesis. The tapered cavity, which can help to reduce the losses into radiation via an adiabatic transition from fundamental cavity mode to Bragg mirror mode [78,79], is the answer we propose in Chapter 4. Another interesting structure visualized in Fig.1.7 (c) is the combination of elliptical CBG and the on-chip waveguide [67], where the dimensional parameters of the bullseye are designed by different criteria used in the vertical emission CBG mentioned above to ensure the planar light propagation. Apart from the coupling with QDs, bare waveguide structures also allow the interaction with 2D single photon emitters [80,81]. The blank space in the experimental demonstration of efficient coupling between monolayer emitters and the on-chip cavity is an exciting field left to the researchers.

1.4 Spectral tuning and charge control

This sub-chapter will illustrate the key reasons for implementing the electric contacts to the QD-based SPSs. As introduced in Chapter 1.2, there is charge noise around the QD environment, which brings spectral wandering

and fluctuation to the photon emissions. They separately cause the shift and broadening to the QD ZPL and eventually hurt the photon indistinguishability. A practical solution is applying electric contacts, as demonstrated in Fig.1.8 (a), which can stabilize the charge state by Coulomb blockade [82–84] and drastically reduce the noise fluctuation [85]. Applying this strategy, Zhai *et al.* [86] experimentally demonstrated the ultra-low-noise behavior in GaAs QDs.

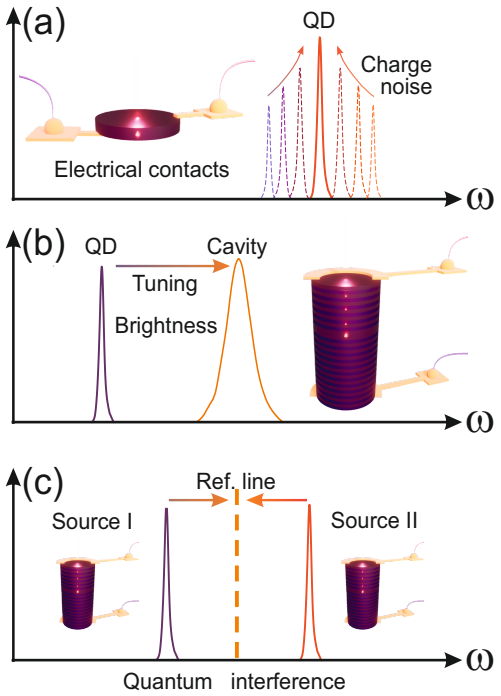

Figure 1.8. Illustration of the three main reasons for applying electrical contacts to QDs for high SPS performances: (a) stabilizing the charge environment to reduce the spectrum wandering and fluctuation. (b) tuning the QD emission line to the cavity resonance, especially in high-quality structures, for instance, Micropillar. (c) tuning remote QDs to the same emission frequency allowing for multi-photon interference from individual devices. The figure is taken from [87].

Due to the decoherence occurring at the PSB and to improve photon collection, it is necessary to embed the QD into a nano-cavity. However, the random nature of the nucleation process and the diffusion of material on the surface will make the QDs' sizes and compositions uncontrollable [88]. In principle, these properties affect the QD emission line [89]. On the other hand, the imperfections in the fabrication procedure also lead to the cavity resonance

shift from the design. Considering these uncontrollable factors, the tuning of QDs and the nano-cavities for better spectral alignment can benefit the high-quality SPSs. It's noticed that an open cavity structure allows the tuning of cavity [27]. However, the mode resonances in most other nano-cavities are not straightforward to change. Therefore, the tuning of QD emission frequency into the cavity resonance, indicated by Fig.1.8 (b), is more feasible. Several methods have been applied to modify the emission wavelength, such as temperature tuning [90–92], magnetic field application [2, 93], or strain implementation [94–96]. However, the most promising, integrated, and scalable is the electrical tuning by Stark effect [97–101]. The Quantum-confined Stark effect (QCSE) allows for finely tuning the optical transition frequency of the QD by affecting the Coulomb and exchange interactions among the charge carriers [102–104]. This strategy has been successfully applied in Micropillar [26, 105–107], open cavity [27], and PC waveguide cavities [65, 108, 109].

Electric tuning can also contribute to the interference between remote single photons. Scalable linear quantum computing highly demands large amounts of indistinguishable photons to interfere with each other [110]. Implementing the electrical control to the individual SPSs, as shown in Fig.1.8 (c), enables the spectral alignment between the remote QDs, which is a significant precondition of successful two-photon or even multi-photons interference. In 2010, Patel *et al.* [111] carried out the first work regarding the interference of photons from two individual sources. Recent work from Zhai*et al.* [39] demonstrated two-photon interference visibility of >93% obtained from two separate electrically-tunable QDs, proving the effectiveness of electric tuning strategy in the field of remote photon interference. Pascale Senellart's group and Peter Lodahl's group dedicate to realizing the same goal with the favor of electric tuning based on different Micropillar [112, 113] and PC waveguide cavities [114, 115], respectively. Almost all the applications of electric contacts need to implement additional sections around the cavity. Thus, Chapter 5 in this thesis will demonstrate our perspectives on the impacts of these appendages on the SPS performance, especially the source efficiency.

CHAPTER 2

General introduction of numerical methods

This chapter will give a general introduction to the modeling techniques used in this thesis. The project is investigated using the two-level semiconductor QD. Thus, how to describe it in numerical simulations is of vital importance before we start to model the SPS.

2.1 Dipole approximation

We first consider a classical point dipole $\boldsymbol{d}$ located at the position r_0 can generate a corresponding current j, given by

$$j(r) = -i\omega_0 \boldsymbol{d}\delta(r - r_0), \tag{2.1}$$

where ω_0 is the angular frequency of the current. To figure out the electric field $E(r)$ generated by $j(r)$, we need to solve the second-order wave equation, which comes from the classical Maxwell's equation with the absence of magnetic materials and free charges, following:

$$\nabla \times \nabla \times E(r) - \epsilon_r(r){k_0}^2 E(r) = i\omega_0\mu_0 j(r), \tag{2.2}$$

where k_0 is the free-space wavenumber, μ_0 is the vacuum permeability and $\epsilon_r(r)$ is the dielectric constant of the surrounding material. An elegant solution by applying the dyadic Green's function $\overline{\overline{G}}$ [116] is given by

$$E(r) = i\omega_0\mu_0 \int_V \overline{\overline{G}}(r, r')j(r')\, dr', \tag{2.3}$$

where the Green's function $\overline{\overline{G}}$ represents the field generated at the location r by a current at location r'. The total power emitted by the current can be evaluated by the integration of the normal component of the Poynting vector

over the surface S of the Volume V surrounding the current, which is described by

$$P = \frac{1}{2}\int_S Re(E \times H^*) \cdot n_s \, dS, \tag{2.4}$$

where n_s is the unit vector normal to the surface S. According to Poynting's theorem, the average energy dissipation rate W of the Volume V given by

$$W = -\frac{1}{2}\int_V Re(j^* \times E) \, dr \tag{2.5}$$

is equivalent to P, combing with Eq.2.1, Eq.2.3 and Eq.2.5, we can get the relation of power P and the dipole $\boldsymbol{d}$, complying with the equation

$$P = \frac{{\omega_0}^3 \mu_0 |\boldsymbol{d}|^2}{2} \mathrm{Im}\left(n_d \cdot \overline{\overline{G}}(r_0, r_0) \cdot n_d\right), \tag{2.6}$$

where $n_d = \boldsymbol{d}/|\boldsymbol{d}|$ is the dipole orientation.

So far, we have obtained the expression of power P in terms of the dipole moment $\boldsymbol{d}$ and Green's function $\overline{\overline{G}}$. Now we turn our attention to the description of Spontaneous emission (SE) in a two-level system, for instance, an InAs QD. Under the weak coupling framework and according to Fermi's golden rule [117], the SE rate Γ of the QD at the position r_0 complies with

$$\Gamma = \frac{\pi\omega_0}{\hbar\epsilon_0} |\boldsymbol{d}|^2 \rho\left(n_d, r_0, \omega_0\right), \tag{2.7}$$

where ω_0 is the angular transition frequency of the QD. In terms of Green's function, the LDOS can be written as [118]

$$\rho\left(n_d, r_0, \omega_0\right) = \frac{2\omega_0}{\pi c^2} \mathrm{Im}\left(n_d \cdot \overline{\overline{G}}(r_0, r_0, \omega_0) \cdot n_d\right). \tag{2.8}$$

Inserting Eq.2.8 into Eq.2.7 and comparing with Eq.2.6, we obtained a very important Dipole approximation (DA) relationship

$$\frac{\Gamma}{\Gamma_0} = \frac{P}{P_0}, \tag{2.9}$$

which tells the equivalence of the normalized QD SE rate Γ/Γ_0 and the normalized power dissipation P/P_0 from a point dipole, where Γ_0 or P_0 is the corresponding emission evaluated in bulk material. The DA is a fundamental assumption in the model of SPS investigated in this project. Although some works argued that the failure of DA could be caused by larger QD size [119] or a close distance to the material interface [120, 121], the QD and platforms

discussed in this thesis are still roughly safe under these considerations. Concerning the horizontal dimension of the InAs QD is much larger than the vertical dimension, as visualized in Fig.1.4 (b), only the in-plane dipole orientations are taken into account throughout the thesis.

2.2 Fourier modal method

Fourier modal method (FMM) is a powerful tool to calculate the optical properties in nano-photonic structures, especially the rationally symmetric models, where the 3D simulations can be simplified to 2D. In this thesis, FMM is used to calculate the dipole emission in nanopost SPS. Here, we only introduce the basic theory and algorithm for electric field computation of the device of our interest. For a more detailed introduction and discussion, please see Ref. [122].

The four-layer 2D geometry depicted in Fig. 2.1 (a) is fully comparable to the nanopost structure shown in Fig. 3.1. Each of these layers has a uniform permittivity profile along the z-axis. Layers 1,2, and 4 are homogeneous, while the lightness change in layer 3 indicates the diversification of the refractive index along the x-axis. Our target is to compute the optical field in Layer 3, corresponding to the cavity region in the nanopost device investigated in Chapter3.1. The application of FMM relies on the plane-wave expansion theory. Thus, as the first step after segmenting the object, the eigenmodes in each layer have to be calculated by solving the eigenvalue problem equation:

$$\nabla^2 \mathbf{e_m} + \nabla(\mathbf{e_m} \cdot \nabla \mathbf{ln}\epsilon(r)) + \epsilon(r){k_0}^2 \mathbf{e_m} = {\beta_m}^2 \mathbf{e_m}. \tag{2.10}$$

Here, $\mathbf{e_m}$ represents the lateral field component, and β_m is the propagation constant of the eigenmode m. Especially, eigenmodes must fulfill the continuity condition at the material-material interfaces in Fig.2.1 (a) layer 3, which has a mutative refractive index along the x-axis. Then according to mode expansion theory, we can use these modes and propagation constants to describe the electric field (lateral component) in the corresponding layer, given by

$$E(r) = \sum_{m=1}^{N} a_m \mathbf{e_m}(r) e^{i\beta_m z} + \sum_{m=1}^{N} b_m \mathbf{e_m}(r) e^{-i\beta_m z}, \tag{2.11}$$

where a_m and b_m are the expansion coefficients of the forward and backward propagating modes. Theoretically, the summations are carried out over an infinite number of modes, but we need to cut off this value at N for practical calculations. Due to the light transmissions and reflections between all the

layers, as indicated in Fig. 2.1 (b), we need to confirm the exact expansion coefficients by implementing the S-matrix technique [123], where the S-matrix is used to link the non-adjacent layers.

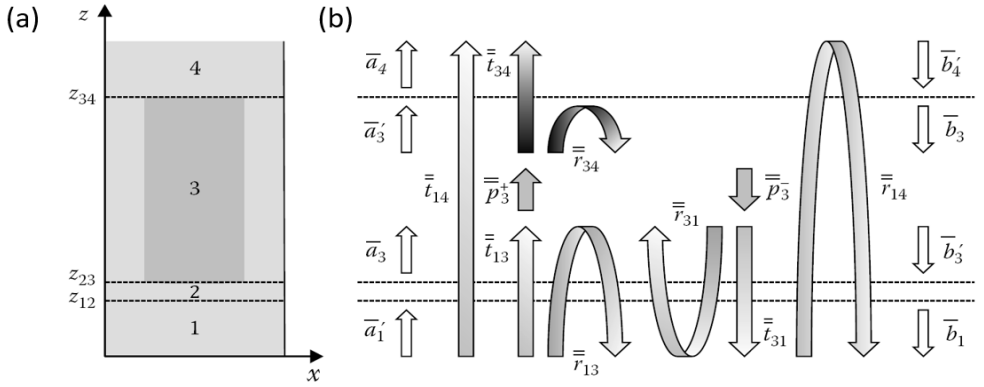

Figure 2.1. (a) Sketch of a four-layer 2D-geometry. (b) The reflection and transmission of light inside the structure. This figure is taken from Ref. [122] FIGURE 6.18.

Taking the 4-layer geometry as an example, the first thing we need to do is calculate the reflection $\overline{\overline{r}}$ and transmission $\overline{\overline{t}}$ matrices at each interface $\overline{\overline{r_{12}}}$,$\overline{\overline{r_{21}}}$, $\overline{\overline{t_{12}}}$,$\overline{\overline{t_{21}}}$, $\overline{\overline{r_{23}}}$,$\overline{\overline{r_{32}}}$, $\overline{\overline{t_{23}}}$,$\overline{\overline{t_{32}}}$, $\overline{\overline{r_{34}}}$,$\overline{\overline{r_{43}}}$, $\overline{\overline{t_{34}}}$,$\overline{\overline{t_{43}}}$, which all can fulfill the boundary conditions requiring the continuity of the tangential electric and magnetic fields at the corresponding layer-layer interfaces. Then the other recursive matrices followed the S-matrix formalism between the non-adjacent layers have the relations shown below:

$$\overline{\overline{r_{1,q+1}}} = \overline{\overline{r_{1,q}}} + \overline{\overline{t_{q,1}}}\overline{\overline{p_q}}^{-}\overline{\overline{r_{q,q+1}}}\overline{\overline{p_q}}^{+}\left(\overline{\overline{I}} - \overline{\overline{r_{q,1}}}\overline{\overline{p_q}}^{-}\overline{\overline{r_{q,q+1}}}\overline{\overline{p_q}}^{+}\right)^{-1}\overline{\overline{t_{1,q}}} \tag{2.12}$$

$$\overline{\overline{t_{1,q+1}}} = \overline{\overline{t_{q,q+1}}}\overline{\overline{p_q}}^{+}\left(\overline{\overline{I}} - \overline{\overline{r_{q,1}}}\overline{\overline{p_q}}^{-}\overline{\overline{r_{q,q+1}}}\overline{\overline{p_q}}^{+}\right)^{-1}\overline{\overline{t_{1,q}}} \tag{2.13}$$

$$\overline{\overline{r_{q+1,1}}} = \overline{\overline{r_{q+1,q}}} + \overline{\overline{t_{q,q+1}}}\overline{\overline{p_q}}^{+}\left(\overline{\overline{I}} - \overline{\overline{r_{q,1}}}\overline{\overline{p_q}}^{-}\overline{\overline{r_{q,q+1}}}\overline{\overline{p_q}}^{+}\right)^{-1}\overline{\overline{r_{q,1}}}\overline{\overline{p_q}}^{-}\overline{\overline{t_{q+1,q}}} \tag{2.14}$$

$$\overline{\overline{t_{q+1,1}}} = \overline{\overline{t_{q,1}}}\overline{\overline{p_q}}^{-}\overline{\overline{t_{q+1,q}}} + \overline{\overline{t_{q,1}}}\overline{\overline{p_q}}^{-}\overline{\overline{r_{q,q+1}}}\overline{\overline{p_q}}^{+}\left(\overline{\overline{I}} - \overline{\overline{r_{q,1}}}\overline{\overline{p_q}}^{-}\overline{\overline{r_{q,q+1}}}\overline{\overline{p_q}}^{+}\right)^{-1}\overline{\overline{r_{q,1}}}\overline{\overline{p_q}}^{-}\overline{\overline{t_{q+1,q}}} \tag{2.15}$$

$$\overline{\overline{r_{q-1,n}}} = \overline{\overline{r_{q-1,q}}} + \overline{\overline{t_{q,q-1}}}\,\overline{\overline{p_q}}^{-}\,\overline{\overline{r_{q,n}}}\,\overline{\overline{p_q}}^{+}\left(\overline{\overline{I}} - \overline{\overline{r_{q,q-1}}}\,\overline{\overline{p_q}}^{-}\,\overline{\overline{r_{q,n}}}\,\overline{\overline{p_q}}^{+}\right)^{-1}\overline{\overline{t_{q-1,q}}} \tag{2.16}$$

$$\overline{\overline{t_{q-1,n}}} = \overline{\overline{t_{q,n}}}\,\overline{\overline{p_q}}^{+}\left(\overline{\overline{I}} - \overline{\overline{r_{q,q-1}}}\,\overline{\overline{p_q}}^{-}\,\overline{\overline{r_{q,n}}}\,\overline{\overline{p_q}}^{+}\right)^{-1}\overline{\overline{t_{q-1,q}}} \tag{2.17}$$

$$\overline{\overline{r_{n,q-1}}} = \overline{\overline{r_{n,q}}} + \overline{\overline{t_{q,n}}}\,\overline{\overline{p_q}}^{+}\left(\overline{\overline{I}} - \overline{\overline{r_{q,q-1}}}\,\overline{\overline{p_q}}^{-}\,\overline{\overline{r_{q,n}}}\,\overline{\overline{p_q}}^{+}\right)^{-1}\overline{\overline{r_{q,q-1}}}\,\overline{\overline{p_q}}^{-}\,\overline{\overline{t_{n,q}}} \tag{2.18}$$

$$\overline{\overline{t_{n,q-1}}} = \overline{\overline{t_{q,q-1}}}\,\overline{\overline{p_q}}^{-}\,\overline{\overline{t_{n,q}}} + \overline{\overline{t_{q,q-1}}}\,\overline{\overline{p_q}}^{-}\,\overline{\overline{r_{q,n}}}\,\overline{\overline{p_q}}^{+}\left(\overline{\overline{I}} - \overline{\overline{r_{q,q-1}}}\,\overline{\overline{p_q}}^{-}\,\overline{\overline{r_{q,n}}}\,\overline{\overline{p_q}}^{+}\right)^{-1}\overline{\overline{r_{q,q-1}}}\,\overline{\overline{p_q}}^{-}\,\overline{\overline{t_{n,q}}} \tag{2.19}$$

For the 4-layer structure, q can be 2 or 3, and n is 4. In these equations, $\overline{\overline{I}}$ is the unit matrix, $\overline{\overline{p_q}}^{-/+}$ represents the backward or forward propagation matrix in layer q, respectively. Specify q as 3, corresponding to the cavity layer in the nanopost structure, where we put a dipole at the interface z, and define $z - z_{23} = z_b$, $z_{34} - z = z_t$. We can write the expressions of the expansion coefficients in Eq. 2.11 at the height z as:

$$\overline{a_m{}^z} = \left(\overline{\overline{I}} - \overline{\overline{p_3(z_b)}}\,\overline{\overline{r_{3,1}}}\,\overline{\overline{p_3}}\,\overline{\overline{r_{3,4}}}\,\overline{\overline{p_3(z_t)}}\right)^{-1}\left(\overline{a_m} + \overline{\overline{p_3(z_b)}}\,\overline{\overline{r_{3,1}}}\,\overline{\overline{p_3(z_b)}}\,\overline{b_m}\right) \tag{2.20}$$

$$\overline{b_m{}^z} = \left(\overline{\overline{I}} - \overline{\overline{p_3(z_t)}}\,\overline{\overline{r_{3,4}}}\,\overline{\overline{p_3}}\,\overline{\overline{r_{3,1}}}\,\overline{\overline{p_3(z_b)}}\right)^{-1}\left(\overline{b_m} + \overline{\overline{p_3(z_t)}}\,\overline{\overline{r_{3,4}}}\,\overline{\overline{p_3(z_t)}}\,\overline{a_m}\right). \tag{2.21}$$

Here, $\overline{\overline{p_3}} = diag(e^{i\beta_m(z_{34}-z_{23})})$ is the propagation matrix throughout layer 3, $\overline{a_m}$ and $\overline{b_m}$ are the initial forward and backward coefficients of the eigenmodes in the same layer. Finally, we obtain the expression of the lateral electric field component at the dipole position in the nanopost cavity (layer 3), complying with [122]:

$$E(r,z) = \sum_{m=1}^{N} a_m{}^z \mathbf{e_m}(r) + \sum_{m=1}^{N} b_m{}^z \mathbf{e_m}(r), \tag{2.22}$$

where $\mathbf{e_m}$ only refers to the eigenmodes found in the cavity layer.

To obtain far-field photon collection efficiency, we need to apply the near-to-far field transformation technique. In simple terms, the equivalent currents

related to the near-field electric and magnetic distributions are assumed to appear right above the top facet z_{34}. Combined with the coordinate transformation (cylindrical to spherical), we calculate the far-field distribution generated by the equivalent currents and integrate the time-averaged Poynting vector at the far-field spherical surface, typically within the Numerical aperture (NA) of an objective lens. The detailed description of near-far-field transformation can be found in Ref. [124, 125].

2.3 Finite element method

The numerical studies for most of this thesis were carried out by Finite element method (FEM) with the commercial simulation package JCMsuite, which is well-suitable for calculating optical nanostructures. [126–128]. As a tool but not the main subject in the research, this subchapter will provide a short and general introduction to the FEM solving process.

In 1969, P. P. Silvester used the FEM to analyze wave propagation in waveguides, the first time that the FEM was applied to microwave engineering and electromagnetism. The FEM is based on the frequency-domain Maxwell's equation, whose solution object is the time-harmonic electromagnetic field, meaning that the field is periodically distributed in the time dimension, and thus only a distribution function of spatial variables:

$$\begin{aligned} \nabla \times E &= -j\omega\mu H \\ \nabla \times H &= j\omega\epsilon E + J \\ \nabla \cdot (\epsilon E) &= -\frac{1}{j\omega}\nabla \cdot J \\ \nabla \cdot (\mu H) &= 0 \end{aligned} \tag{2.23}$$

The solving process starts with spatial discretization by dividing the entire structure into a large number of small elements, typically triangles or tetrahedrons. The second step is to discretize the spatial electromagnetic field distribution to be solved, where the fundamental idea is to find a set of basis functions, which are the tangential components on the jth edge E_j, and the corresponding coefficients N_j to assemble the unknown solution E:

$$E = \sum_{j=1}^{\Omega} N_j E_j. \tag{2.24}$$

The FEM solver uses simple linear or quadratic functions to approximate the unknown field distributions on every single element, called subdomain basis functions. The last step is to find out the coefficients that can fulfill the wave functions in domain Ω and the boundary conditions. Until now, we get all the basis functions and their coefficients, and according to them, the FEM solver can reassemble the electric field in the whole computational domain. For more detailed illustrations about FEM, please see the books from J.M. Jin [129] and A.C. Polycarpou [130].

2.4 Quasi-normal mode approach

Quasi-normal modes (QNM) approach is an essential tool helping us to analyze the discrete modes' contributions to the LDOS at the position of our interest in the nano-cavity. Different from the DA applied in FMM and FEM, QNMs are the solutions to the source-free Maxwell's equations. In the weak coupling regime, LDOS ρ is proportional to the QD SE rate [118], and thus can be expressed as:

$$\rho(r_0,\omega) = \frac{2\omega}{\pi c^2}\mathrm{Im}\left(n_d \cdot G(r_0,r_0,\omega)\cdot n_d\right), \tag{2.25}$$

Eq. 2.25 is the same as Eq. 2.8, while the overlines on top of $\overline{\overline{G}}$ are omitted for simplicity. Directly computing the Green's function G in complicated nano-cavity is challenging. Thus, we assume G can be approximately expanded by a few QNMs when the focus of simulation is around the cavity's frequency and position [131]. This hypothesis perfectly works under our frameworks since we are interested in the QD-cavity resonant coupling. In this scenario, Green's function is expanded by a finite number of QNMs as:

$$G(r_0,r_0,\omega) = \frac{c^2}{2}\sum_m \frac{E_m(r_0)\bigotimes E_m(r_0)}{\omega_m(\omega_m-\omega)}, \tag{2.26}$$

where ω_m is the complex angular frequency of the mth QNM, $E_m(r_0)$ is the corresponding normalized field strength at the position r_0. Inserting Eq. 2.26 into Eq. 2.25, the LDOS in terms of QNMs is given by:

$$\rho(r_0,\omega) = \frac{\omega}{\pi}\sum_m \mathrm{Im}\left(n_d \cdot \frac{E_m(r_0)\bigotimes E_m(r_0)}{\omega_m(\omega_m-\omega)}\cdot n_d\right), \tag{2.27}$$

combining with the LDOS in bulk material $\rho_0(\omega) = \omega/(2\pi c^2)$, we can finally evaluate the normalized frequency-dependent LDOS by $\rho(r_0,\omega)/\rho_0(\omega)$, which

is comparable to the normalized SE rate of the QD supposed to locate at position r_0. In our simulations, the QNMs are solved in FEM software JCMsuite by searching the eigenmodes around the cavity resonance.

Part II

Designs, results, and discussions

CHAPTER 3

Designs of vertical-emission single-photon sources

As summarized in the Introduction for nano-cavities (Chapter 1.3), we reviewed multiple types of structures [26, 27, 57, 62, 65, 71, 77, 132–135] that can be applied to improve SPSs' performances. These cavities can be classified into different categories from various perspectives. For instance, broadband structures are easier to fall into resonance with the quantum emitters [135, 136], while high-quality cavities are beneficial to photons' indistinguishability [26, 27].

Another consideration can revolve around source tunability. The spectral and spatial misalignments of QD and cavities are practical challenges in experiments. Thus, the tunability of QD and cavities is a critical topic in realizing a high-performance SPS. As introduced in Chapter 1.4, spectral tuning on QD emission has already been realized by implementing electrical contacts [25–27]. On the other hand, the spatial location of QD can also be deterministically controlled by QD imaging technique [137]. However, it is more difficult to play with the cavity resonance. Thus, whether the cavity itself is adjustable is also one of the differentiating aspects. Strain-tunable models [66, 95] can be used to achieve this goal. While in contrast, the open cavity [27] itself is also able to be adjusted by moving the top mirror in spatial, so that it is more convenient to tune the cavity resonance and find the QD locations.

In this thesis, we classify the nano-cavities into two groups under the consideration of photon collecting directions, vertical or on-chip. Chapter 3 is mainly focused on the former, including nanopost, new-type bullseye, and open cavity designs. They separately target the three properties we demonstrated above: broad bandwidth, high-quality factor, and device tunability.

The idea of Chapter 3.1.1 is published in ref [138], in this paper, the PhD student gave the contribution to all the numerical simulation results. Chapter 3.1.2 is based on the publication ref [133], where the FEM and QNM analysis of the asymmetric spectrum were carried out by the PhD candidate.

3.1 Nanopost device

This section will illustrate the FMM-based modeling and design procedure of a simple but effective nanopost SPS, which features a remarkable Purcell enhancement, decent source efficiency, and good potential for ease of fabrication. Apart from FMM, we also applied QNM introduced in Chapter 2.4 to check the consistency between these two approaches and got a good agreement from them.

3.1.1 Modeling and design procedure based on FMM

The structure under consideration is depicted in Fig.3.1. It consists of a gold-SiO_2 bottom mirror and a truncated GaAs nanowire, where QD is located on its central axis. To make a good cavity, we need to find the optimal design with proper dimensional parameters, which include the diameter of the nanowire, the thickness of the glass slab h_{SiO_2}, and the vertical location of the QD relative to the top GaAs-Air facet h_t and to the bottom GaAs-SiO_2 facet h_b. But before presenting the design procedure, we would like to first introduce the three figures of merits considered in this work.

According to the FMM introduced in Chapter 2.2, the photons emitted by the QD will funnel into separate modes. Among them, the fundamental HE_{11} mode guided by the nanowire is one that we expect photons can be coupled to the maximum proportion. In nanopost structure, the cavity mode can be roughly considered as the reflections of HE_{11} mode. Under this framework, we assume the total emission from the QD is evaluated by $\Gamma_t = \Gamma_{c/HE_{11}} + \Gamma_\gamma$, where $\Gamma_{c/HE_{11}}$ is the SE rate of cavity mode in nanopost or that of HE_{11} mode in untruncated nanowire, and Γ_γ is the total power from all the other background modes. The first figure of merit β factor is used to quantitatively describe the proportion of light funneling into the cavity or HE_{11} mode, with the definition of:

$$\beta = \frac{\Gamma_{c/HE_{11}}}{\Gamma_t}. \tag{3.1}$$

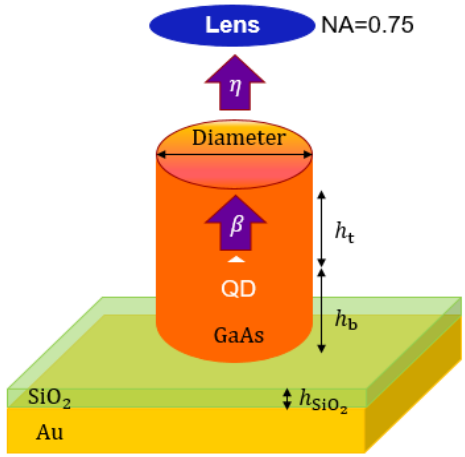

Figure 3.1. Sketch of the nanopost structure. QD presented by the white triangle is embedded in the GaAs mesa, beneath which is the bottom mirror consisting of a thin slab of SiO_2 and the gold substrate. The coupling factors β and η are schematically shown.

To evaluate how much of the light can be collected by the objective, we now introduce another factor, which is the transmission efficiency

$$\eta = \frac{\Gamma_{NA}}{\Gamma_{c/HE_{11}}}, \tag{3.2}$$

where Γ_{NA} is the power collected by the first lens within a NA of 0.75. The product of these two factors then comes up with the second critical figure of merit in this work: the total source efficiency $\epsilon = \beta\eta$. We are also curious about, to what extent QD emission can benefit from the nanopost cavity, especially the part of power funneling into the cavity mode. So this brings the last quantity of interest, the normalized SE rate Γ_c/Γ_0, where Γ_0 is the emission rate in a bulk material.

Now we can step into the detailed design procedure for the nanopost device working at 928nm. The first parameter that has to be determined is the diameter of the GaAs nanowire. So in this step, we swipe the diameter of the infinitely long nanowire to get an insight into how the β factor responds. As shown in Fig.3.2 (a), within a diameter range between 200nm to 250nm, there is a very good HE_{11} mode coupling efficiency of over 90%. However, this is a quite large range with respect to the optimum design.

Therefore, in the second step, we look into the reflectivity of HE_{11} mode to help us find the proper diameter which leads to the highest reflectivity at

the facets. The calculation at the bottom GaAs-SiO_2 interface needs to know the exact thickness of the glass, and therefore we choose the top GaAs-Air reflectivity as the object of interest. Fig.3.2 (a) clearly tells us 245nm is the optimum diameter with approximately 43% of light being reflected back to the cavity.

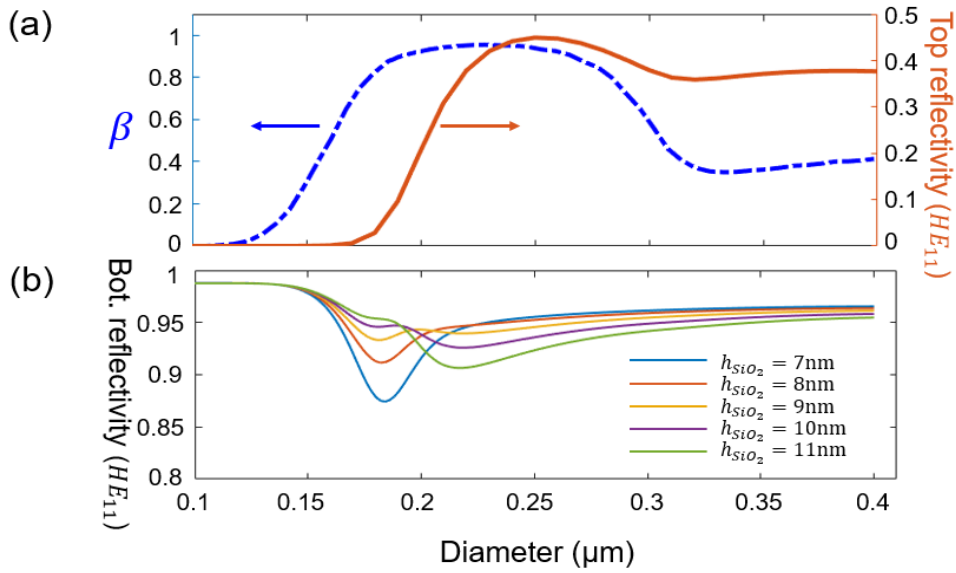

Figure 3.2. (a) coupling β factor and the reflectivity from the top facet of HE_{11} mode as a function of nanowire diameter. (b)HE_{11} mode reflectivity from the bottom GaAs-SiO_2 facet as a function of nanowire diameter when the thickness of SiO_2 slab varies from 7 to 11 nm. The refractive index of gold is chosen as n_{Au}=0.12+6.24i.

Now it is time to look for an appropriate h_{SiO_2}. Our target is to build a good nano-cavity, which apparently requires the bottom reflectivity as large as possible. As implied by Fig.3.2 (b), at our designed diameter 245nm, h_{SiO_2}=7nm becomes the optimum thickness, which shows a 95% reflection of the fundamental mode. Until now, we are almost close to the final target. The last step in our design procedure is to locate the QD at the anti-nodes with respect to the top and bottom interfaces, which means the position of the QD can only be discretely changed. This is to ensure that constructive interference can happen in the nanopost cavity. Under the framework of Single modal method (SMM), the source performances would not be affected by the order of the anti-nodes. Thus, we simply put the QD at the first longitudinal anti-node of the nano-cavity mode, which means h_b=70nm, and h_t=390nm.

In our extensive work [133], we further discuss the breakdown of SMM and implement the full model to more accurately describe the performances of the nanopost SPS. While in this chapter, we still adopt the SMM scenario to compute SE rate and the source efficiency.

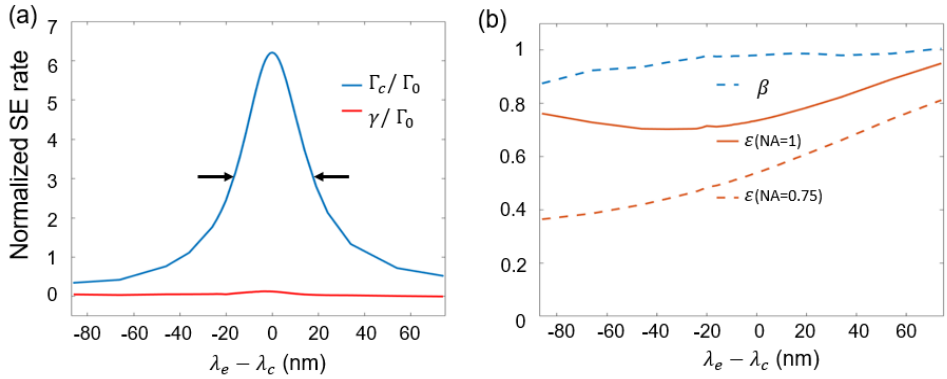

Figure 3.3. (a) Normalized SE rate of the cavity mode (blue) and all the other background modes (red), (b) cavity mode coupling factor β, first lens source efficiency within NA=1 (solid) and NA=0.75 (dashed) as a function of the wavelength detuning. λ_e and λ_c are the emission of the QD, and the resonance of the nanopost cavity, respectively.

Our designed nanopost cavity works at the wavelength of 928nm, Fig.3.3 (a) indicates a remarkable on-resonance Purcell enhancement of 6.3, while the background emission rate is fairly low. The high fraction of the light funneled into the cavity mode is also demonstrated by the high β factor shown in Fig.3.3 (b). Full width at half maximum (FWHM) of approximately 40nm extracted between the arrows in Fig.3.3 (a) proves our nanopost cavity is a broadband structure. In addition, within a broad QD-cavity detuning range (-86nm∼76nm), we predict this nanopost device can stably support the emissions coupling into the cavity mode, which is proven by the nearly flat β curve in Fig.3.3 (b). Regarding source efficiency, we obtain a value of 54% at the cavity resonance within NA of 0.75.

However, the increase of ϵ from 38% at detuning=-86nm to 82% at detuning=76nm can hardly be ignored. To figure out the reason, we also plot the corresponding efficiency under NA=1 in Fig.3.3 (b). The solid orange curve indicates that the total collection in the upper far field does not change too much when tuning the QD wavelength, at least more gently than the ϵ (NA=0.75). Thus, we plot the far-field emission patterns in Fig.3.4 to get insight into what happens in the far-field region when the QD wavelength

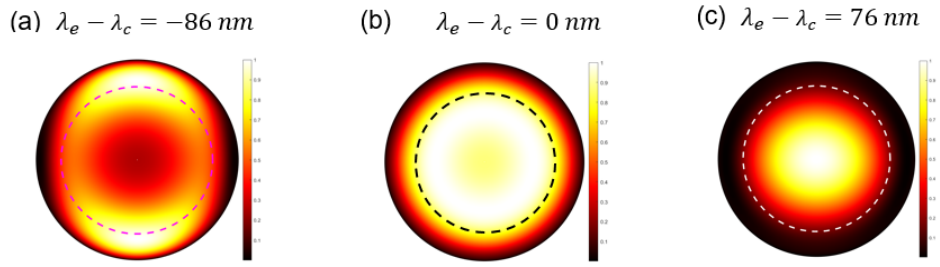

Figure 3.4. Far-field emission patterns observed at the QD-cavity detuning of (a) -86nm, (b) 0nm, and (c) 76nm respectively. The dashed circles represent the range of NA=0.75.

redshifts. The evolution of the field profiles from Fig.3.4 (a) to (c) implies the gathering of the light to the spot center, which improves the fraction of the power collected by the objective divided by the total energy transferred to the upper far field. Then this can explain the gradual approach of curve ϵ (NA=0.75) to curve ϵ (NA=1) in Fig.3.3 (b) when the QD-cavity detuning varies from negative to the positive regime.

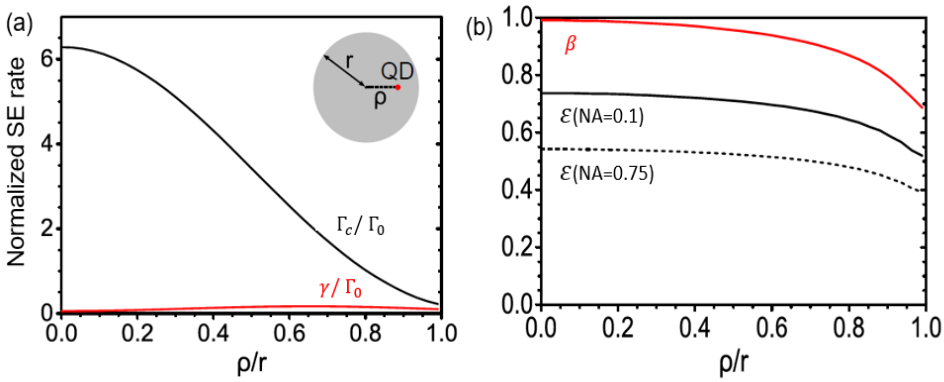

Figure 3.5. (a) Normalized emission rates into the cavity mode (Γ_c/Γ_0) and into the other modes (Γ_γ/Γ_0) as a function of the normalized distance to the axis (ρ/r). (b) β factor and total efficiency ϵ NA = 1 and 0.75) as a function of ρ/r. The QD is resonant with the nano-cavity mode ($\lambda_e = \lambda_c$) and is modeled as an in-plane isotropic optical dipole. Figure taken from [138].

As demonstrated at the beginning of Chapter 3.1.1, we locate the QD exactly on the central axis of GaAs section. However, in reality, it is very difficult to perfectly control the QD position. This means that we have to consider the impact of the QD in-plane spatial misalignment on the factors

of interest in this work. An off-axis location breaks the symmetry between radial and tangential QD dipoles. For simplicity, we model here the QD as an in-plane, isotropic optical dipole, which means the emission rate into a given mode is the average of the rates of the radial and tangential dipoles. The calculations are conducted for a QD at spectral resonance. Fig.3.5 (a) shows the normalized emission rate into the cavity mode and into the other modes as a function of the normalized distance to the axis ρ/r (r is the nano-cavity radius). The maximum SE rate of the cavity mode is achieved on the axis (r = 0). For ρ/r equals 0.5, normalized rate Γ_c/Γ_0 is divided by a factor of 2. Fig.3.5 (b) shows the factor β and ϵ as a function of the misalignment. Again, the maximum β and ϵ are achieved on the axis. However, both two factors are only weakly affected by the misalignment, which indicates our device has a decent tolerance to the QD in-plane spatial misalignment.

3.1.2 Comparison between FMM and QNM approaches

The work discussed in Chapter 3.1.1 was investigated under the framework of SMM. To more accurately describe the leaking of fundamental mode into the background modes, the breakdown of SMM is deeply investigated in Ref. [133]. The interaction between the fundamental mode and radiation modes makes the Purcell enhancement and source efficiency become sensitive to the order of anti-node. This means that locating the QD at 1st or 2nd anti-node would not affect the source performance with the SMM scenario. However, this is not the case under full model consideration.

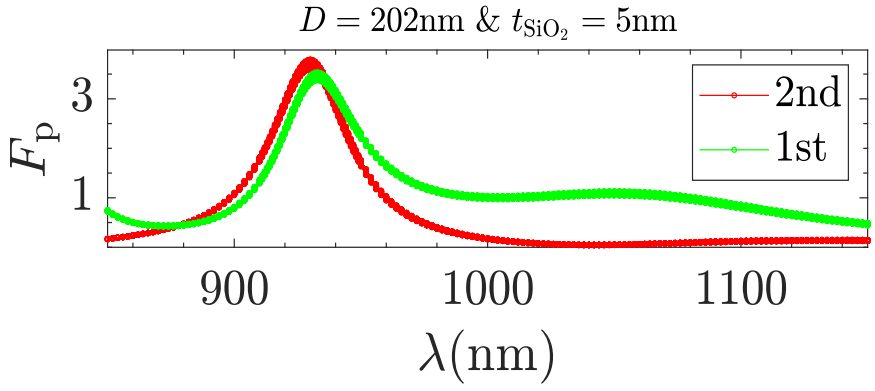

Figure 3.6. Purcell factor, F_p, as a function of wavelength, λ, for the two anti-nodes. The parameters are nanopost diameter D=202nm and silica slab thickness t_{SiO_2}=5nm. Figure taken from [133].

Here we define the Purcell factor F_p=Γ_t/Γ_0, as the normalized SE rate from all the modes (fundamental and radiations). The spectrum deviation when QD at different positions (1st or 2nd anti-node) can clearly be observed from Fig.3.6, where the nanopost has a diameter of 202nm and the silica slab is 5nm thick. Although this is not the optimum design, it behaves a pronounced difference between the two spectra. Not only the shift of cavity resonance but also we can see the asymmetric wavelength dependence for the two anti-nodes. To figure out why the tails appear on the spectra, we performed QNM (introduced in Chapter 2.4) simulations on the nanopost.

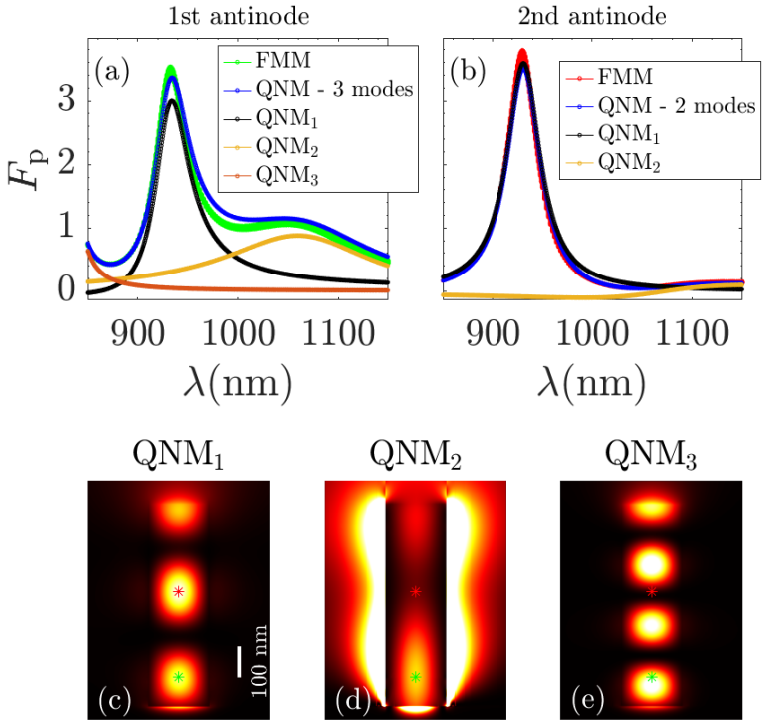

Figure 3.7. Comparison of the Purcell factor between the FMM and the QNM simulation for (a) the 1st anti-node and (b) the 2nd anti-node. Mode profiles of the three QNMs are shown in (c), (d), and (e). The green/red star corresponds to the position of the 1st/2nd anti-node, respectively. The white scale bar in (a) corresponds to 100nm. The intensity is scaled in each field plot and should not be used for comparison. Figure taken from [133].

In the end, 15 QNMs are found, with the complex eigenfrequencies in the form of $\tilde{\omega}_\mu = \omega_\mu - \mathrm{i}\gamma_\mu$. Among them, the three important QNMs are $\tilde{\omega}_{QNM_1} =$

$2.0237 \times 10^{15} - \mathrm{i}4.4904 \times 10^{13}$ Hz, $\tilde{\omega}_{QNM_2} = 1.7595 \times 10^{15} - \mathrm{i}1.4654 \times 10^{14}$ Hz and $\tilde{\omega}_{QNM_3} = 2.2809 \times 10^{15} - \mathrm{i}2.0703 \times 10^{13}$ Hz. The corresponding real parts of the complex wavelength are λ_{QNM_1}=930.3nm, λ_{QNM_2}=1063.2nm and λ_{QNM_3}=825.8nm. The Q factors of the QNMs can also be calculated using $Q_\mu = \omega_\mu/(2\gamma_\mu)$ [139], and we obtain Q_{QNM_1}=22.5, Q_{QNM_2}=6.0 and Q_{QNM_3}=55.1.

Fig.3.7 (a) and (b) demonstrate the comparison of the spectrum between FMM and QNM approaches when the QD is placed at the 1st and 2nd anti-node, respectively. The Purell factor simulated by FMM shows three possible peaks in Fig.3.7 (a), one below 900nm, one at 930nm and another smooth one around 1060nm. In the same figure, the independent spectra from three individual QNMs and the sum of them are depicted. We can see QNM_1 contributes most to the higher peak around 930nm, QNM_2 corresponds to the smooth slope at 1063nm, and QNM_3 most likely overlaps with the sharp peak on the left side of the wavelength range, because of the higher Q_{QNM_3} compared to the other two. Considering the total contributions from these three resonance modes, we find a good overlap between the green curve (FMM) and the blue curve (QNM-3 modes). To explain why these three modes can stand out from all the resonance modes. We plot the corresponding mode profiles in Fig.3.7 (c) to (e), where the green star refers to the position of the 1st anti-node. This position is also very close to an anti-node for QNM_2 and QNM_3. Therefore the contributions of these QNMs appear in the spectrum. Basically, the same story happens to the 2nd anti-node. As shown in Fig.3.7 (b), the spectrum of QNM_1 is almost sufficient to be compared with the FMM curve, apart from the small jump at a longer wavelength (>1050nm). But this can be compensated by QNM_2. Again, looking into mode profiles Fig.3.7 (c) to (e), we can find the 2nd anti-node (red star) is much closer to a node for QNM_3, and therefore it does not influence the spectrum.

Overall, we find FMM and QNM approaches have a good agreement with respect to the analysis of the cavity resonance. We also find out that the tails on the FMM spectra come from the contributions from other cavity modes at the QD position.

3.2 New-type bullseye structure

The bullseye structure, or the so-called CBG device [135,140] features a broadband property, a decent far-field collection efficiency, and a lower requirement in fabrication, and thus becomes a popular platform in the field of Quantum

light source (QLS). The low-quality cavity is welcomed with respect to the QD-cavity spectral alignment. However, it will cause the arising of phonon sideband in the QD emission spectrum, which is harmful to photon indistinguishability. Taking this as a starting point, the target of this chapter is to build a new type of bullseye structure with the combination of good source efficiency and high-quality factor. There is a natural obstacle to this goal, which is the trade-off between the strong in-plane field confinement and the large vertical light transmission, where the former points to the high Q cavity and the latter indicates a good photon collection.

3.2.1 Hole-bullseye design and optimization

Ref [134] proposed a high-Q hole-bullseye design with a numerical Q factor of 4200, resonant at 1050nm. As depicted in Fig.3.8 (b), the air trenches in regular bullseye structures Fig.3.8 (a) are replaced by air holes. Although the

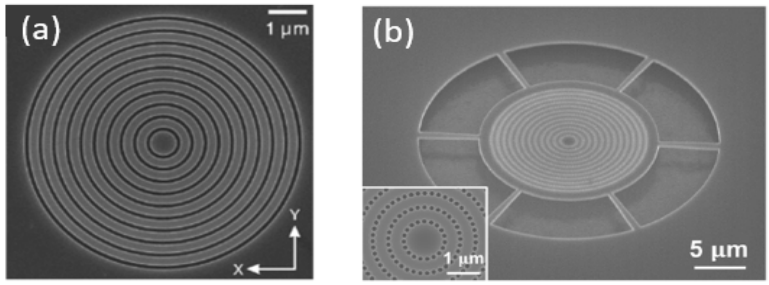

Figure 3.8. SEM image of (a) traditional ring CBG [140], and (b) hole-bullseye device [134].

diameter of the holes can be reckoned as the trench width in traditional designs, the additional parameter, angular periodicity between the neighboring holes, breaks the rotational symmetry and thus brings another degree of freedom in the axial direction, and in the end contributes to the groundbreaking quality factor. They claimed a good collection efficiency in the far field. However, this quantity is defined as the fraction of the light collected within a NA compared to the total upper half-sphere emission P_{NA}/P_{upper}, which is a bit different from our definition, $\epsilon = P_{NA}/P_{total}$, where P_{total} is the total emission from the QD. In addition, based on the wafers in our hands, we want to make a new design, which is made of different materials and works at another wavelength, compared to the cavity in Ref [134]. But we also hope it can keep the high Q factor, and maintain the good source efficiency ϵ comparable to the performance in traditional CBGs.

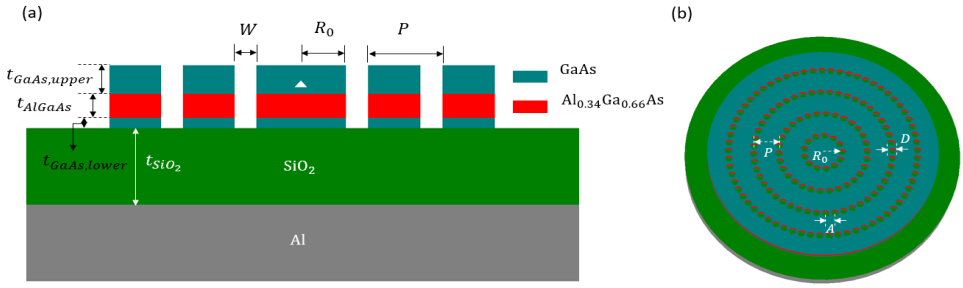

Figure 3.9. Schematics of (a) ring-CBG and (b) hole-CBG, based on our materials platform. The white triangle represents the QD.

We adopt the FEM (introduced in Chapter 2.3) to design and optimize bullseye structures in this section. Fig.3.9 (a) depicts the sketch of regular CBG design based on our wafer and material platform. The bullseye is constructed as a central disk with a radius of R_0=208.7nm, and 4 outer rings, with a pitch of P=341nm and a trench width W=102nm. In between the aluminum mirror and the CBG, there is a silica layer, whose thickness t_{SiO_2}=250nm is designed for an optimum source efficiency ϵ. The CBG itself consists of three sections, an $Al_{0.34}Ga_{0.66}As$ layer (t_{AlGaAs}=80.5nm) sandwiched by two GaAs layers with the thicknesses of $t_{GaAs,lower}$=32nm and $t_{GaAs,upper}$=92nm, respectively. The QD is located on the axis of the central disk and 7nm above the AlGaAs layer. At designed cavity resonance 910nm, this regular CBG performs a calculated Purcell factor of 11 and a source efficiency of 83%.

In the following, we illustrate the optimization procedure of a hole-CBG device, which is designed based on the same material platform as the ring-CBG introduced above. Since the rotational symmetry is broken by the air holes, directly optimizing the hole-bullseye is a highly demanding task from the aspect of computation. Thus, we inherit the parameters of the central disk radius R_0=208.7nm and the radial pitch P=341nm from the regular CBG design. The reason is that these two quantities mainly affect the cavity working wavelength, and we hope our regular CBG and hole-bullseye design can both work at 910nm. Then the optimizing parameters, shown in Fig.3.9 (b), are reduced from 4 to 2, only the hole diameter D and the angular period A remain. To save time and computational resources, the optimization in the next section starts from 4-ring structure.

3.2.1.1 Optimization strategy i

The optimization strategy I is inspired by Ref [134], where all the air holes have the same size and the same axial period. Thus, in step 1, we swipe the parameters D and A in a 4-ring hole-CBG structure and search the resonance cavity mode around the designed wavelength of 910nm. In test simulations, we notice that the distribution of the holes has the chance to split the cavity mode into two orthogonal non-resonant modes, leading to a poor quality factor. To get rid of the mode splitting and also to reduce the computational demand, we implement mirror boundary conditions in JCMSuite [141] to do the FEM simulations and only investigate a quarter of the geometry.

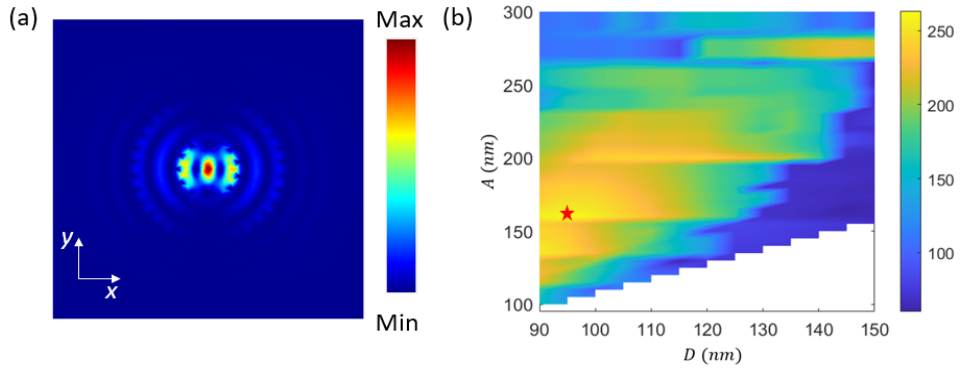

Figure 3.10. (a) In-plane mode profile of the hole-CBG cavity mode. (b) Q factor as the functions of parameters D and A, the red star indicates the optimum 4-ring structure with Q=263 optimized by the strategy I.

The cavity mode that we are looking for features a mode profile shown in Fig. 3.10 (a), where the strongest field intensity should appear at the QD position (in-plane center of the central disk). Fig. 3.10 (b) demonstrates how the Q factor responds to the change in hole diameter and angular periodicity. The discontinuous variation of Q along the y-axis is caused by the non-continuous change in the holes' locations. To ensure all the holes are complete and unified, the axial period should be divisible by an integer, which means the valid value of A is discrete. The maximum Q factor extracted from this plot is 263, corresponding to geometry with $A = 160$nm and $D = 95$nm. The second step in strategy I is keeping the parameters determined in step 1, and increasing the number of rings. Then we find a Q factor of 474 and an efficiency ϵ=86% become saturated from 8-ring geometry. Although it's already a breakthrough compared with the quality factor of one or two hundred in the regular CBG

SPSs, we are still far from the demanding high-quality cavity.

3.2.1.2 Optimization strategy ii

To give a more careful optimization, we change the strategy to optimizing the structure ring by ring, from the 1st to the N_{th}. After swiping the hole diameter and axial period in 1-Ring geometry, we extract the highest Q factor and assign the corresponding D_1 and A_1 to the first circle of holes. Based on it, the same scanning for the second ring is carried out. In the following, we simply determine the optimized parameters (D_N and A_N) for each ring by repeating the above steps, until the saturation happens. The results are listed in Table 3.1. Unfortunately, this strategy stops working at the 4-Ring structure, with a Q of 391. The optimization plots for each ring look similar to Fig. 3.10 (b), and thus we put them in Appendix A.

N	D_N (nm)	A_N (nm)	Q
1	110	220	61
2	120	140	92
3	95	330	255
4	110	300	391
5	105	125	354

Table 3.1. Optimized structural parameters and Q factor for each ring.

3.2.2 Chirped bullseye design with JCMsuite optimizer

According to the investigations in Chapter 3.2.1, the rough optimizations for the hole-bullseye device based on our QD samples and wafer do not seem to work. Therefore, in this section, we relax the requirement on cavity resonant wavelength and again adopt the ring-based bullseye structure, whose rotational symmetry can simplify the 3D simulations back to 2D simulations. This means all the three in-plane parameters W, R_0, and P sketched in Fig.3.9 will be considered during the optimization. Concerning the figure of merit of a high-quality factor, we add an additional chirped section to the regular bullseye [142]. In the new-type chirped bullseye structure (sketched by Fig.3.11), the trench width W_N from ring to ring is not consistent. Instead, the grating pitch P_N gradually increases from the center to the outer rings, while all the rings still have the same thickness. This is realized by introducing a shifting parameter Δ_N, leading to the relations $P_N = P - \Delta_N$ and $W_N = W - \Delta_N$,

where $\Delta_N = \Gamma\Delta_{N-1}$, Γ is the chirped factor ranging from 0 to 1, N is the order of the ring.

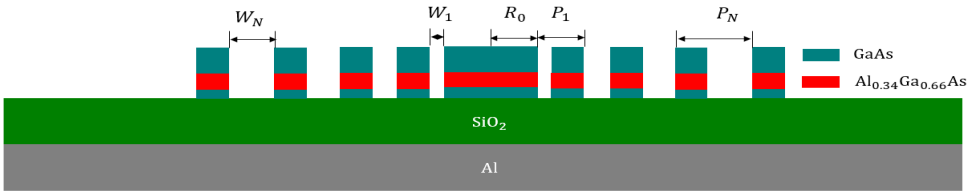

Figure 3.11. Sketch of the chirped bullseye structure.

Under this configuration, we have to know 5 structural parameters to determine the geometry: R_0, W, P, Γ, and Δ_1, where Δ_1 is the initial trench shift of the first ring. We apply the JCMsuite Optimizer to automatically make the optimizations to our target, high Q factor, and good source efficiency. The software can change the parameters within the ranges we set in Table 3.2. The parameters regarding the thickness of each layer and the QD location are consistent with the settings in Chapter 3.2.1. The optimization is carried out for 20-ring geometry.

Parameter	Optimization range
target resonant wavelength λ	850nm∼950nm
R_0	200nm∼500nm
W	100nm∼300nm
P	200nm∼400nm
Γ	0∼0.9
Δ_1	0∼200nm

Table 3.2. Optimization range of the parameters set for JCMsuite Optimizer.

The optimizer is terminated after 2000 times searching, and we finally capture three groups of potential candidates after the automatic optimization. We list their performances (Q factor, efficiency ϵ, Purcell factor F_P), cavity resonant wavelength λ, and the corresponding parameters in Table 3.3.

From this table, we can hardly tell the relation between the compactness or looseness of the structure and the quality factor of the cavity. However, the positive relationship between Q and F_P, and the inverse relationship between Q and ϵ are in line with our predictions for the bullseye cavity. Nevertheless, these three geometries feature groundbreaking high-quality cavities with factors over 1000. The most promising structure is the one with Q=3048 and F_P=10. Although the far-field ϵ is lower than 30%, our experience in design-

Q	ϵ	F_P	λ (nm)	R_0 (nm)	W (nm)	P (nm)	Γ	Δ_1 (nm)
3048	27.0%	10.0	876.6	200.0	153.3	203.3	0.2	77.4
2634	55.4%	6.5	877.3	441.5	161.9	211.9	0.9	16.3
1395	83.0%	1.4	942.5	424.1	100.0	337.0	0.3	0.0

Table 3.3. Three groups of optimizing results and the corresponding parameters from 2000 times searching.

ing the bullseye device convinces us this efficiency can be further optimized by adjusting the thickness of the silica layer. On the other hand, if we choose the geometry with 83% source efficiency, the quality factor is possible to be enhanced with the combination of hole-bullseye design. Based on the above two arguments, we believe our current results shown in this section can provide a good starting point for further optimizations. The interface of the JCMsuite Optimizer is displayed in Appendix B.

3.3 Engineering of open double-cavity

Due to its excellent tunability, the open cavity structure has attracted great attention in the field of QLS in recent years [27, 63, 143]. The original designs are constituted of a bottom DBR section with high reflectivity hosting the quantum emitter layer (QD [27] or 2D emitter [63]), and a tunable top mirror made of dielectric or metal materials. Ref [143] demonstrates a new-type open double-micro-cavity, which consists of a bottom planar λ cavity, sandwiched between two DBRs, and a top open cavity. This kind of design presents the good potential to support the emission of both exciton and bi-exciton while getting rid of the mode crossing [144]. Our design in this chapter is inspired by Ref [143,144], but based on different QD samples and DBR wafers provided by Professor David Gershoni from Israel Institute of Technology, and Professor Christian Schneider from the University of Oldenburg. In this chapter, we will introduce our optimization of open double-cavity for the figure of merit (source efficiency).

3.3.1 Bare planar cavity

Before the investigation of the open double cavity, we slowly start with its bottom part, which is the bare planar cavity visualized in Fig. 3.12 (a). The thickness of AlAs and GaAs in the DBR section is 84.2 nm and 71.2 nm,

respectively. QD is located in the center of the 287.6 nm thick λ cavity and assumed as an in-plane electric dipole. Based on FEM, we present the Purcell factor Γ_t/Γ_0 and the source efficiency Γ_{NA}/Γ_t as a function of QD wavelength in Fig. 3.12 (b) and (c). Due to the lack of field confinement in the planar direction, this structure displays a very slight enhancement in dipole emission and poor source efficiency. But the latter shows broadband behavior in the range of 950∼985nm, where the efficiencies of NA=0.85 and NA=1 are very comparable. This phenomenon is also indicated by the narrow bright ring within a relatively small NA in the far-field inset of Fig. 3.12 (c). However, the non-Gaussian shape implies a bad coupling with the optical fiber. Thus, we need to construct another top open cavity for the enhancement of collection efficiency with good fiber coupling.

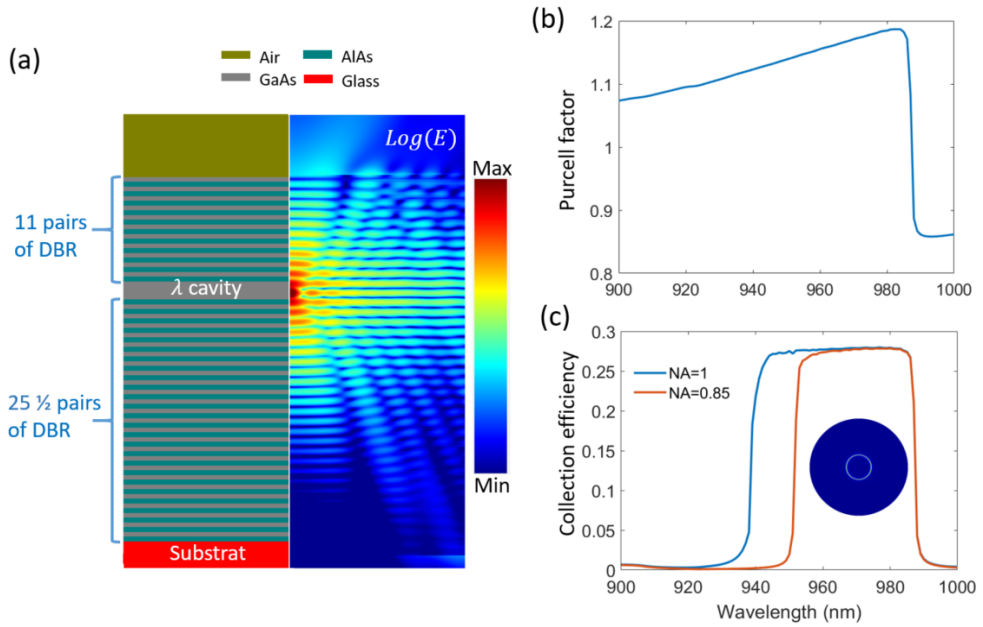

Figure 3.12. (a) Left: Sketched vertical cross-section of the bare planar cavity, constituted of a λ cavity, a top, and bottom DBR, placed on the glass substrate. All the layers are assumed infinitely extended on the horizontal plane. Right: The vertical electric field distribution $Log(E)$ when the QD dipole is located in the center of the cavity. Only the right half of the cross-section is shown, while the other half is symmetrical. (b) Purcell factor and (c) source efficiency within NA of 0.85 and 1 as a function of the emitter wavelength. The inset presents the far-field pattern at 983nm.

3.3.2 Open cavity design with a top-curved gold mirror

As displayed in Fig. 3.13 (a), taking the bare planar cavity illustrated in Chapter 3.3.1 as the bottom part of the open cavity design, we first choose the 33nm thick gold covering a curved glass lens as the top mirror. The diameter and depth of the lens are 5μm and 300nm, respectively. Before optimizing the air separation, we need to confirm the cavity resonance in advance.

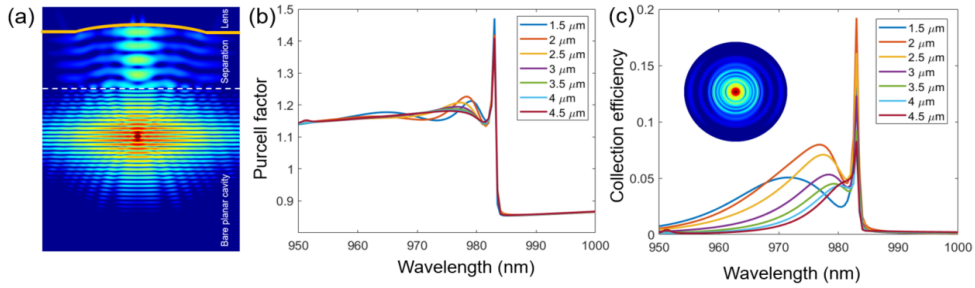

Figure 3.13. (a) The on-resonance vertical electric field distribution $Log(E)$ when the QD dipole is located in the center of the bare planar cavity, which is separated from a 33nm thick gold mirror (yellow area) with an air separation=2μm. (b) Purcell factor and (c) source efficiency within NA of 0.85 as a function of the emitter wavelength for separations from 1.5 to 4.5μm. The inset presents the on-resonance far-field pattern when air separation is 2μm.

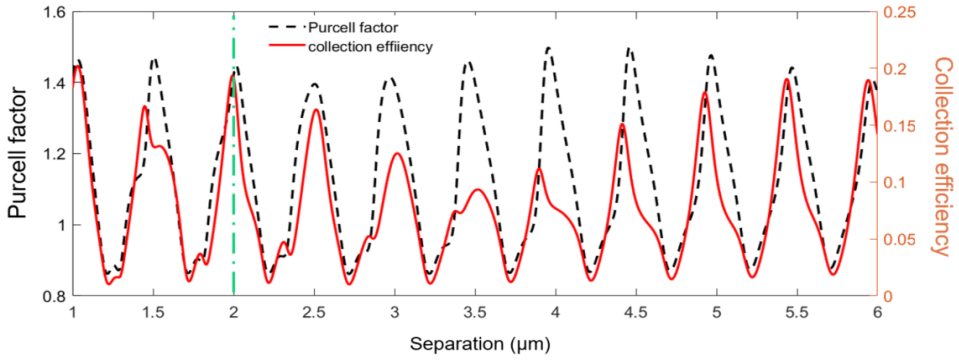

Figure 3.14. Purcell factor and source efficiency as a function of air separation at λ=983nm. The green dashed line indicates the optimum separation.

The peaks in Fig. 3.13 (b) and (c) tell that the gold-mirror-based open cavity only has one resonance (983nm) on the spectrum, no matter the dis-

tance of air separation. Thus, in the second step, we fix the dipole wavelength at 983nm and swipe the separation to look for the best efficiency.

We can observe a clear oscillation in Fig. 3.14, which is caused by the phase change when moving the top mirror up and down in reality. The green dashed line indicates a Purcell factor of 1.4 and an efficiency of 20% at separation=2μm. Contrary to our expectations, implementing a gold mirror reduces the collection efficiency. The monitor of the power traveling through the gold layer confirms the reduction is caused by the absorption of gold. However, comparing the insets of Fig. 3.13 (c) and Fig. 3.12 (c), the top mirror indeed remodels the far-field emission pattern to a more Gaussian-like shape.

3.3.3 Open cavity design with a top-curved dielectric mirror

To get rid of the large photon loss in the metal, in this section, we use the dielectric mirror which alternates between a high refractive index material TiO_2 (n=2.488) and a low index material SiO_2 (n=1.450) to construct the top open cavity [27], where the thicknesses of TiO_2 and SiO_2 are 98.98 nm and 117.20 nm, respectively.

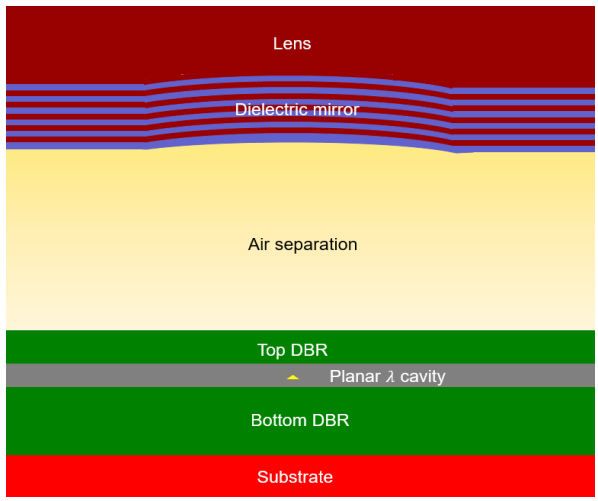

Figure 3.15. Sketch of the open double cavity, where the top mirror is made of alternative changing dielectric materials combined with a glass lens, and the bottom section is the bare planar cavity introduced in Chapter 3.3.1. The yellow triangle represents the QD.

Aiming for a better photon collection, we change the diameter and depth of the lens to 20μm and 400nm, separately, to increase the radius of curvature. The dielectric mirror starts from the TiO_2 layer in the bottom and is departed

from the lower section at a distance. For the open double cavity visualized in Fig. 3.15, we change the number of pairs in the dielectric mirror between 3½, 5½, 7½, and look for the optimized air separation for each.

Same to the optimization procedure presented in Chapter 3.3.2, this section still starts by confirming the cavity resonance. However, contrary to Fig 3.13 (b) and (c), the configuration in Fig. 3.15 leads to multiple peaks of the Purcell factor and efficiency on the spectra, as illustrated in Fig 3.16 (a) and (b). More importantly, these peaks may appear or disappear when air separation is tuned. Thus, we need to consider more resonances, but only those surviving the change of separations can be selected. In the end, we find one survivor in the 7½ configuration, two resonances in 3½ pairs mirror, and three stubborn peaks in 5½ scheme.

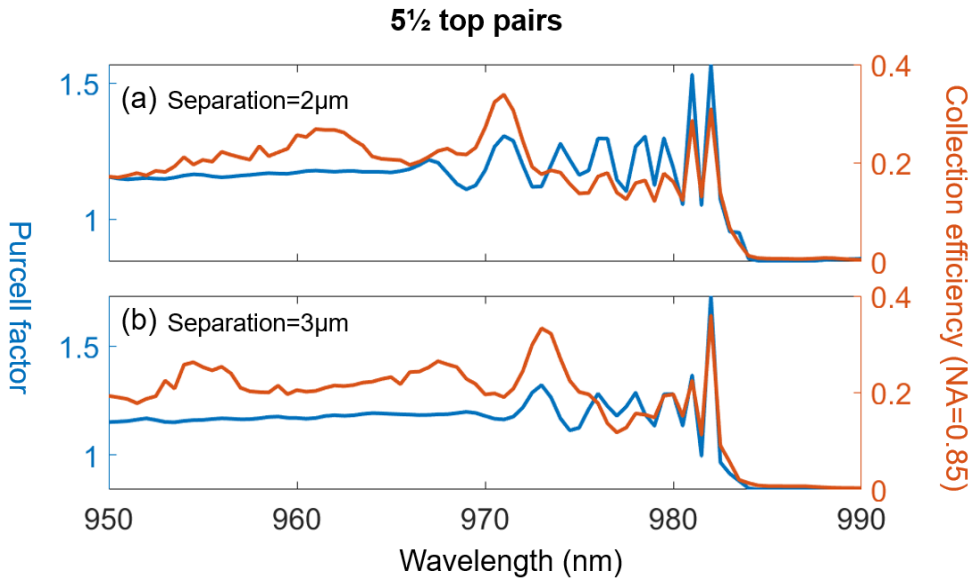

Figure 3.16. Purcell factor and source efficiency as a function of dipole wavelength when there are 5 ½pairs of TiO_2/SiO_2 in the dielectric mirror with a separation from the bottom section of (a) 2 μm and (b) 3 μm, respectively.

Mainly aiming at good source efficiency, we optimize the air separation for each mirror configuration at their cavity resonances, Fig. 3.17 demonstrates an example of 7 ½pairs at a wavelength of 982nm, where the oscillated behavior indicates the phase change due to the dielectric mirror movement. Among all the peaks on the spectrum, we select the one with a good Purcell factor of 3.8 and collection efficiency of 46.0%, which is pointed by the arrow, as

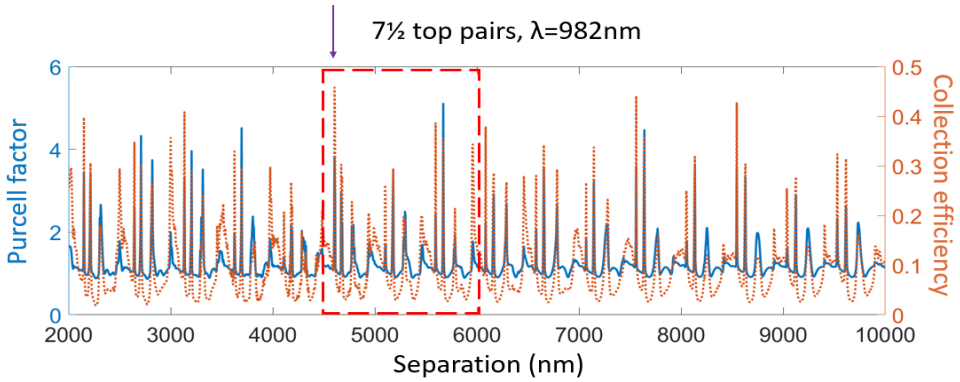

Figure 3.17. Purcell factor and collection efficiency as a function of air separation at λ=982nm when there are 7 ½pairs of TiO_2/SiO_2 in the dielectric mirror. The purple arrow implies the optimized separation of 4.605 μm, displaying a Purcell factor of 3.8 and an efficiency of 46.0%.

Number of pairs in top mirror	Resonant wave-length (nm)	Purcell factor	Collection efficiency	Separation (μm)	Number
7½	982.0	3.8	46.0%	4.605	I
5½	977.5	2.8	59.4%	2.325	II
	981.0	3.5	57.4%	4.210	III
	982.0	3.8	49.5%	6.160	IV
3½	977.5	2.3	57.5%	2.830	V
	984.0	2.1	43.5%	4.505	VI

Table 3.4. Optimizing results for dielectric-mirror-based open double cavity.

the optimized separation value. The responses of other configurations to the air separation look very similar to Fig. 3.17. Thus, we summarize the corresponding best performances in Table 3.4. We can find the source efficiency is enhanced to ∼50% level compared to the ∼20% obtained with a gold curved mirror. On the other hand, the Purcell factor is also 2∼3 times higher than the previous performance in Chapter 3.3.1 and 3.3.2. For easy description, we use Roman numerals I∼VI to number these configurations.

From their far-field profiles visualized in Fig.3.18, we realize not all the patterns are dominated by the fundamental mode. Some of them, like II and V, are clearly occupied by other higher order modes. However, we also observe two better Gaussian shape profiles in I and VI, which indicates a good

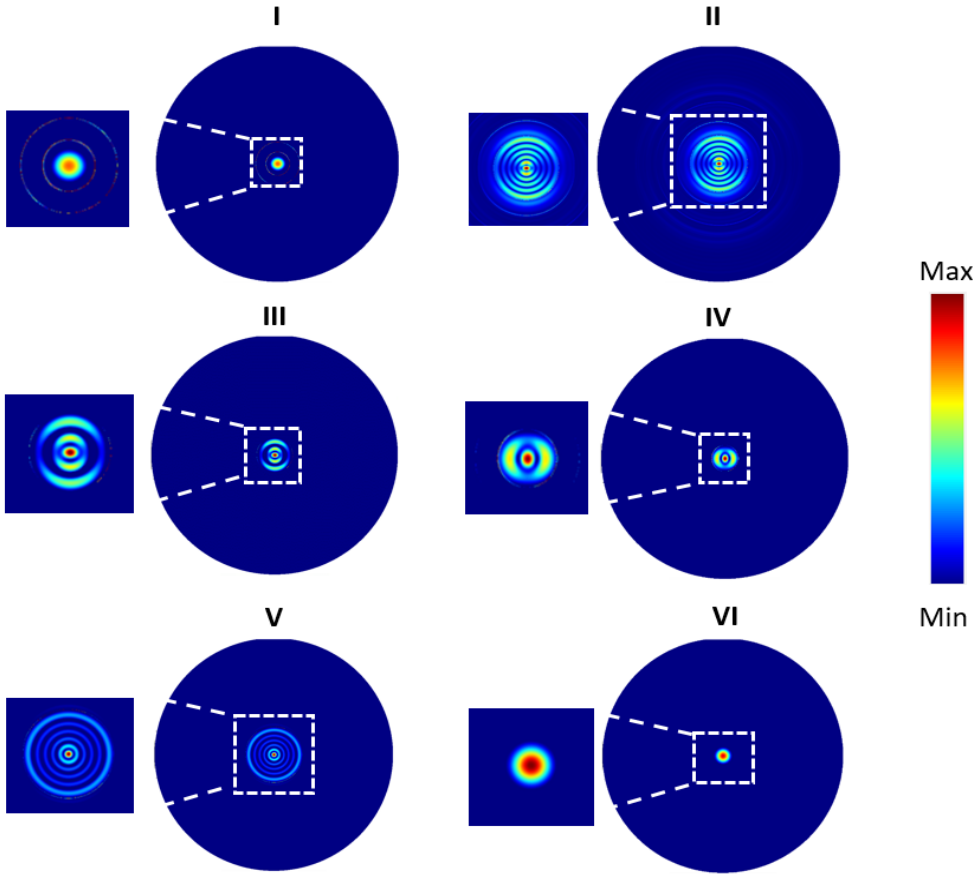

Figure 3.18. Far-field emission patterns of configurations I∼VI. The dashed lines indicate the zooming areas.

potential for fiber mode coupling. To quantitatively prove this argument, in the next section, we will implement a Single-mode optical fiber (SMF) into the simulations and present the numerical results of the total efficiency, which directly points out the fraction of the light funneled into the fiber mode compared to all the energy emitted by the QD.

3.3.4 Coupling with single-mode fiber

In this chapter, we adopt the most commonly used SMF 28 as the top section in our simulations, which is placed 2 μm above the dielectric mirror, this distance is also the thickness of the lens in Fig. 3.15. Since some of the opti-

mizing configurations in Chapter 3.3.3 are dominated by higher order modes, for the target of good fiber coupling efficiency, we have to optimize the air separation again. This time we only simulate the distances that have shown good performances on the spectra, for instance, all the peaks within the red dashed frame in Fig. 3.17. Here, we still use the configuration 7 ½pairs at resonance 982nm to illustrate. Comparing Fig. 3.19 and Fig. 3.17, we can see Purcell factor is almost unaffected by the SMF because it's distant from the QD location. However, the non-Gaussian far-field profiles make the total source efficiency fall to 0, except two peaks survived, which should thank the Gaussian-shape far-field patterns.

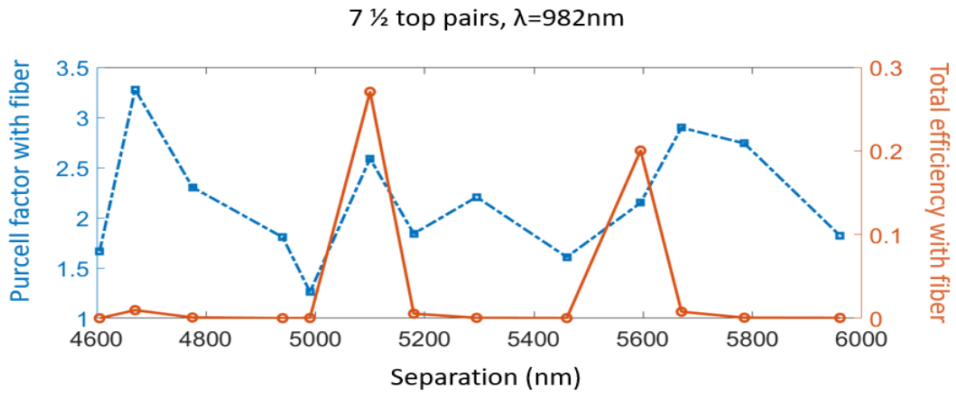

Figure 3.19. Purcell factor and total fiber-coupled collection efficiency as a function of air separation at λ=982nm when there are 7 ½pairs of TiO_2/SiO_2 in the dielectric mirror.

Number of pairs in top mirror	Resonant wave-length (nm)	Purcell factor	Collection efficiency	Separation (μm)
7½	982.0	2.6	28.0%	5.100
5½	981.0	1.7	18.5%	4.585
	982.0	2.1	24.8%	6.575
3½	984.0	2.1	25.0%	4.505

Table 3.5. Optimizing results for SMF-coupled dielectric-mirror-based open double cavity.

We carry out the same procedure for other configurations and present the results in Table 3.5. The champion design with a Purcell factor of 2.6 and total efficiency of 28.0% is the 7½ configuration. However, the performances of the other two are still comparable to the champion. Thus, our design provides

tolerant choices regarding the number of dielectric layers in real fabrications. Comparing Table 3.5 and 3.4, we can find the resonances 977.5nm are removed. This is because there is no fundamental mode excited at this wavelength, which is proved by less than 1% coupling efficiency with the SMF no matter how we move the top mirror.

3.4 Discussion and Conclusion

In this chapter, we presented and discussed three types of vertical-emission SPSs. The first nanopost structure is a simple but effective candidate. We adopted FMM and proposed a design procedure under the SMM framework. Our nanopost device features a remarkable Purcell enhancement of 6.3 to the fundamental cavity mode, combined with a decent and broadband far-field collection efficiency of 54%. We also discussed spatial misalignment of the dipole in-plane location and found our device keeps a good tolerance to the source efficiency, while the Purcell effect is more sensitive to the off-axis scheme. For more accurately describing the interactions between HE_{11} mode and all the other background modes, an extensive work [133] displays the breakdown of SMM and gives a detailed explanation based on the full model scheme. In this work, an asymmetric behavior appears on the spectrum, which means the SE curve is modified by other higher order modes. After finding these modes, we applied the QNM theory to describe the contributions from them. In the end, the spectra obtained via FMM and QNM approach presented a good agreement.

To get a high-quality cavity, we turned our attention to the new-type bullseye structures. After implementing two optimization strategies to the hole-bullseye device, we found the Q factor can be improved to four or five hundred, and at the same time, the high Purcell and source efficiency are still maintained. This is a breakthrough compared to regular CBG devices, however, we are still far from the demanding high-quality cavity. The chirped bullseye is able to achieve very strong in-plane light confinement, but generally, this means a slight vertical transmission and collection. Thus, we use the FEM optimizer to look for the structure that can simultaneously maintain a high quality and a reasonable source efficiency. The found structures are not satisfying yet, but they can be better designed by integrating holes and chirped sections in CBG, or by tuning the thicknesses of the materials.

The open cavity provides good tunability to the SPS devices. We made this design combined with the planar cavity wafers currently in hand and

looked for the potentially optimal open double cavity structures for the target of good coupling with commercial SMF. Despite optimizing the structural parameter of the cavity, the design with gold mirror displayed unreasonable efficiency due to the absorption by the metal. However, this can be restored by the dielectric materials. In the end, the total source efficiency, concerning the fiber coupling, shows a decent value of 28% when the dielectric mirror is placed by a proper distance above the bottom planar cavity.

CHAPTER 4

Designs and discussions of on-chip waveguide-based single-photon sources

As mentioned in Chapter 3, we classify the nano-cavities into two groups considering photon collecting directions, vertical or on-chip. This chapter will mainly focus on the latter. As a piece of background information, this work is fully funded by EU MSCA QUDOT-TECH project. In this project, 15 Ph.D. students hosted by different universities and research institutions collaboratively work with the ambition of building a fully integrated quantum network. One of the key components in the network is the on-chip SPS, which can be conveniently coupled to the transmission waveguide and the superconducting nanowire single photon detector (SNSPD) for manipulating and detecting the generated single photons. In this work, we choose the semiconductor ridge waveguide as the platform under the consideration of two advantages: low propagation loss [73, 74] and selective guidance of photons with specific polarization orientation [75]. Applying this strategy, the coupling efficiency from an InAs QD to a bare GaAs ridge waveguide located on the top of a low-index silica substrate has achieved ∼60% [75]. Recently, researchers presented a rectangular DBR holes-based SPS featuring an efficiency of 86% [76], and a value of 73% in a circular-hole DBR device [77]. Nevertheless, realizing a near-unity efficiency comparable to the state-of-the-art micropillar [132] or PC waveguide SPS [65, 68–71] in semiconductor ridge waveguide platform is still of critical importance and under pursuit. One possible solution is the tapered cavity, which can help to reduce the losses into radiation via an adiabatic transition

from fundamental cavity mode to Bragg mirror mode [78,79], and thus can be fused into the ridge waveguide SPS design to approach the source efficiency that we are pursuing.

Chapter 4.1 is published in our paper [145], where we not only introduce our taper-based champion nanobeam cavity design but also propose an optimization recipe to achieve arbitrarily high efficiency in the QD-ridge-waveguide platform. Considering the challenge in fabrication, the scale-up structures are discussed and designed in Chapter 4.2. A follow-up perspective on suppressing the emission from unwanted polarization for the target of a higher source efficiency is also included in Chapter 4.3. The last part of this chapter talks about the integration of the waveguide with the SNSPD, which is in collaboration with another student in the QUDOT-TECH project, and thus the materials of the structure are different from our nanobeam cavity.

4.1 Champion design

4.1.1 General Concept

The structure under consideration in this work is schematically depicted in Fig.4.1. An infinitely long GaAs ridge waveguide surrounded by air is on the top of a substrate with a lower index material SiO_2. The Inset of Fig.4.1 shows the fundamental Transverse electric (TE) mode, denoted by mode M, is well confined inside the structure instead of leaking into the substrate, mainly thanks to the significant index contrast between GaAs and SiO_2. An InAs QD with the free-space emission wavelength of 940nm is embedded on the central axis of the waveguide. We build a cavity composed of two sets of DBRs formed by cylindrical air holes around the QD to improve its SE rate with the help of the Purcell effect. Considering SE wavelength, the refractive indexes are set as $n_{GaAs} = 3.45$, $n_{SiO_2} = 1.45$, and $n_{Air} = 1$ [75]. We adopt the FEM based commercial solver (JCMsuite [141]) and the usage of HPC cluster hardware [146] to perform fully three-dimensional numerical simulations in this work. The self-assembled semiconductor QD, as introduced in Chapter 1.2, typically features a several times larger horizontal than a vertical extension, and thus can be modeled as a linear in-plane xy-polarized dipole under the consideration of the dipole approximation [116, 141, 147]. The red double-headed arrow in Fig. 4.1 depicts the orientation of an xy-polarized dipole. θ is the polarization angle, randomly distributed in the xy-plane. Since one can always project the

arrow onto two base axes, we consider the total emission from the sum of two cases: purely x-polarized ($\theta = 0$) and purely y-polarized ($\theta = \pi/2$) dipoles.

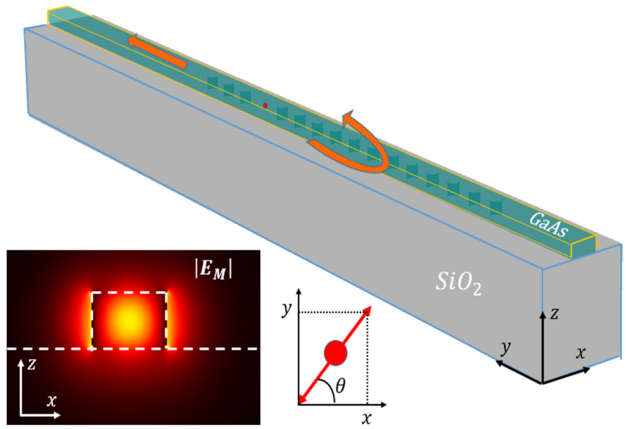

Figure 4.1. Sketch of the GaAs nanobeam cavity waveguide on top of the SiO_2 substrate. An InAs quantum dot denoted by the red circle is embedded in the center of the cavity sandwiched between two mirrors formed by cylindrical air holes. The red double-headed arrow represents the dipole orientation, which can always be projected onto two base axes x and y. The curved arrow indicates most of the light going to the bottom mirror is reflected back to the cavity, and this part escapes from the top mirror along with the light emitting upwards, as demonstrated by the straight arrow. Inset is the 2D mode profile of the fundamental TE mode M propagating along the bare ridge waveguide. The figure is taken from Ref. [145].

Correspondingly, we define $P_{x(y)}$ as the power emitted by the x/y-polarization configuration. The Purcell effect describes the enhancement of the QD SE rate by the nanostructure. The Purcell factor can quantify this effect and is defined as:

$$F_{x(y)} = \frac{P_{x(y)}}{P_0}, \tag{4.1}$$

where P_0 is the power emitted by the QD in the bulk material. As the figure of merit, the coupling efficiency of an xy-polarized dipole is given by [148]:

$$\epsilon_{xy} = \frac{P_{M,x} + P_{M,y}}{P_x + P_y}, \tag{4.2}$$

where $P_{M,x(y)}$ denotes the power emitted by the x/y-polarized dipole funneled into the mode M and is evaluated by the overlap of the scattered electromagnetic field and the mode M at the waveguide cross-section, which is pointed by

the arrow in Fig.4.1. When the dipole is on the central axis of the waveguide, it always yields $P_{M,y} = 0$ [75, 148]. Therefore, we simplify the notation in the following by P_M only referring to $P_{M,x}$. We also investigate the efficiency of the source only under the x-polarized configuration, defined as:

$$\epsilon_x = \frac{P_M}{P_x}, \tag{4.3}$$

From the aspect of the numerical simulations in JCMsuite, we use the following solvers for solving different categories of problems in the whole work: a propagation mode solver for computing waveguide modes, a mode solver for computing Bloch modes for the cylindrical air hole unit cell, a scattering solver for computing scattered field with a dipole excitation and deducing Purcell factor, and a mode solver for computing the modes of the full structure and deducing Q factor [141].

4.1.2 QD coupled to a ridge waveguide

First, we investigate the dependence of ϵ_{xy} on the waveguide geometry for an infinitely long and pristine waveguide (with no holes), whose cross-section and top view are depicted in Fig.4.2(a) and (b). We consider a rigde waveguide of height h and width w in the ranges $h \in [100\text{nm}, 300\text{nm}]$, $w \in [200\text{nm}, 580\text{nm}]$ respectively, with a step-size $\Delta h = \Delta w = 10\text{nm}$. Transparent boundary conditions are implemented using Perfectly matched layers (PML) [141] to perform the infinitely spatial scattering simulations. Then, we compute the mode overlap and the emitted power by x/y- polarized dipole for each set of parameters to calculate the Purcell factors and efficiencies according to Equations (4.1-4.3), and the results are shown in Fig. 4.2(c)-(g). The white areas correspond to the specific sets where no guided mode can be found. Comparing Fig.4.2(c) and (d), the Purcell factor of y-polarized dipole F_y is more sensitive to the dimensional variation than that of x-polarized dipole F_x. This is because the oscillation axis of the y-polarized emitter (y-axis) is perpendicular to the waveguide cross-section (xz-plane) [148]. Next, we consider the sum of the power extracted from the top and bottom outputs, $P_{M,\text{top}}$ and $P_{M,\text{bot}}$, as shown by the arrows in Fig.4.2(b). In principle, P_M=$P_{M,\text{top}}$+$P_{M,\text{bot}}$. Fig.4.2(e) shows P_M normalized by its maximum value. P_M increases by reducing the waveguide dimensions to an optimum mode confinement.For a purely x-polarized emitter, the coupling efficiency ϵ_x can reach as high as 95%. In addition, the area with a small cross-sectional size can maintain high efficiency of over 90%, as shown in the dark-red area in Fig.4.2(f), where we can also

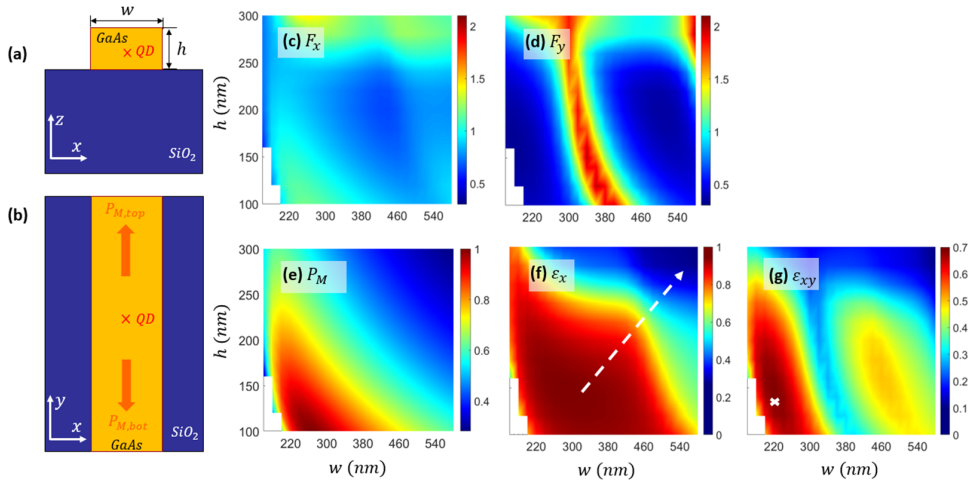

Figure 4.2. (a)/(b) Front view/top view of the QD-bare ridge waveguide system with physical dimensions: w= waveguide width, h= height, and material properties: substrate SiO_2 (dark blue), waveguide GaAs (yellow), embedded QD (red cross). P_M denotes the power emitted by x-polarized dipole into the fundamental propagation mode M. In this bare waveguide, two opposite arrows indicate two equal output channels. (c)/(d) Purcell factors $F_{x/y}$ for x/y-polarized dipole, (e) mode coupling power P_M normalized by its maximum value, and (f)/(g) coupling efficiencies ϵ_x/ϵ_{xy} for x/xy-polarized dipole as functions of waveguide width and height. The white cross represents the physical dimensions yielding the optimum efficiency. The figure is taken from Ref. [145].

see ϵ_x diagonally drops, as indicated by the arrow. The reason is that a wider structure supports additional guided modes, thus decreasing the relative emission into the fundamental TE mode. The white cross in Fig.4.2 (g) represents the geometric parameters $h = 140$nm and $w = 220$nm yielding a maximum coupling efficiency ϵ_{xy} of 70% for an xy-polarized emitter. The structures that we investigate in the following will inherit this set of dimensions.

Comparing Fig.4.2 (d), (f) and (g), higher values of ϵ_{xy} coincide with high ϵ_x and low F_y. Moreover, the bright/dark areas in Fig.4.2 (g) almost perfectly correspond to the dark/bright areas in Fig.4.2 (d). This is due to $P_{M,y} = 0$ and the strong dependence of efficiencies on the dipole orientation (x). Therefore, the distribution of ϵ_{xy} relies on the interplay of ϵ_x and F_y, and a relative suppression of F_y will significantly contribute to a higher ϵ_{xy}. However, a bare waveguide always features $P_{M,\mathrm{top}} = P_{M,\mathrm{bot}}$, which means we will always lose 50% of the light if we only collect from the top. Therefore, in the following, we will try to make $P_{M,\mathrm{top}} \gg P_{M,\mathrm{bot}}$ by engineering a highly reflective bottom mirror.

4.1.3 Design concept and results for a DBR in a ridge waveguide

As depicted in Fig.4.3 (a), the DBR mirror is composed of cylindrical air holes with a number of N_{bottom}. The hole radius r and the distance between successive hole centers, periodicity p_h, should be carefully selected to ensure a good reflection from the bottom mirror at the designed SE wavelength 940nm. We find the correct periodicity by performing a photonic band structure calculation for 3D unit cell of the PC in a 1D-periodic arrangement for different values of p_h and r, as shown in the inset of Fig.4.3 (b). The yellow shade indi-

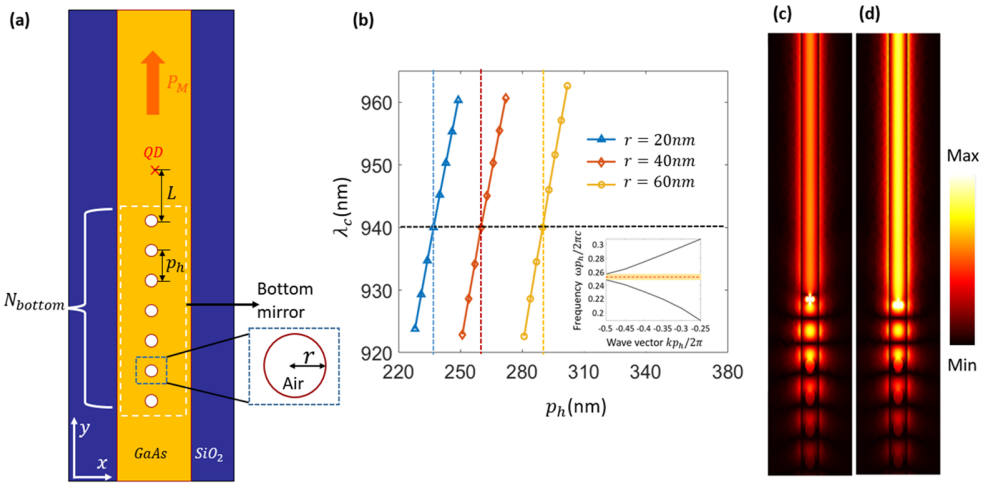

Figure 4.3. (a) Top view of the QD-ridge waveguide system with bottom mirror, formed by an array of periodic and uniform holes. N_{bottom} denotes the number of holes in the bottom mirror, L and p_h is the distance from QD to the bottom mirror and between two adjacent periods. Inset shows the enlarged view of one of the air holes with the radius of r. Emitted photons can only propagate through one output channel, as the arrow indicates. (b) Center wavelength λ_c, obtained from the bandgap calculation of three different hole radii ($r = 20$nm, $r = 40$nm, $r = 60$nm), as a function of periodicity p_h. The intersections of horizontal and vertical dashed lines imply three suitable p_h to reach λ_c=940nm (designed wavelength). Inset shows the bandgap (yellow shade) of a period with $r = 20$nm, $p_h = 237$nm, where the red dashed line indicates the center frequency ($\lambda_c = 940$nm). (c)/(d) Field profile $|E_x|$ when QD is at a random position/an antinode relative to the bottom mirror under the same color bar. The figure is taken from Ref. [145].

cates the bandgap [149] of the periodic structure with parameters $r = 20$nm, $p_h = 237$nm, in the center of which a red dashed line denotes its center wavelength λ_c precisely at 940nm. For the highest possible reflectivity in DBR, the band gap should be engineered exactly around the SE frequency. After scanning the periodicities for three radii that we would investigate in the following

and extracting all the corresponding center wavelengths, we finally get the impact of p_h on λ_c, as shown in Fig.4.3 (b). It reveals that a longer period is necessary for a larger hole or a longer wavelength to achieve the greatest reflection. The intersections of the dashed lines in Fig. 4.3 (b) represent the optimal p_h of three periodic structures at the designed wavelength 940nm. They are $p_h = 237\text{nm}(r = 20\text{nm}), p_h = 260\text{nm}(r = 40\text{nm}), p_h = 290\text{nm}(r = 60\text{nm})$, respectively. By applying these parameters, we can expect a fairly high bottom reflection to appear in this structure.

Next, a stronger Purcell enhancement can be achieved by the constructive interference between the forward-propagating photons and the ones reflected at the bottom mirror [148], which requires the dipole to be precisely at an antinode relative to the mirror. We first place the emitter at a random distance L to the bottom mirror to obtain a field profile, where we can observe the position of the antinodes. As shown in Fig.4.3(c), there are three antinodes between the dipole and the mirror, indicated by three bright standing wave patterns. The second step is to choose one of the antinodes and relocate the emitter there. Here, we avoid the first antinode in case there is any influence induced by the close distance between QD and DBR. In this structure, we choose the third antinode to locate the dipole, and the field profile is shown in Fig.4.3 (d), where the output signal is much stronger than that in Fig.4.3 (c). As mentioned above, this results from perfect constructive interference when the emitter is precisely at the antinode. The quantitative analysis for the dipole misalignment will be discussed in Chapter 4.1.5. For different radii, the distances of QD to the bottom mirror used in this work are given as follow: $L = 289\text{nm}(r = 20\text{nm}), L = 298\text{nm}(r = 40\text{nm}), L = 312\text{nm}(r = 60\text{nm})$. Although we observed an enhanced SE rate and $P_{M,\text{top}} \gg P_{M,\text{bot}}$ by only implementing a bottom mirror, we are still pursuing a better Purcell factor and higher source efficiency, as shown in Chapter 4.1.4.

4.1.4 QD in nanobeam cavities with and without taper

The third step in the design procedure is to construct a complete cavity, in which two sets of DBR sandwich the QD in the center, and thus cavity length is twice as long as L. By applying the parameters designed in the previous step, the cavity will further enhance the QD SE through a more substantial Purcell effect. Fig.4.4 (a) is the sketch of a QD-nanobeam cavity waveguide coupling system. Here, we design a top mirror with a higher transmission than the bottom one, which is achieved by using less holes. For a purely x-polarized dipole, part of the total emitted power P_T funnels into the waveguide

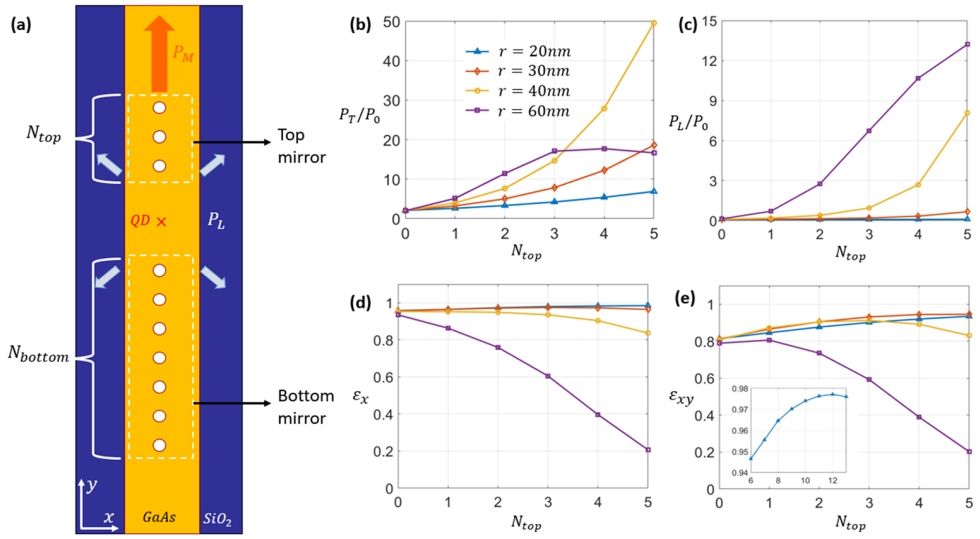

Figure 4.4. (a) Top view of the QD-nanobeam cavity waveguide (regular DBR) coupling system. $N_{\text{top}}/N_{\text{bottom}}$ is the number of periods in top/bottom mirror. For x-polarized dipole, P_M denotes the power funneled into fundamental mode M, all the other power lost by radiation P_L is depicted by the small arrows, total power $P_T = P_M + P_L$. (b)/(c) Emitted/lost power $P_{T/L}$ and (d)/(e) coupling efficiencies ϵ_x/ϵ_{xy} for x/xy-polarized dipole as a function of N_{top}. Inset shows the maximum efficiency ϵ_{xy} can reach 97.7% with parameters: $r = 20$nm, $N_{\text{top}} = 12$. The figure is taken from Ref. [145].

fundamental guided mode M, denoted by P_M. The rest lost into radiation, named P_L, mainly appears at the interfaces of the cavity and the DBRs.

Fig.4.4 (b)-(e) show the impact of the number of periods in top mirror N_{top} on the SE properties and coupling efficiencies under four sets of configurations. Generally, when N_{top} increases, the top reflectivity increases as well. For each data point, N_{bottom} is accordingly increased to ensure the bottom reflectivity stays higher. Here, we state that the parameters used in the design of $r =$ 30nm are $p_h = 248$nm, $L = 291$nm. Fig.4.4 (b) demonstrates the normalized P_T emitted by an x-polarized dipole as a function of N_{top}. In the range of $N_{top} \in [0, 5]$, the large size design ($r = 60$nm) has already reached the highest Purcell factor. In contrast, the curves for 20, 30 and 40 nm are still going up but will not increase infinitely. Due to the scattering taking place at the cavity-DBR interface, there is a trade-off between the enhancing quality factor and the scattering loss when increasing N_{top}, and therefore those curves will reach a maximum at a larger N_{top}. As N_{top} increases, the reflectivity from the top becomes comparable to that from the bottom, and thus more light into

the free space leads to a rise in P_L, as shown in Fig.4.4(c). Here, the structure with the smallest size ($r = 20$nm) yields the lowest P_L. Fig.4.4 (d) and 4(e) confirm indeed that a smaller radius is beneficial for suppressing P_L, as both ϵ_x and ϵ_{xy} achieve much higher values in this regime.

We find a maximum efficiency ϵ_{xy} =97.7% for $r = 20$nm and $N_{\text{top}} = 12$ (and a corresponding $N_{\text{bottom}} = 85$), accompanied by a Purcell factor of $F_x = 38.6$, and a Q factor of 668. As the supplementary information to Fig.4.4(e), we show the maximum efficiency ϵ_{xy} for four different radii and the corresponding period configurations in Table 4.1. The optimum efficiency increases with a smaller hole radius thanks to the reduction in scattering losses. Still, it pays a cost for more periods due to the reduced reflection from a single hole. A single computation in the parameter scan is performed with an accuracy setting yielding an estimated numerical relative error of 0.5% for Q and of 0.1% for ϵ_{xy}. The corresponding discrete problem has a dimension of N=14836908 and is solved with a RAM consumption of 500GB and with a computation time of roughly 4 hours, using 6 nodes on a standard workstation. The numerical error has been estimated using a numerical convergence study with gradually increasing numerical accuracy settings.

To make a more fabrication-friendly design, the last step in the design procedure is to find a structure with fewer periods but which can keep a near-unity coupling efficiency simultaneously. On one hand, the $r = 20$nm platform effectively suppresses the scattering loss into the free space but takes a large number of periods because a single period contributes very little to the overall reflectivity. On the other hand, the 40nm platform achieves high bottom reflection with few holes but features stronger scattering losses due to a significant mode mismatch between the Bloch mode in the DBR mirror section and the cavity mode. One way to take advantage of both configurations is to implement a taper section [150–152] in the bottom mirror, where the hole radius gradually increases from 20nm in the vicinity of the QD to 40nm. We thus consider a bottom mirror consisting of N_{regular} holes of radius 40nm and

Radius(nm)	N_{bottom}	N_{top}	Maximum ϵ_{xy}
20	85	12	97.7%
30	35	5	94.6%
40	15	3	91.3%
60	10	1	80.6%

Table 4.1. Maximum coupling efficiency ϵ_{xy} under different configurations

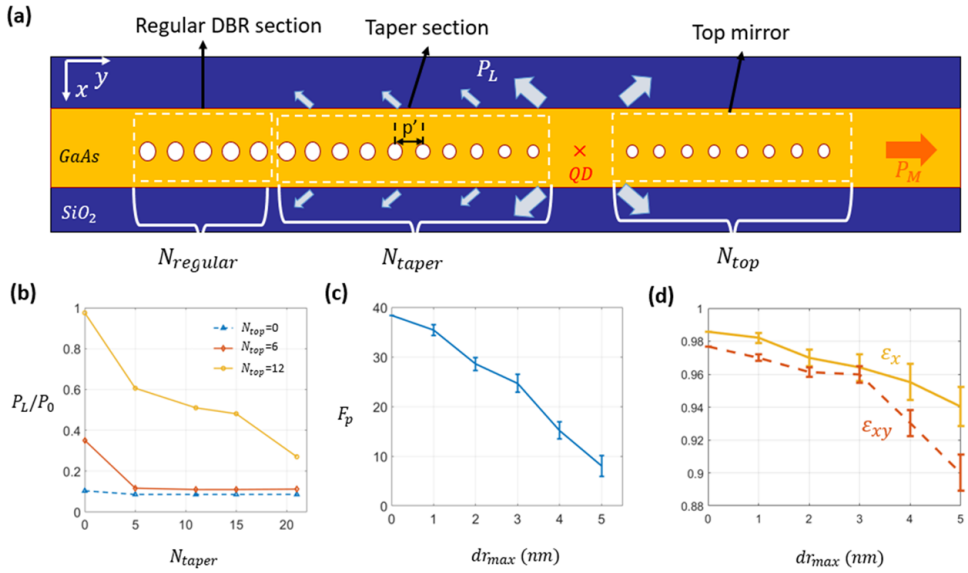

Figure 4.5. (a) Top view of the QD- taper cavity waveguide structure. The bottom mirror is divided into a taper section and a regular DBR section, whose number of holes is described by N_{taper} and N_{regular}. (b) Power into radiation modes P_L as a function of N_{taper}. (c) The Purcell factor for x-polarized dipole and (d) coupling efficiencies ϵ_x/ϵ_{xy} for x/xy-polarized dipole as a function of maximum radius deviation dr_{max} from the perfectly designed holes in the entire structure. All the data shown in (c) and (d) are obtained from 10-times simulations. The figure is taken from Ref. [145].

a taper section including N_{taper} holes, as shown in Fig.4.5 (a), and the new variable distance between two holes p' is given by $p' = (p_{h1} + p_{h2})/2$, where p_{h1} and p_{h2} are the individual periodicities of two adjacent periods. The principal power loss in this platform still appears at the interfaces of the cavity and two mirrors, as depicted by the thick arrows.

However, the increased size in the taper section also introduces additional scattering loss, denoted by the small arrows in Fig.4.5(a). We investigate the impact of N_{taper} on the normalized P_L, as shown in Fig.4.5 (b). We can find increasing N_{taper} will effectively suppress P_L. In our investigations, the cavity effect is indispensable, and therefore we employ a large N_{taper} in the design. Then, we propose an optimum new design yielding a coupling efficiency $\epsilon_{xy} = 97.6\%$, a remarkable Purcell factor of 38.3, and a Q factor of 616 with the parameters $N_{\text{regular}} = 9$, $N_{\text{taper}} = 21$, $N_{\text{top}} = 12$. Compared with the previous result in this section, which is obtained via 20nm-hole regular DBR nanobeam cavity, we achieve identical performance but with only 1/3 of

the total periods in the bottom mirror, contributing to a smaller mode volume and, in turn, a broader bandwidth.

In principle, the figure of merit ϵ_{xy} can be further improved by using a longer taper section and smaller holes, but these come at the price of a much longer structure and heavier calculations. Under the premise that the minimum design radius is 20nm, we don't implement a similar taper section in the top mirror and instead, keep the regular DBR. This avoids the additional power loss introduced by the increased radius in the taper.

4.1.5 Investigation of the impact of fabrication tolerances on the performance of the SPS

Considering the imperfections that will appear in the actual situations, the tolerance study for the optimum QD-taper cavity platform is carried out by randomly changing the radii of the well-designed holes. Fig.4.5 (c) and (d) demonstrate the Purcell factor and efficiencies as a function of the maximum radius deviation dr_{max} between the designed radii and the possible imperfections in fabrication, which means that each hole radius is changed by an individual random amount in the interval (0, dr_{max}). Even under a 5nm deviation, our platform is still robust on ϵ_x and ϵ_{xy}, keeping the performances of over 90% with a standard deviation of 1%. However, the Purcell factor is more sensitive to imperfect situations. This is because a misalignment of the new antinode with respect to QD position leads to poor constructive interference.

In Chapter 4.1.3, the field strength comparison between Fig.4.3 (c) and (d) implies the QD-cavity coupling might highly depend on the accuracy of the QD position. To offer a more quantitative analysis, we investigate the impact of QD misalignment on the SPS performance. In this subchapter, we still consider the on-axis dipole but change its position along the axis. We define ρ as the deviation of QD position from the ideal center in the cavity, and this value varies in the range [-(L-r_b),(L-r_t)] when we assume $\rho = 0$ is the cavity center. Here, L is the half cavity length, and r_b (r_t) is the radius of the hole closest to the cavity in the bottom (top) mirror. The peaks and valleys in Fig.4.6 (a) correspond to the QD at the cavity's antinodes and nodes. The wave shape is the consequence of walking in the cycle between constructive and destructive interference. The green shade area reveals that a relative QD position deviation of 50nm is tolerable with a cost of 50% Purcell enhancement. In Fig.4.6 (b), the efficiencies ϵ_x and ϵ_{xy} present an even broader

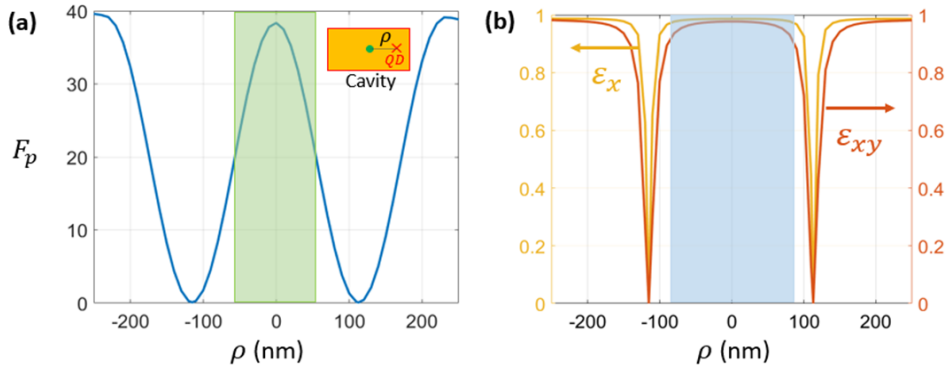

Figure 4.6. (a) Purcell factor for x-polarized dipole and (b) coupling efficiencies ϵ_x/ϵ_{xy} for x/xy-polarized dipole as a function of ρ, which is the deviation of on-axis QD (red cross) from ideal cavity center (green dot). The shade areas indicate the tolerance ranges of the QD-taper cavity waveguide SPS on the imperfect QD position. The figure is taken from Ref. [145].

spatial linewidth, denoted by the blue shade area. Within a 90nm QD-cavity center deviation, our platform can still perform a more than 90% coupling efficiency.

4.2 Scale-up discussions and tolerant designs

Now that the design is finished, we try to bring out the fabrication. However, we meet a big challenge with respect to the small holes in our champion design. The irregular shape and the etch depth that cannot be fully grasped might thoroughly destroy the SPS performance. Thus, we turn attention to the wider nanobeam cavity design, which may bring more tolerance to the fabrication. Then we consider a 300nm wide, 150nm high GaAs waveguide placed on top of a glass substrate. The target wavelength is changed to 850nm, which is a typical value of a single-photon emitter in strained WSe2 monolayer [153]. We follow the nanobeam cavity design procedure introduced in Chapter 4.1 and start from the bandgap calculation to look for the proper pitch distance between the air holes in the DBRs. We expect to see a clear and clean bandgap like the one that we find in Chapter 4.1.3, visualized in Fig.4.7 (a). However, no matter how we change the diameter of the holes in the structure discussed in this subchapter, we can never find a similar bandgap. As demonstrated in Fig.4.7 (b), all the dots represent the modes found at a specific wave vector.

Since no frequency can survive from this band diagram, we are not able to determine a suitable periodicity in this configuration.

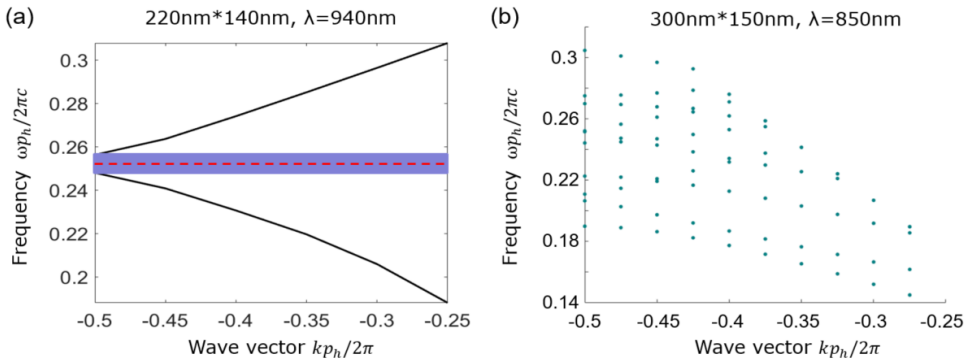

Figure 4.7. Band diagrams of the 3D unit cells in a 1D-periodic arrangement: (a) waveguide dimensions w=220nm, h=140nm, target wavelength 940nm, (b) w=3000nm, h=150nm, target wavelength 850nm. The purple shade in (a) indicates the bandgap, where the target frequency is in the middle.

To find the solution, we have to figure out the failure reason. Comparing the two configurations (A: 220nm*140nm, $\lambda = 940$nm, B: 300nm*150nm, $\lambda = 850$nm) in Fig.4.7, we start the analysis from two aspects: dimensions and wavelength. Fig.4.8 (b) illustrates the relation between the bandgap center wavelength λ_c and the pitch distance p_h in configuration A. No matter the value of the hole diameter D, λ_c and p_h always show a linear relation. Therefore, when the target wavelength is changed from 940nm to 850nm, we need to consider a smaller pitch in Configuration B than that in A. This means the upper size limit of D gets smaller, complying with the most basic requirement $D < p_h$. Now you may ask, is there a minimum size requirement for the holes? The answer is yes, especially when the dimensions of the waveguide are enlarged. The red and the yellow dashed frames in Fig.4.8 (a) roughly separate one period in the DBR into two parts.

These two regions typically feature one higher effective index (red) and one lower effective index (yellow) due to the presence of air holes in the structure. The deviation of the indexes “opens” the bandgap. Now considering a fixed diameter and only broadening the waveguide, the relative deviation of effective indexes would decrease, and the bandgap is at risk of being “closed”. Although we are not clear how low the deviation will make the bandgap disappear, we do know there is a minimum requirement D_{min} for the hole diameter, which

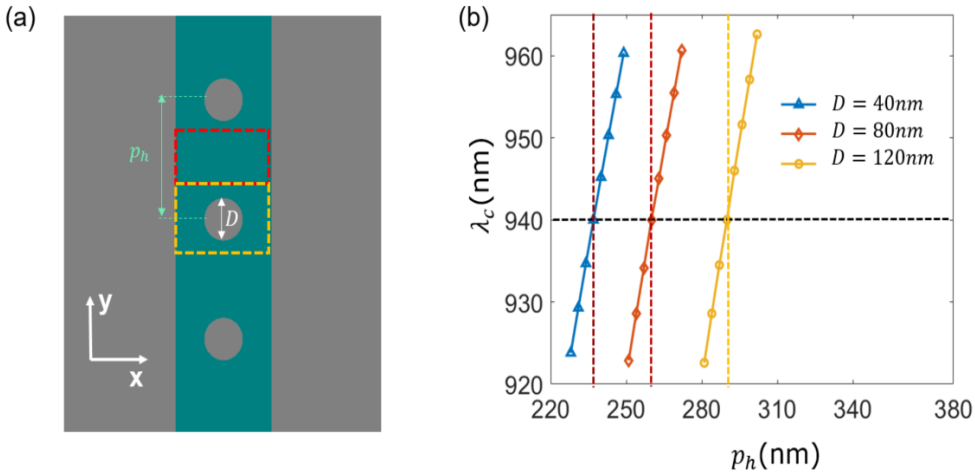

Figure 4.8. Band diagrams of the 3D unit cells in a 1D-periodic arrangement: (a) Top view of three periods in nanobeam DBR. (b) Center wavelength λ_c, obtained from the bandgap calculation of three different hole diameters (D = 40nm, D = 80nm, D = 120nm), as a function of periodicity p_h. The intersections of horizontal and vertical dashed lines imply three suitable p_h to reach λ_c=940nm. Picture taken from Ref. [145]

means $p_h > D > D_{min}$ should be satisfied if we expect to see a proper bandgap. Now we can provide a possible explanation for the absence of bandgap in Fig.4.7 (b). Compared to Configuration A, the shorter target wavelength in Configuration B leads to a decrease in p_h, while the broader waveguide results in an increase of D_{min}. The combination of two changes could possibly cause the reversal relation $D_{min} > p_h$, and this might be the failure reason when looking for a bandgap with Configuration B.

To find out the solution, we need to separate the problem into two directions: one along x axis and another along y axis. In y direction, we keep the holes at a safe distance from each other, which means $p_h > D$ must be complied. Concerning the deviation between the effective indexes of two regions, which also must be large enough, we extend the hole dimension in the x direction, meaning that the elliptical holes displace the round holes. Under this new configuration, the area of air in the yellow region becomes larger, which makes the bandgap easier to "open".

The inset of Fig.4.9 (b) presents a single period considered in the new strategy, with long axis L=200nm, short axis=80nm, and pitch P=205nm. In order to verify the effectiveness of this strategy, the bandgap calculation is carried out. The first three modes are displayed in Fig.4.9 (b). Initially, we

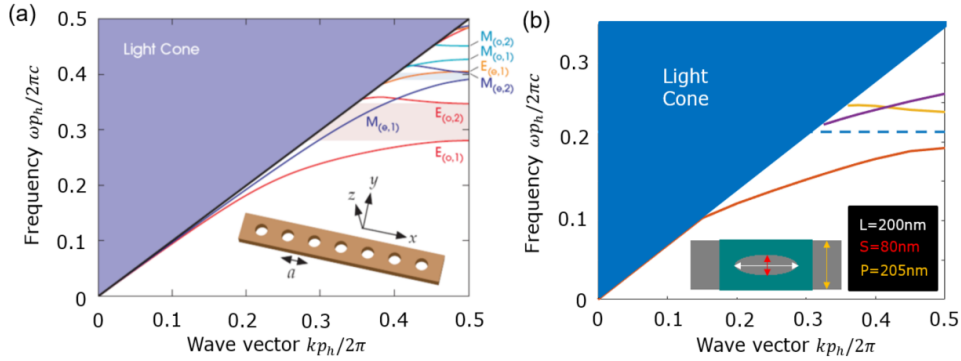

Figure 4.9. Band diagram of (a) a suspended 3D dielectric strip, picture taken from [149], (b) elliptical-hole-based waveguide, the inset shows a single period in the structure, with long axis L, short axis S, and periodicity P.

thought the purple curve polluted the bandgap. However, when comparing it to the band diagram of a suspended waveguide slab presented in Fig.4.9 (a) [149], we realize the purple curve in Fig.4.9 (b) is one of the guided modes: first order Transverse magnetic (TM) mode, and the orange and yellow curves correspond to the first and second order TE mode, respectively. All these modes are terminated at different wave vectors by the light cone (blue shade). Then we draw a blue dashed line representing the target wavelength 850nm and find it can safely travel through the bandgap. This preliminarily proves the effectiveness of our new strategy.

To further convince this point, we apply the elliptical hole shown in Fig.4.9 (b) inset to build a cavity around the QD, as depicted in Fig.4.10 (a). The design follows the procedure introduced in Chapter 4.1. Its field profile Fig.4.10 (b) indicates the cavity is working well at 850nm. Until now, we are fully convinced that replacing round holes with elliptical holes is an effective solution when the wide waveguide is the target platform for nanobeam cavity design.

The solution to the scale-up problem allows us freely make the on-chip SPS devices with the dimensions and working wavelength aligned with our expectations. Relied on the QD and wafer samples in our hand, we proposed a nanobeam cavity design in a $w = 400$nm, $h = 140$nm GaAs waveguide platform. The DBRs are constructed by the elliptical holes with the dimensional parameters: L=100nm, S=80nm, P=196nm. The QD is located in the center of a 1.16μm long cavity, expected to resonate at 915nm. The optimum source efficiency of this device is 80%, appearing in N_{bottom}=20 - N_{top}=3 structure.

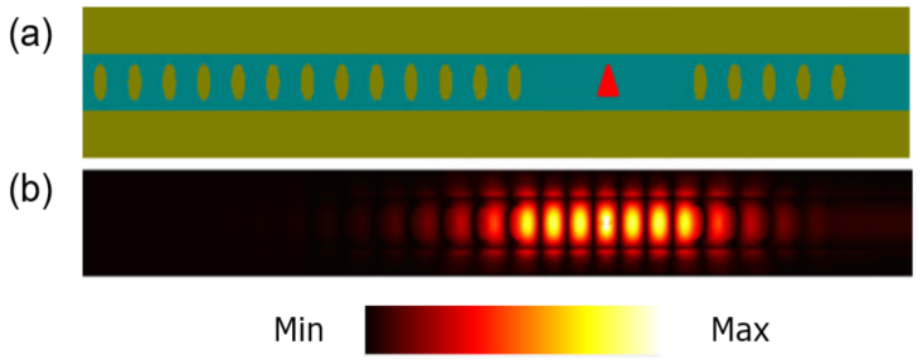

Figure 4.10. (a) Top view of the nanobeam cavity constructed by elliptical holes, QD is located in the center of the cavity and represented by the red triangle. (b) Field profile $|E|$ when QD emitted at 850nm.

Although it is not comparable to our champion design proposed in Chapter 4.1, it's more friendly to the fabrication perspective.

To further verify the existence of the cavity, we numerically calculate the transmission spectrum of the structure. As depicted in Fig.4.11 (a), the incident light comes from one side of the cavity, and the transmission is collected from the other side. We define the transmission rate as the ratio of Transmission/Incident. Fig.4.11 (b) shows the spectrum of N_{bottom}=2 - N_{top}=2 configuration. At our designed wavelength of 915nm, we observe a weak cavity performance which is implied by the broad FWHM on the spectrum, and the other two peaks roughly indicate the mirror stopband. A similar transmission spectrum of N_{bottom}=5 - N_{top}=5 configuration is displayed in Fig.4.11 (c). The same finding of a peak at 915nm further verifies the working wavelength in our nanobeam structure. This stronger cavity and stronger mirror correspondingly feature a narrower FWHM and a closer mirror stopband in Fig.4.11 (c), which is also in line with our expectations.

4.3 Wings study

For our ambition of achieving a near-unity on-chip source efficiency ϵ_{xy}, we made a lot of effort to design a good cavity in the semiconductor ridge waveguide platform. Looking back to the definition of ϵ_{xy} in Eq.4.2, we realize there might be another approach to improve this figure of merit, apart from utilizing the Purcell effect. The research in Chapter 4.1 mainly focused on the enhance-

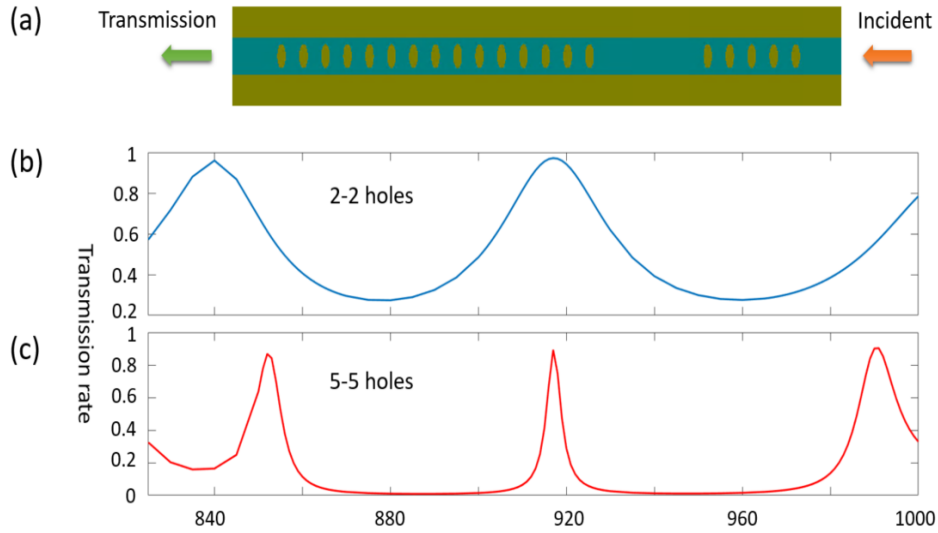

Figure 4.11. (a) The sketch of transmission simulation on nanobeam cavity. The incident light comes from one side of the cavity, indicated by the orange arrow, and the transmission is collected from the other side, depicted by the green arrow. (b) Transmission spectrum as a function of incident light wavelength under two configurations: (b) two holes and (c) fives holes in each side of the cavity.

ment of the x-polarized emission F_x and coupling ϵ_x by the implementation of the cavity along the y-axis. However, in this section, we will try to optimize the source efficiency by adding additional structures along the x-direction to inhibit the y-polarized dipole, ideally aiming at "zero" y-emission. If this can work, then the near-unity efficiency might be easier to realize with a simpler nanobeam cavity, meaning fewer challenges in fabrications.

4.3.1 Wings with bare waveguide

We choose an infinitely long bare waveguide depicted in Fig.4.12 (a) as the first platform, where a QD is located in the structure center. Inspired by the formation of the bullseye SPS, we surround the QD region with two semi-rings, as visualized in Fig.4.12 (b). The dimensions of the waveguide are in line with the values in Chapter 4.1, 220nm*140nm. We name this new configuration as wing-based waveguide.

To look for the optimal total source efficiency, we carry out the swiping on

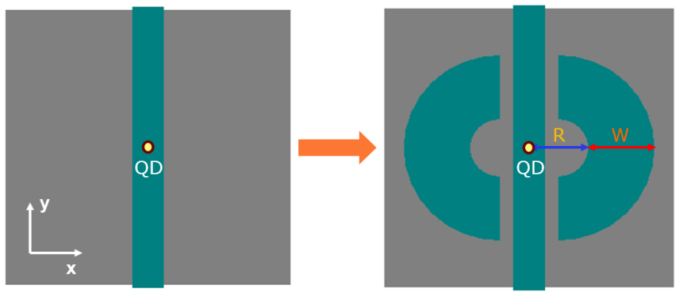

Figure 4.12. Top views of the QD (yellow dot) embedded in a bare waveguide and the same configuration surrounded by a pair of semi-rings. R is the distance from the QD location and the inner edge of the semi-ring, whose thickness is described by W. We call this structure a wing-based waveguide. The grey areas represent the SiO_2 substrates. The waveguides and the wings are both made of GaAs

two parameters, R and W, simultaneously. R is the distance from the QD to the inner edge of the ring, and W is the ring thickness. For a deeper insight into what is happening when R and W are changed, apart from the quantity of our interest ϵ_{xy} (Eq.4.2), we also display the corresponding 2D plots of x/y-polarized dipole emission $F_{x/y}$ (Eq.4.1), and the x-direction coupling efficiency ϵ_x (Eq.4.3) in Fig.4.13. The oscillations are observed in Fig.4.13 (a) and (b) when the ring thickness changes, while the impact on the y-polarized dipole is stronger than another polarization. This could be caused by a direct and significant phase shift in the y-polarized dipole due to the ring thickness change, and the phase of the x-polarized dipole might also be slightly affected by the four "feet" of the semi-rings, which are relatively closer to the waveguide section. As for the x-polarized coupling efficiency ϵ_x, only when the semi-rings are thick and close to the waveguide could this factor be influenced. If these additional structures can be far enough from the QD, then the x-polarized good properties are safe, which are indicated by the minor oscillations visualized in Fig.4.13 (a) and (c) when R is beyond 400nm. Now turning our attention to the figure of merit ϵ_{xy} displayed in Fig.4.13 (d). We can see the bright area is roughly coincident with the dark area in F_y plot Fig.4.13 (b), and vice versa. This proves that the inhibition of y-polarized emission can truly benefit the total source efficiency. The optimum efficiency is marked by the green star in Fig.4.13 (d), which points to W=100nm and R=300nm. In this configuration, the emission of y-polarized dipole F_y is suppressed to 0.22 from the original performance of 0.38 in the bare waveguide, and correspondingly, the efficiency ϵ_{xy} is enhanced from 68.5% to 73.1%, while the x-polarized properties F_x and

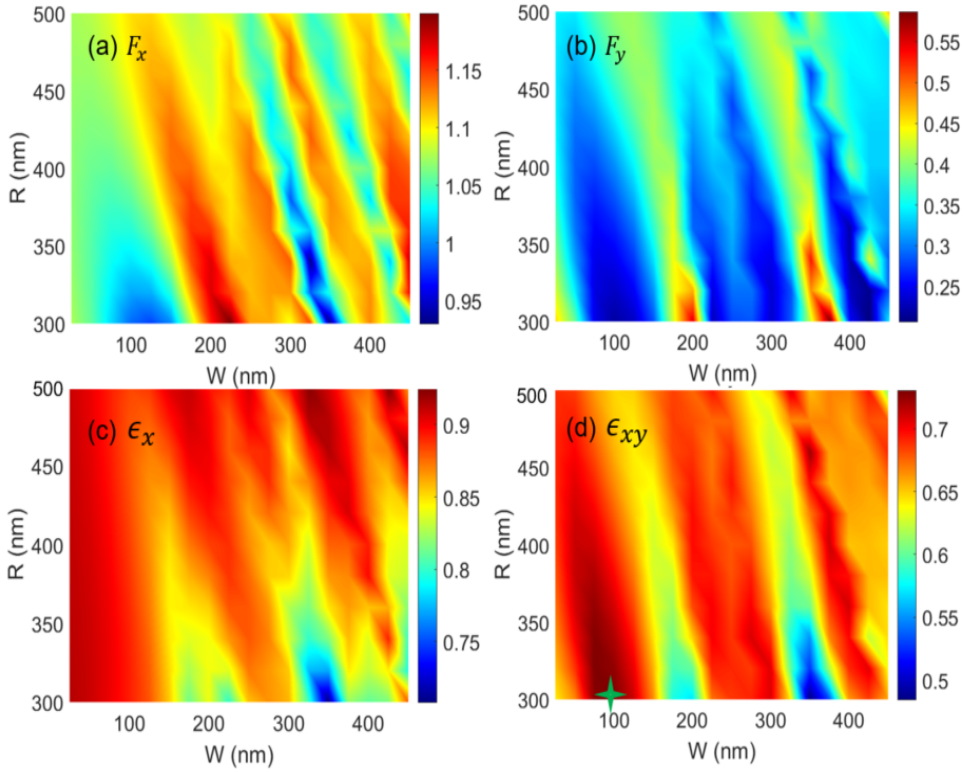

Figure 4.13. Purcell factor (a) F_x, (b) F_y and coupling efficiency (c) ϵ_x, (d) ϵ_{xy} as the functions of QD-wing distance R and wing thickness W. F_x and ϵ_x are evaluated for x-polarized dipole, F_y and ϵ_{xy} are simulated for y-polarized and xy-polarized dipole, respectively. The green star marks the maximum efficiency ϵ_{xy}, appearing at W=100nm, R=300nm.

ϵ_x are both slightly decreased. Although the improvement is not very remarkable, it still proves the idea of integrating additional structures perpendicular to the waveguide transmission direction is a potential approach to the highly efficient on-chip SPSs.

4.3.2 Wings with DBR mirror

Finishing the study of bare structure, we try to push forward by investigating the impacts of the wings on the same waveguide but with a DBR mirror, which consists of 5 round holes with a radius of 60nm. We take this single DBR-based waveguide as the reference structure, whose dipole emissions and coupling efficiencies are displayed in Table 4.2.

4 Configurations	F_x	F_y	ϵ_x	ϵ_{xy}
Reference	2.0	0.38	92.0%	77.5%
Reference + semi-rings	1.8	0.22	87.4%	78.0%
Reference + reversed semi-rings	2.0	0.34	91.5%	78.2%
Reference + reduced rings	2.0	0.30	91.4%	79.5%

Table 4.2. The dipole emissions and coupling efficiencies in different configurations. The reference structure is a 220nm wide, 140nm high GaAs waveguide only with a bottom DBR mirror, located on a glass substrate. The DBR consists of 5 unitary air holes.

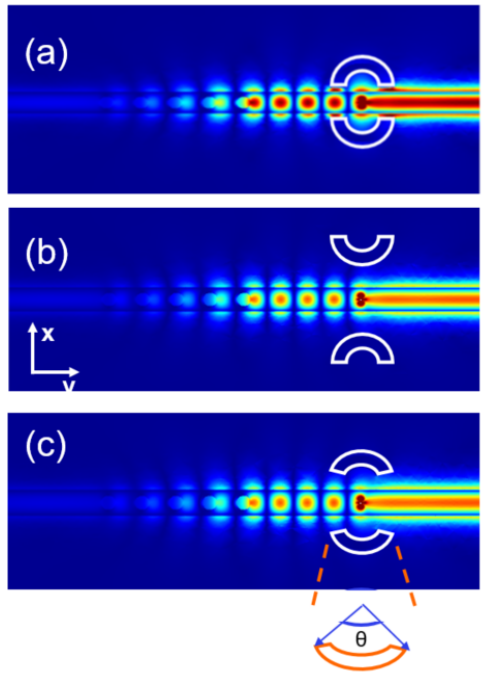

Figure 4.14. Field profile of waveguide with the same bottom mirror under (a) ring strategy, (b) reversed ring strategy, and (c) reduced ring strategy with an angle θ of 120°. The white lines outline the wings. The fields are not normalized by the same value, and thus the intensities are not fully comparable.

The first strategy is simply inheriting the optimum structural parameters (W=100nm, R=300nm) found in Chapter 4.3.1 and integrating the same pair of semi-rings to reference structure. A slight 0.5% enhancement of efficiency ϵ_{xy} is observed in Table 4.2. Although we see a good suppression of y-polarized emission, another polarization is also negatively affected. We attribute this

to the interaction between the rings "feet" and the waveguide sidewalls, as visualized in Fig.4.14 (a), where the "absorption" from the wings will increase the scattering loss, and therefore the x-polarized properties are damaged.

To avoid unwanted interactions, the second strategy is implementing the reversed semi-rings, as shown in Fig.4.14 (b). We can qualitatively see these additional wings almost have no influence on the field distribution. Agreed with our expectation, this strategy can maintain the original performance from the x-polarized perspective. However, its suppression of y polarization is poor. Thus, we flip the rings back and reduce the angle θ in the semi-rings to 120°, as depicted in Fig.4.14 (c), to minimize the obstruction of the wings to x-polarized performances. The third strategy presents better suppression of the y emission, and at the same time, F_x and ϵ_x are kept very well, which encourages us to further optimize this scheme.

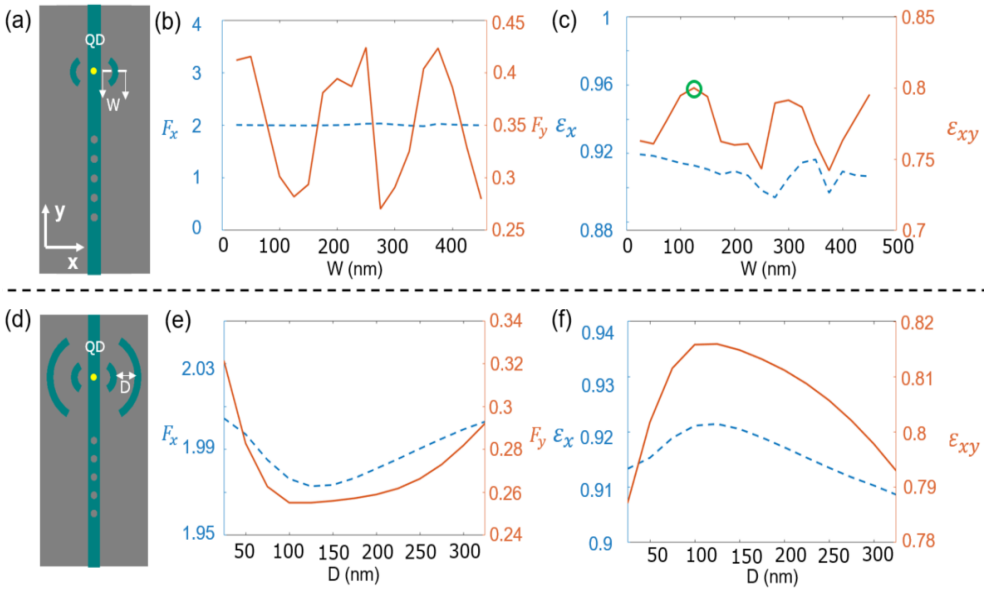

Figure 4.15. Sketch of the waveguide with a DBR mirror (5 air holes), surrounded by (a) one pair and (d) two pairs of reduced rings. (b) and (c) are the Purcell factors and efficiencies as a function of the ring thickness W of the structure depicted by (a). The green circle in (c) marks the optimum source efficiency ϵ_{xy}=80%, appearing at W=125nm. (e) and (f) display the same figures of merits as the function of trench width D between the two wings in configuration (d), where the rings' thicknesses are 125nm.

Here, we keep the ring angle at 120° and the distance R at 300nm, then study the responses of source performances to the change of ring thickness W.

As shown in Fig.4.15 (b), the emission of an x-polarized dipole F_x is almost not affected by W, while the other polarization F_y displays the oscillation with respect to the ring thickness, which is mainly caused by the phase change. Dominated by the strong vibration of F_y, similar behavior in the source efficiency ϵ_{xy} is also observed in Fig.4.15 (c). We extract the optimal ϵ_{xy}=80.0% from W=125nm. In the second step, we fix this ring thickness, and add another pair of reduced rings to the structure, as depicted by Fig.4.15 (d), which brings a new parameter: trench width D. In Fig.4.15 (e) we can see both F_x and F_y respond to the change of D, but not oscillating within the range that we are looking at. So far, unfortunately, we cannot explain the trends of these curves due to the lack of more physical insight into this problem. But we do make good suppression of y-polarized emission, which is reduced ∼30% compared to the reference structure. Thus, we see a peak value of ϵ_{xy}=81.5% at D=100nm in Fig.4.15 (f). The optimizations carried out in this chapter are not the end of this story, we believe the idea of inhibiting unwanted dipole emissions can give a better contribution to the highly-efficient on-chip SPSs by more careful designs and finer optimizations in the future.

4.4 Integration with SNSPD

The study in this section is in close collaboration with another Ph.D. student Marcel Erbe hosted by the University of Basel. Both as the members involved in the EU MSCA QUDOT-TECH project, we are not only interested in the generation of single photons, the following detection part also attracts our attention. Based on the structure he is going to fabricate, my task is to figure out the corresponding length of the detector, which is able to absorb 99.9% of the incident light.

The platform of our interest is sketched in Fig.4.16 (a). From the cross-section, we can see a GaAs waveguide is sandwiched between a substrate and two superconducting MoSi nanowires, whose refractive index at the device working wavelength 915nm is n= 4.8207 + 4.1552i. The material of the substrate can be $Al_{0.75}Ga_{0.25}As$ or air, the latter means a suspended waveguide. The heights of the waveguide and the MoSi nanowires are 180nm and 6nm, respectively. There's another 3nm thin Si covering on top of the Mosi material to protect the detector. Looking at the top view of the structure, we can find the overall shape of the superconducting detector, whose two feet (nanowires) are separated by a distance d. In the following, we will discuss the influence of d and nanowire width w′ on the length of 99.9%-absorption-detector.

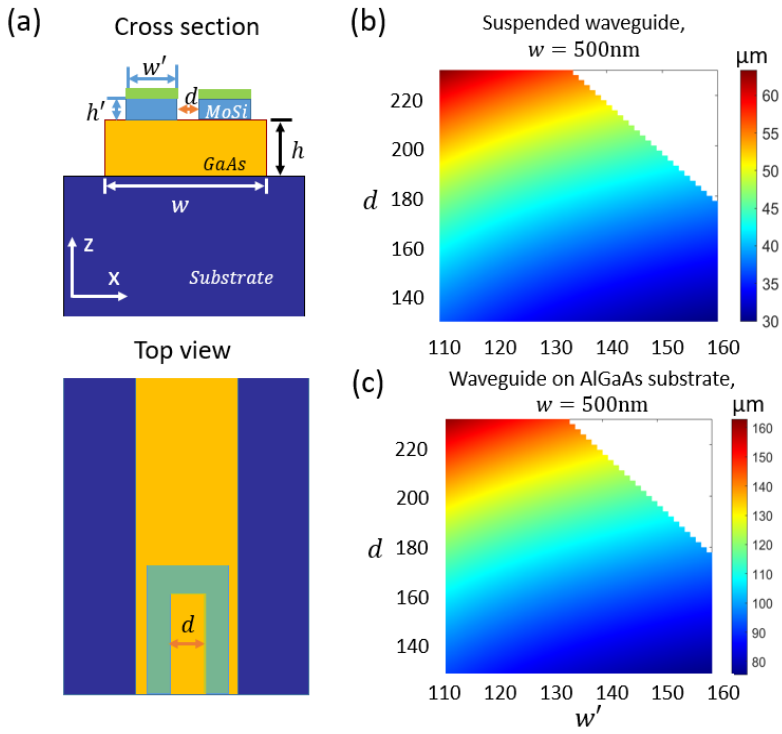

Figure 4.16. (a) Sketched cross-section and top view of the SNSPD integrated with a GaAs waveguide, on top of a substrate. A 3nm thin Si (green areas) covers the detector for protection. w and h are the dimensions of the waveguide, and w′ and h′ are the width and height of the MoSi superconducting nanowire, while d is the distance between the two wires. Detector length as the functions of w′ and d in 500nm wide (b) suspended waveguide and (c) the same waveguide on $Al_{0.75}Ga_{0.25}As$ substrate.

The first step in our calculations is to find the propagation mode and its effective refractive index n_{eff} at the cross-section displayed in Fig.4.16 (a). The propagation parameter β is obtained from the imaginary part of $2\pi n_{eff}/\lambda$. Following the function

$$\frac{P_L}{P_0} = exp^{-\beta L}, \tag{4.4}$$

where P_L and P_0 are the field intensities at the termination and the beginning of the MoSi detector, respectively. For the target of 99.9% absorption, the detector length can be directly calculated by Eq.4.5, where λ is the working

wavelength 915nm.

$$\frac{ln(0.001)}{-I(2\pi n_{eff}/\lambda)}, \tag{4.5}$$

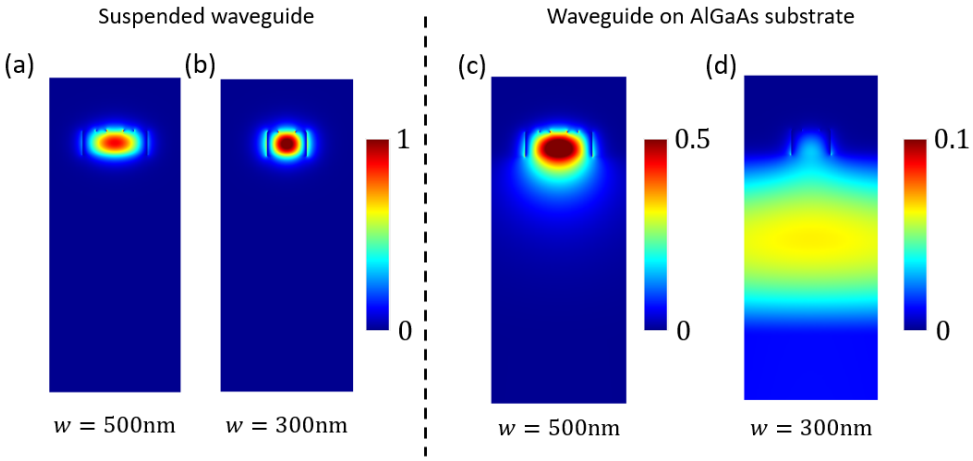

Figure 4.17. Propagation mode profiles of (a) 500nm, (b) 300nm wide suspended waveguide, and (c) 500nm, (d) 300nm wide waveguide based on AlGaAs substrate.

We first investigate a 500nm wide suspended waveguide. Fig.4.16 (b) illustrates the response of detector length to the change of nanowires' width w′ and their distance d. We can simply conclude that the required detector length is shortened with larger w′ and smaller d, which also indicates a larger overlapping between the detector and the waveguide top facet. We then transplant this structure to an AlGaAs substrate, which is also a candidate in experiments. We see a very similar performance in Fig.4.16 (c), and the only difference from (b) is the larger values in the color bar. This can be explained by the comparison of their propagation mode profiles, displayed in Fig.4.17 (a) and (c). Apparently, the suspended waveguide has better light confinement which can benefit the capture of light by the detector. In contrast, leaking into the substrate is inevitable in the AlGaAs configuration, which results in an overall longer detector than Fig.4.16 (b).

For further shortening the detector length, our interest is turned to a narrower waveguide, which generally provides better confinement to light. In Fig.4.18, we see the length is further reduced to ∼25 μm in a 300nm wide suspended waveguide configuration. The reduction mainly comes from stronger imprisonment in the waveguide, which is visualized from the comparisons of

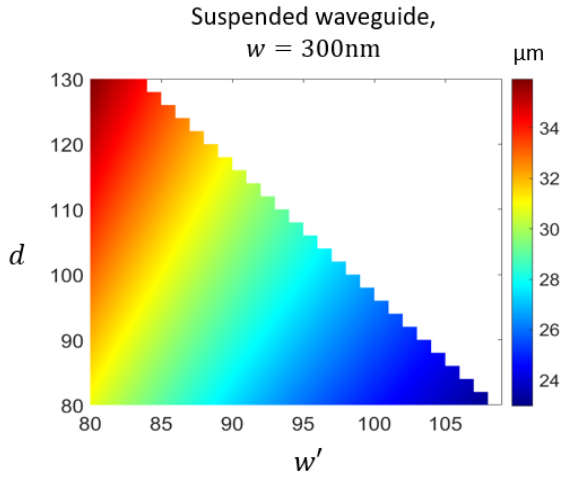

Figure 4.18. Detector length as the functions of w' and d in 300nm wide suspended waveguide.

the mode profiles in Fig.4.17 (a) and (b). However, we failed to find a shorter detector in the configuration of a 300nm wide waveguide on the AlGaAs substrate. The reason is shown in Fig.4.17 (d), where the light is squeezed to the substrate, due to the low index contrast between GaAs and AlGaAs. For the mode shown in Fig.4.17 (d), a 0.48mm long MoSi SNSPD is needed to capture 99.9% of the incident photons, thus we didn't carry out the parameters swiping for this last configuration.

4.5 Discussion and conclusion

In the first part of this chapter, we adopt the finite element method to numerically investigate the QD spontaneous emission and its coupling efficiency to the waveguide fundamental guided mode in a nanobeam cavity SPS. A careful cavity design can not only improve the dipole emission but also boost the source efficiency via lower scattering losses. By investigating the impact of the hole radius on the dipole emission properties, we find that the smaller the hole, the better it controls the scattering loss at the cavity-DBRs interfaces and in the taper. Our optimum platform appears with a near-unity efficiency (97.7%), a remarkable Purcell factor of 38.6, and a Q factor of 668. We also propose a taper to strongly reduce the number of holes in the bottom mirror by a factor of ~ 3, and to achieve a broader bandwidth, corresponding to a

slightly lower Q factor of 616. Moreover, the Purcell factor and efficiency are still comparable to those in the optimum system. If we overlook the challenge in fabrication, it is possible to pursue a source efficiency arbitrarily close to unity by reducing the radii in the overall structure and increasing the number of holes in the taper section based on our design. In addition, the platform under investigation is proven tolerant of imperfections on the hole variation and QD position deviation, especially for source efficiency.

Apart from building a cavity along the waveguide propagation direction, we also discussed another approach to suppressing the unwanted polarized emission for a higher source efficiency. By implementing the proposed structures along the direction perpendicular to the waveguide, our strategies showed good inhibition of unwanted polarization and in the end, improved the total source efficiency not only in the bare waveguide but also in the waveguide with a single DBR mirror. Although the enhancements were not very significant, our idea still displayed the good potential of contributing to a highly-efficient on-chip SPS. Since the current strategies and structures are not fully optimized, there is still plenty of space for improvement. More effort in the future should be allocated to the design and optimization of this idea for an ambitious target of zero emissions from unwanted polarization. If this can come true, then our need for an excellent cavity could be highly released, and thus the near-unity efficiency might be realized in a truly fabrication-friendly structure.

In the last part of Chapter 4, we considered the integration of MoSi SNSPD to the top facet of the GaAs waveguide. We discussed the length of the detector, which is able to capture 99.9% of the incident light, in different configurations. In our simulations, we first computed the propagation mode of the structure cross-section and extracted the effective refractive index, according to which, we were able to calculate the detector length, responsible for the 99.9% light absorption. The narrow suspended waveguide showed the best light confinement, and thus the length requirement for the detector was the shortest, which was $\sim$25 μm. Considering the refractive index contrasts in GaAs/Air and GaAs/AlGaAs, the leakage of light from the waveguide to the AlGaAs substrate was more severe than the suspended configuration. Thus, it's harder for the detector to capture light from the waveguide on an AlGaAs slab than from the suspended waveguide with the same dimensions, which leads to a longer required length for the detector. Moreover, due to the small index contrast in GaAs/AlGaAs, the light in a narrow waveguide would be squeezed into the substrate, resulting in a very long detector of 0.48mm. This work is in close collaboration with Ph.D. student Marcel Erbe from the Uni-

versity of Basel, and he is carrying out the fabrications and the experimental tests based on the numerical simulations presented in this chapter.

CHAPTER 5

Impacts of electrical contact implementation on sources performances

As illustrated in Chapter 1.4, the implementations of electrical contacts to QD-based SPSs have tremendous contributions to stabilize QD's state by Coulomb blockade [82] and drastically reduce charge noise [85, 86], which is beneficial to the indistinguishability of the emitted photons. In addition, for a more efficient QD-cavity resonance, the spectral alignment between QD and the cavity is of vital importance [25, 132]. Again, this is able to be realized by tuning the QD emission via QCSE with electrical contacts. The reason is that QCSE allows for finely tuning the optical transition frequency of the QD, by affecting the Coulomb and exchange interactions among the charge carriers [102–104]. On the other hand, as the heart of quantum information processing [19,154] and some of the quantum protocols [155,156], the challenge of realizing remote quantum interference has to be overcome. Here, a basic requirement for remote quantum emitters is the same working frequency. Otherwise, the quantum operation might be failed. Applying the electrical contacts is a promising strategy for making good spectral alignment between the emission lines from individual sources [39]. Based on the above three benefits, an electrically tunable SPS is a very strong candidate in the field of quantum applications. Although in the last few years, there have been many theoretical studies regarding the optimization of devices' geometries of different types [58,157–159], few of them include the consideration of electrical contacts [160–162].

Motivated by the importance of electrical contact and the lack of its numerical simulations, in this chapter, we dedicate our insights to the readers regarding the impacts of additional sections for implementing the contacts in nano-cavities on the overall SPS performances. This chapter is based on our perspective manuscript [87], which is attached as the Appendix C.

5.1 Strategies in vertical-emission SPSs

In this section, we introduce different types of contact strategies to three vertical-emission SPSs, including Micropillar, nanopost, and bullseye structures, and present the individual impacts of these strategies from the numerical point of view. In Chapter 5.1, we evaluate the source performance from two aspects: Purcell factor Fp and the source efficiency ϵ.

5.1.1 Micropillar structure

The studies are launched from one of the most successful SPS devices so far: Micropillar, which features an excellent Purcell factor and photon collection efficiency. The layout implemented for the following investigations, as visualized in the central section of Fig.5.1 (a), consists of a GaAs cavity sandwiched by a 40 pairs bottom DBR and a 17 pairs bottom DBR. The thickness of the cavity layer is 256.1 nm, and those in DRBs are 74.8 nm ($Al_{0.85}Ga_{0.15}As$) and 64.0 nm (GaAs), respectively.

5.1.1.1 Strategy I: Gold Ring

Gold ring scheme is the first strategy implemented for the above-mentioned Micropillar device, which is fully sketched in Fig.5.1 (a). The pillar diameter is fixed at 2.2 μm, and the difference between the ring's inner and outer diameter is 6 μm. We tune the overlap d by changing the inner diameter and then investigate the impact of the gold ring on the source performances.

Fig.5.1 (e) illustrates the response of the Purcell enhancement Fp and the source efficiency ϵ to the change of ring-pillar overlap. Our study reveals that they are sensitive to implementing an additional gold ring, especially when the overlap is more than 200 nm, from where we can see a cliff-like drop in performance. Firstly, the absorbent property of the gold material can reduce the number of collected photons, and the more the ring overlaps, the more significant the reduction. Secondly, the complicated scattering and the corresponding interference introduced by the gold ring can strikingly affect

the far-field emission patterns of the structure, as shown from Fig.5.1 (b) to (d).

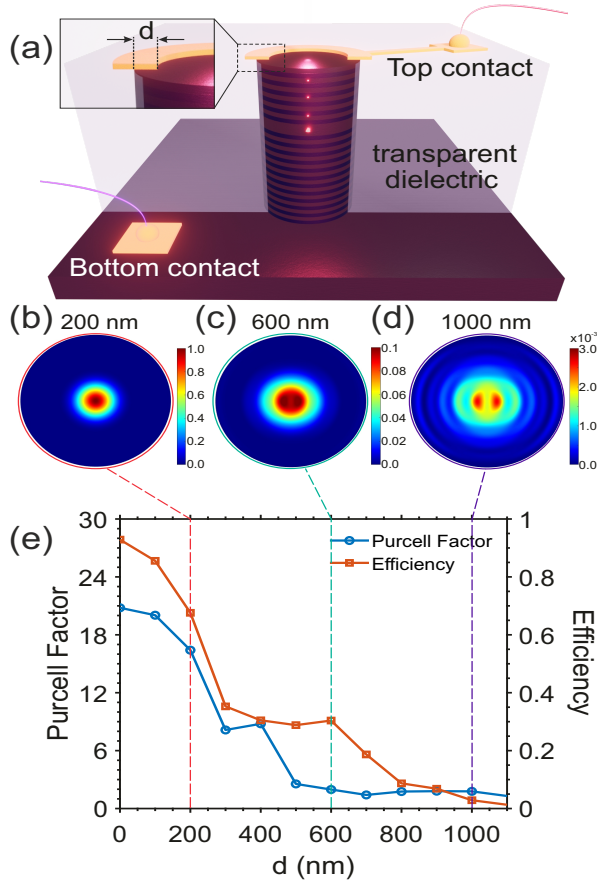

Figure 5.1. (a) Sketch of the Micropillar SPS surrounded by the transparent dielectric material Benzocyclobutene (BCB) and covered by a gold ring on top. The pillar consists of two GaAs/$Al_{0.85}Ga_{0.15}$As DBR mirrors and a GaAs cavity between them, with the QD at the center of the cavity. The inset shows the overlap distance of d between the central pillar and the gold ring. The material BCB (refractive index n=1.54) around the micropillar is mechanically used to support the gold ring. Normalized far-field emission patterns when the overlap d is (b) 200, (c) 600, and (d) 1000 nm, respectively. (e) Purcell enhancement Fp and source efficiency ϵ as a function of ring-pillar overlap d. The figure is taken from [87].

We can see the far field is increasingly more split towards the outer area, which directly reduces the proportion of photons within the NA of the lens and correspondingly destroys the source efficiency. Nevertheless, making the overlap around 200 nm is feasible in fabrication and still can maintain a Purcell

enhancement of 15 and an efficiency of 60%.

5.1.1.2 Strategy II: ITO slab

As depicted by Fig.5.2 (a), the second strategy is to cover the top of the Micropillar device by attaching an Indium tin oxide (ITO) slab, which is a type of transparent and conductive material. The central pillar is surrounded by BCB, being used to support the ITO mechanically. Fig.5.2 (b) and (c) indicate the impact of the ITO slab on the Purcell factor and the source efficiency, respectively. To figure out the influence of the lossy property of the ITO material, we consider both the lossy and non-lossy conditions; the latter is carried out by simply erasing the imaginary part in the refractive index. We can see the wave-like behavior from Fp and ϵ, resulting from the additional phase shift introduced by the ITO layer. For non-lossy conditions, we can expect a comparable performance to the device without an ITO slab by carefully choosing the slab thickness. In this case, ITO doesn't give us other effects than phase change.

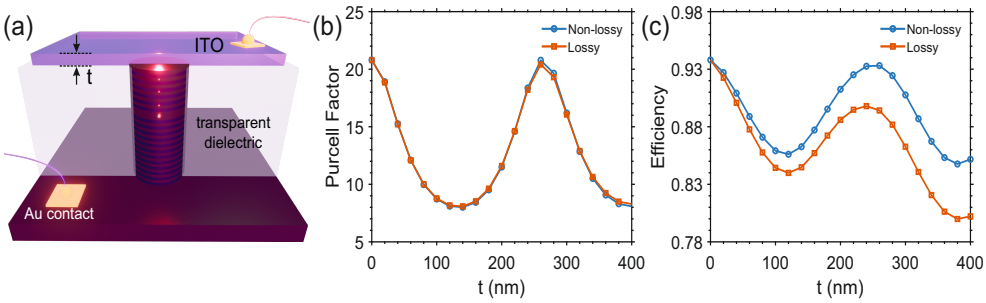

Figure 5.2. (a) Sketch of the Micropillar structure surrounded by BCB material and covered by an ITO slab, whose thickness is represented by t. (b) Purcell factor Fp, and (c) source efficiency ϵ, as a function of t, when considering/ ignoring the lossy property of ITO with a corresponding refractive index n_{ITO}=1.712+0.01i/n_{ITO}=1.712. The figure is taken from [87].

Conversely, considering the lossy configuration, except for the wave-like behavior explained above, we can see a continuous decrease in source efficiency. This is mainly due to the absorption of photons emitted upwards from the micropillar by the lossy ITO slab. In contrast, Fig.5.2 (b) reveals Fp is more robust in the lossy condition thanks to the long distance from the ITO slab to the QD position. Even considering the intrinsic loss of the material, the peaks in Fig.5.2 (c) tell a slight reduction of source efficiency from 94% to 90% when

thickness t is around 250 nm, which indicates this strategy has good potential to keep the SPS performance.

5.1.1.3 Strategy III: bridges

Another solution for contacted pillar was presented in 2016 by Somaschi *et al.* [163]. In this case, the vertical body is connected to a surrounding circular frame by four 1.5-μm-wide wires, which allows locating the top p-contact. The devices realized featured a disruptive purity and indistinguishably under resonant excitation of 0.0028±0.0012 and 0.9956±0.0045, respectively.

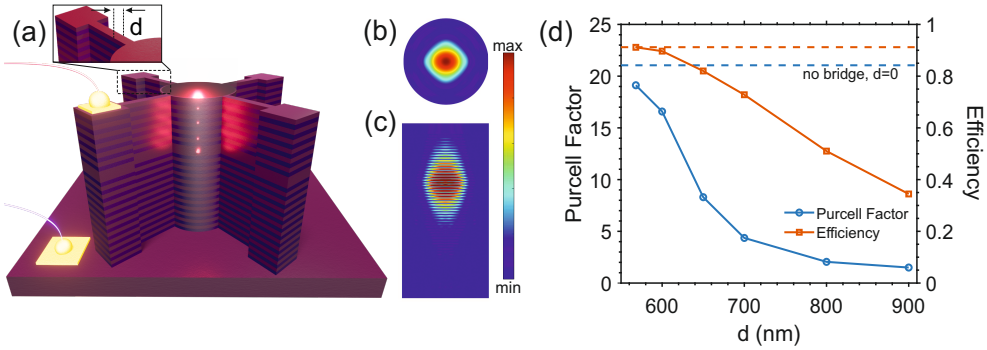

Figure 5.3. (a) Sketch of the Micropillar with four surrounding bridges, whose lengths are 1 μm and widths are w. (b) Normalized far-field emission pattern and (c) vertical field propagation throughout the device when the bridge width is half of the Micropillar radius. (d) Purcell factor Fp and source efficiency ϵ as a function of bridge width. The dashed lines indicate the original Purcell factor (blue) and source efficiency (orange) of the Micropillar device without the bridges. The figure is taken from [87].

Inspired by this idea, we introduce the third strategy under investigation: building bridges around the central Micropillar and placing the electric contacts on top of the bridges' terminals. We fix the bridge length at 1 μm and change the bridge width to study the impact of the bridges on the SPS performance. As depicted in Fig.5.3 (a), we initially implement a four-bridge scheme. Fig.5.3 (b) and (c) are the far-field emission pattern and the vertical field propagation when the bridge width is half of the Micropillar radius. Under this configuration, both two field profiles are slightly modified by the four bridges. To quantitatively analyze, we investigate the impact of bridge width on the Purcell factor and source efficiency. Fig.5.3 (d) indicates that broadening the bridge width to over 600 nm for this configuration can significantly destroy the SPS properties, and both Fp and ϵ sharply drop. This is due to the bridges' damage to the cavity mode and the corresponding leakage

of photons into them. Nevertheless, a bridge width of 550 nm is promising to maintain the identical source performance and is still feasible in fabrication. One can consider another two-bridge configuration, which can naturally break the degeneration of two orthogonal polarized modes. This strategy leads to a total source efficiency of 50% by considering both dipole orientations. The encouraging point is that it shows the potential to break the bottleneck of 50% filtered efficiency under the resonant excitation scheme in a rotationally symmetric Micropillar device.

5.1.2 Nanopost structure

As demonstrated in Chapter 3.1, nanopost is a simple SPS design, but it features a remarkable Purcell enhancement and a good source efficiency [164]. Such structure can be seen as the truncated and, to some extent, simplified version of the tapered and inverted tapered nanowire [160]. Similarly to the bullseye, its main advantage compared to the high-Q cavities is that it is a broadband device and the large operating bandwidth relaxes the spectral matching requirements [136, 165, 166]. In particular, the nanopost funnels the QD SE into the fundamental cavity mode. Moreover, further proof of concept shows that a Purcell factor as high as 7.9 and a collection efficiency of 0.69 can be reached and similar values can be maintained over a broad spectral range [167]. In this section, we investigate the electrical tuning strategies of this simple but effective device.

The original nanopost consists of a truncated GaAs nanowire on top of a gold mirror and a 13 nm thick SiO_2 slab, as depicted in Fig.3.1. This structure is designed for an InAs QD, which can emit photons at around 930 nm. In numerical simulations, we consider the semiconductor QD an in-plane point dipole under the dipole approximation. The diameter of the truncated nanowire is 250 nm, and the height is 461 nm. We locate the on-axis dipole to the second antinode inside the cavity, which is 268.7 nm from the bottom of the post. The figures of merit considered in this work are the Purcell enhancement $Fp = P_{total}/P_{bulk}$, and the source efficiency $\varepsilon = P_{collected}/P_{total}$, where P_{total} is the power emitted by the dipole, P_{bulk} is the dipole emission in bulk material, and $P_{collected}$ is the power collected by the first lens. We perform the FEM simulations for this nanopost structure under the first lens NA of 0.75.

5.1.2.1 Impact of ITO thickness

The first electrical tuning strategy is to attach a slab of ITO on top of the nanopost. We can fabricate several pillars to support this slab mechanically. However, these pillars are not considered in numerical simulations since they are relatively far from the central structure. Hence, we call it the suspended contact configuration.

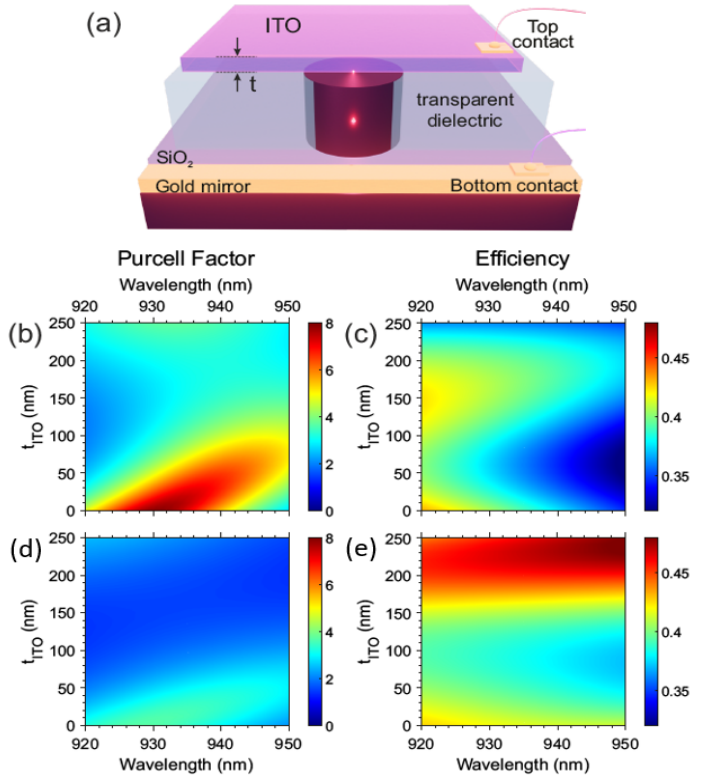

Figure 5.4. (a) Schematic of the electrically tuned nanopost structure with an ITO slab mechanically supported by the BCB material surrounding the truncated nanowire. (b)/(d) Purcell enhancement Fp and (c)/ (e) source efficiency ϵ as the functions of wavelength λ and the thickness of ITO slab t_{ITO} in suspended configuration/ BCB supporting configuration. The figure is taken from [87].

Fig.5.4 (b) and (c) demonstrate the impact of ITO thickness t_{ITO} on the SPS performances, Fp, and ϵ. The pure nanopost structure gives a Purcell enhancement of 7.9 and an efficiency of 40% at 930 nm. By increasing the thickness of ITO, the cavity resonance firstly redshifts and then blueshifts

back, which results from the overall phase change introduced by the ITO slab. On the other hand, the on-resonance peak Fp gradually decreases in this process, which is the consequence of the absorption of ITO. Similarly, the source efficiency also experiences spectral shifting and an overall decrease caused by the same reasons mentioned above. However, the reduction on ϵ is relatively smaller than that on Fp, suggesting the efficiency is more robust than the Purcell enhancement in the ITO-Nanopost structure.

Considering the better mechanical stability, we proposed another configuration where the ITO slab is propped up by the BCB material surrounding the nanowire, as depicted in Fig.5.4 (a). We also investigate the impact of t_{ITO} on the source performances for this configuration, as shown in Fig.5.4 (d) and (e). We can see the behavior in the response of Fp is similar to that in the suspended contact strategy. The worse performance is mainly due to the weaker confinement on the emission when the refractive indexes of the nanowire and the surroundings become closer. Here, we adjust the structural parameters to ensure the nanopost-BCB design has a decent source performance, primarily targeting a reasonable collection efficiency. As shown in Fig.5.4 (e), it is surprising to see an enhancement in efficiency by implementing a thick ITO slab. However, Fig.5.4 (d) tells that the ITO slab should be as thin as possible to maintain the Purcell factor. Hence, there is a trade-off between choosing Fp or source efficiency as the figure of merit of the work, which will affect the thickness choice for the ITO slab.

5.1.2.2 Impact of bridge orientation and width

Another strategy is to add a single bridge directly connected to the nanopost. In the experiment, we can attach the metal contact to the end of the bridge and then control the electrical tuning, as depicted in Fig. 5.5 (a). This single bridge breaks the rotational symmetry of the original nanopost structure, which means the dipole orientation may significantly affect the overall source performances. The bridge discussed in this section is fixed as 1 μm long. We assume the bridge extends along the x-axis and then investigate the device's properties when considering the dipole orientation along the x-axis and the y-axis, respectively.

The comparison of the field distributions in Fig. 5.5 (b) strongly indicates that one can effectively suppress the cavity mode penetrating to the bridge by applying the dipole polarized perpendicular to the bridge orientation. On the other hand, the inset of Fig. 5.5 (d) suggests that the y-polarized dipole has more advantage in ensuring the far-field emission concentrated within the NA

of the first lens. In contrast, the splitting far-field pattern of the x-polarized dipole in Fig. 5.5 (c) might point to the complicated interference introduced by the scattering from the bridge terminal. Overall, the y-polarized dipole qualitatively shows better potential to maintain the SPS performances when the bridge is etched along the x direction.

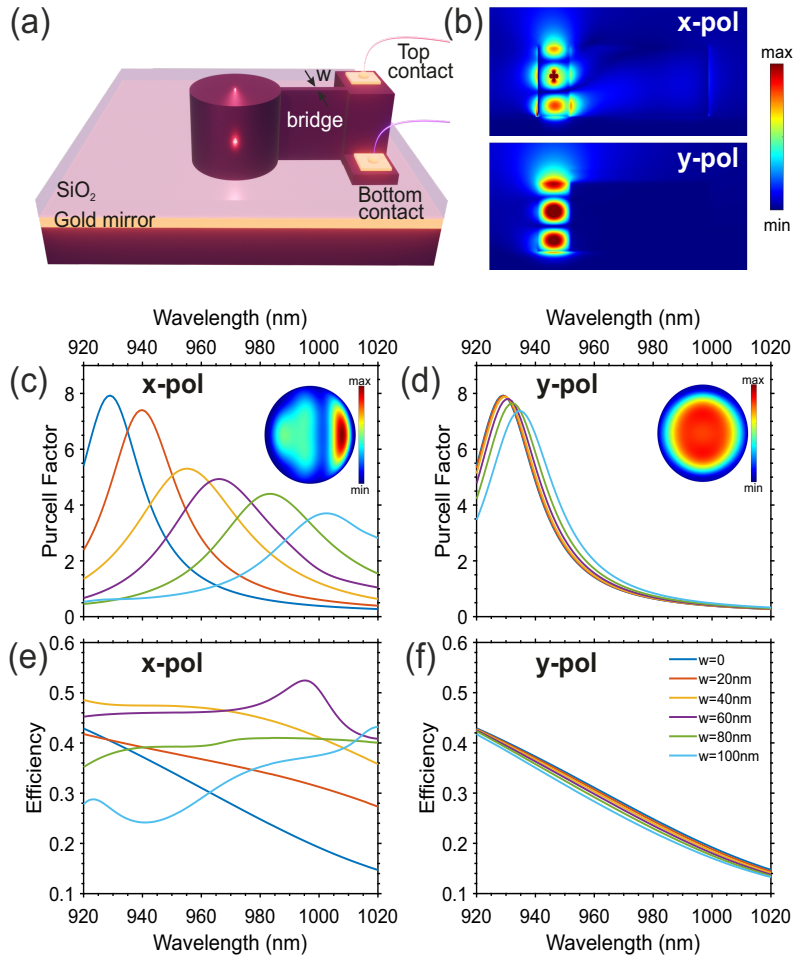

Figure 5.5. (a) Sketch of the nanopost-bridge strategy. (b) Vertical field propagation in the structure with x/y-polarized dipole. (c)/(d) Purcell enhancement Fp, with insets showing the far-field emission pattern when the dipole polarization is along/perpendicular to the bridge orientation, and (e)/(f) source efficiency ϵ as a function of wavelength λ for x/y-polarized dipole when the bridge width varies between 0 nm 100 nm. Here, we assume the bridge extends along the x-axis. The figure is taken from [87].

To provide a quantitative analysis, we tune the bridge width from 0 to 100 nm and study the corresponding spectral response of Fp and ϵ. As shown in Fig.5.5 (c) and (d), two polarization configurations both redshift with increasing bridge width w. However, as indicated by the qualitative results, the y-polarized dipole is less affected by the x-oriented bridge, which manifests in three aspects. Firstly, the resonance spectral shift range (10 nm) in Fig.5.5 (d) is ten times narrower than that (100 nm) in Fig.5.5 (c). Secondly, the reduction of the on-resonance Purcell enhancement for a y-polarized dipole is only 12.5%. In contrast, this value is 50% for an x-polarized dipole. Lastly, Fig.5.5 (e) reveals that the impact of the bridge on the source efficiency for the x-polarized dipole behaves disorganized. However, in Fig.5.5 (f), this impact on the y-polarized configuration is more regular and traceable. Considering the bridge width of 100 nm, comparable to the nanopost radius, we can still observe a Purcell enhancement of 7 and a source efficiency of only 5% less than the bridgeless construction. With this quantitative analysis, we are convinced that the single bridge strategy is promising to maintain good SPS properties when the dipole and bridge have orthogonal orientations.

5.1.3 Electrical tuning in regular CBG and hole-CBG devices

Bullseye (or CBG) structure is an outstanding SPS design that features a good Purcell factor, a remarkable source efficiency, and a broad bandwidth, which is friendly to the QD alignment. Successful electrical tuning ofCBGs has been only recently realized. Among all, the work by Schall *et al.* describes the development of electrically controllable Quantum-Dot-Molecule devices with excellent optical and quantum optical emission properties. They are based on stacked QDs in a pin-diode structure that is subsequently deterministically integrated using in situ electron beam lithography [168]. At the same time, a team from the University of Cambridge was working on a novel design that would be compatible with carrier injection. This considers leaving four semiconductor bridges that connect the central disk, containing the QD, to some n- and p-type contacts. The reported theoretical Purcell factor and dipole collection efficiency are 20 and 70%, respectively. It is also shown that the presence of such bridges affects the confinement of the mode in the cavity. Consequently, the Fp and the efficiency result more or less deteriorated depending on the bridges' width [162].

Considering these results, we dedicate this subsection to proposing the bridge-bullseye structure as the electric tuning strategy and investigating the impact of the bridges on the device. As shown in Fig.5.6 (a), we implement

four bridges to a simple regular bullseye design consisting of a central disk and four outer rings on top of the substrate. The disk and rings are made of GaAs. The substrate comprises a SiO_2 slab, a gold mirror, and a Si layer. In addition, the InAs QD with a dipole orientation along the bridge direction is located in the center of the central disk. The structure in our work has the following parameters: the radius of the main disk R = 360 nm, the periodicity of the rings P = 360 nm, the trench W is 108 nm, the thickness of GaAs, SiO_2, and the Gold layers are 170 nm, 250 nm, and 100 nm respectively. The Purcell factor and source efficiency of this regular bullseye structure without the bridges are 20 and 88.7% when NA of the first lens is chosen as 0.82.

We can see the impact of the bridges' width on the cavity resonance, the Purcell enhancement, and the source efficiency from Fig.5.6 (d), where we fix the bridge length at 3.5 μm. With the increase of bridge width, the cavity resonance starts to red-shift. Moreover, the on-resonance Purcell factor increases first and then decreases, leaving an optimum Fp of 25 when the bridges are 150 nm wide. The rise in the left part benefits from the additional pattern in the angular direction, compared to the single radial pattern in the classical bullseye structure. Although the physical reason is not clear yet, Ref. [64] has proved the remarkable enhancement of the Purcell factor resulting from the angular pattern in the bullseye. However, as the bridges are widened, the cavity mode is damaged, which leads to increased photons penetrating the bridges. Hence, we see a decrease in the right part of Fig.5.6 (d).

Another figure of merit is the on-resonance source efficiency ϵ, which is negatively affected by the widening of the bridges, as indicated by the dashed curve. ϵ is almost halved when the bridge width is 300 nm compared to the bare bullseye. The reduction in efficiency firstly results from the photon in-plane leakage. On the other hand, the bridges can also modify the far-field emission pattern of the whole device. The modification can be observed from the comparison between Fig.5.6 (b) and (c). (b) corresponds to the bare bullseye, and (c) is obtained from the bridge-bullseye structure when the bridge width is 60 nm. We can see the implementation of the bridges causes the light to diverge in the far field beyond the NA range, which is a negative factor to the source efficiency. However, Buchinger et al. [169] proposed other strategies, including changing the number of bridges and even rotating the bridges, which are both possible to achieve higher efficiency than the four-straight-bridge scheme discussed in this work. Nevertheless, it is still promising to maintain a good SPS performance in our configuration by controlling the bridge width below 150 nm, which is a possible value for fabrication. These

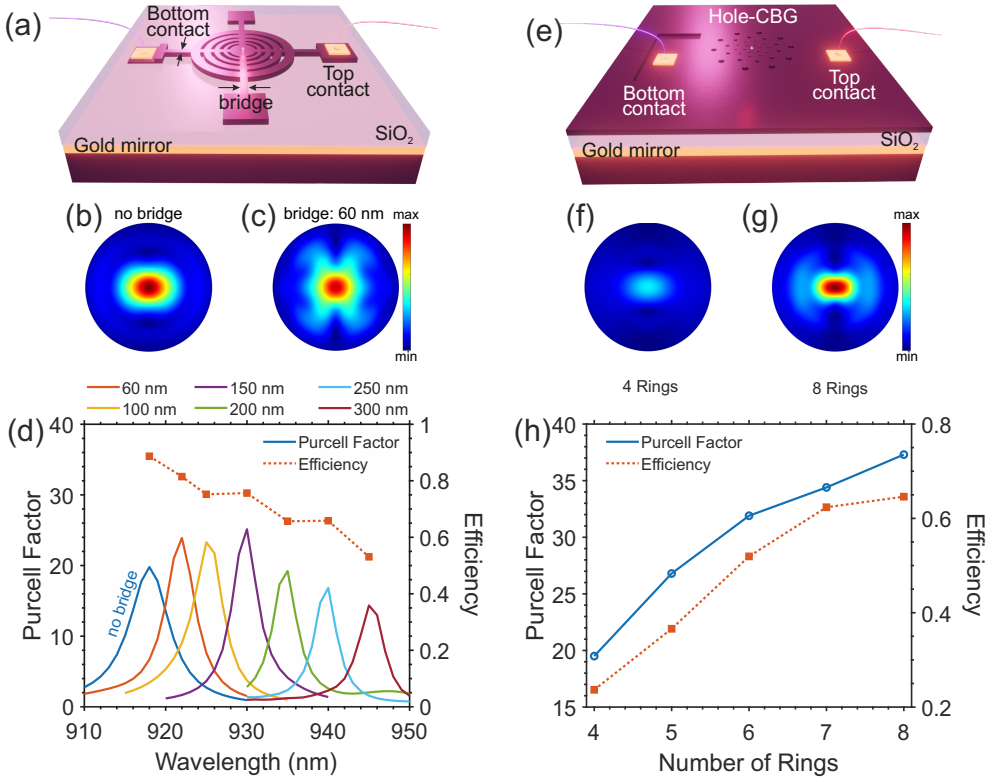

Figure 5.6. (a) Sketch of the bridge-bullseye structure, with a QD embedded in the center of the central disk. Normalized far-field emission patterns (b) without/ (c) with 60 nm wide bridges. (d) Purcell factor as a function of wavelength when the bridge width varies in the range of 0-300 nm, where 0 nm refers to no bridge. The points on the dashed curve are the corresponding efficiencies when the dipole is resonant with the cavity mode. (e) Sketch of the hole-bullseye design with 3 rings. Far-field emission patterns of (f) 4-ring, and (g) 8-ring structure, normalized by the same field intensity. (h) On-resonance Purcell factor (blue) and source efficiency (orange) as a function of ring numbers in hole-CBG device without the boundary. The figure is taken from [87].

results also indicate the possibility of choosing the resonance wavelength in a relatively large range by simply changing the bridge width instead of making a new bullseye design. We also observe similar behaviors when the dipole polarization is 45-degree to the bridge.

In addition to the traditional ring-based structure, we also consider another new-type hole-bullseye SPS, as visualized in Fig.5.6 (e). The overall idea is to construct the gratings with air holes instead of rings. Ref. [134] is the first work that demonstrated an impressive enhancement in Purcell factor and Q

factor with this structure compared to the performances of the regular CBG, and thus we investigated the optimization for this structure in Chapter 3.2. However, we find this new design might also contribute to a simpler way to interact with the QD, without integrating the bridges. From the numerical perspective, the efficiency of the structure with a fixed boundary can go up to ∼80%, which is appreciated in our consideration. However, the relatively narrow boundary prevents a direct implementation of the electrical contacts due to the lack of space. Therefore, we remove the boundary of the structure in this work, meaning that all the layers are freely extensive in the horizontal direction, which provides plenty of space for the contacts. After rough optimization, we determined the structure under research has the following parameters: central disk radius R = 208.2 nm, radial pitch P = 332.6 nm, hole diameter D = 95 nm, and angular periodicity A = 160 nm. Fig.5.6 (h) demonstrates the impact of the number of air-hole rings on the Purcell enhancement and the first-lens collection efficiency within NA=0.82. By increasing the ring number, we can observe both figures of merits are linearly enhanced. The far-field profiles of 4-ring and 8-ring structures displayed in Fig.5.6 (f) and (g) reveal that the increase of ring number only affects the field intensity without the modification of the shape. This can imply linear enhancement to some extent. Based on our simulations, we predict the performances would become saturated at some point, instead of a non-stop growth. Considering the decent source performance of Fp=37.3 and efficiency=64.6%, and the ease of contacts integration, we believe the hole-bullseye device is a more promising candidate than the traditional ring-CBG structure concerning a good tunable SPS.

5.2 Contact strategy in on-chip nanobeam SPS

In this Section, we talk about the electric tuning scheme applied to the GaAs nanobeam cavity sketched in Fig.5.7 (a), which has the same structural parameters as the configuration discussed in Chapter 4.1. This champion nanobeam cavity features a remarkable Purcell factor of 38 and an outstanding near-unity source efficiency when the QD is at the center of the cavity. The two bridges are used to locate the electric contacts. Firstly, we place the 800 nm-long bridges precisely in line with the dipole position. However, Fig.5.7 (b) indicates the light penetration into the bridges, which will destroy the source performance. A possible solution is to move the bridges away from the cavity and put them in the weakest field to avoid the bridge's impact to the greatest

extent. Then, we locate the bridges at the third node relative to the cavity center, one up and one down. The corresponding field profile in Fig.5.7 (c) qualitatively indicates the feasibility of this solution, where we can see much less light going to the wings than in Fig.5.7 (b).

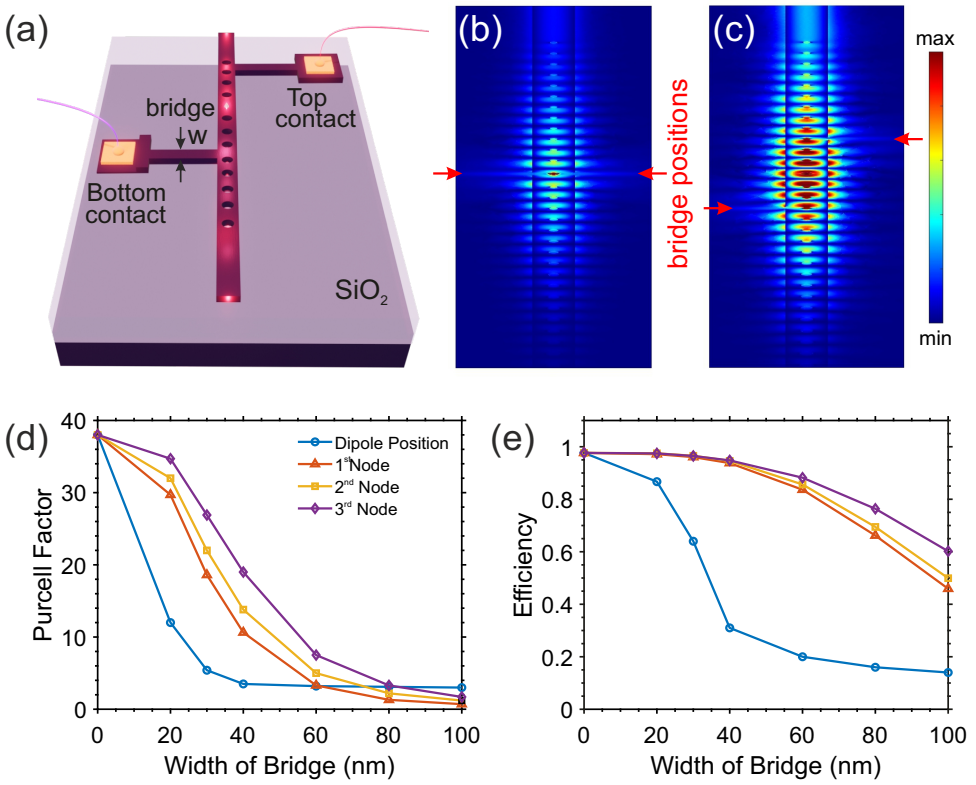

Figure 5.7. (a) Sketch of the nanobeam cavity sandwiched by two DBR mirrors. The normalized electric field profile when the bridges are (b) at the dipole position / (c) at the third antinodes (one upward and one downward). (d) Purcell Factor and (e) source efficiency ϵ as a function of the bridge width for different bridge locations. The figure is taken from [87].

Again, from the quantitative perspective, we analyze the impact of the bridge width on the Purcell factor and the source efficiency when putting the bridges at different locations. Here, the Purcell factor is evaluated for the x-polarized dipole, and the source efficiency ϵ, which is defined as the proportion of the light funneled into the fundamental waveguide mode, is assessed for the xy-polarized dipole. Fig.5.7 (d) and (e) illustrate the impact of different bridge positions on the SPS properties. We can see Purcell factor and ϵ are

sensitive to the bridges when they are spatially in line with the dipole position, especially for the Purcell enhancement. Even if the bridge width is only 20 nm, the Purcell factor dramatically drops from 38 to 12, which means only 30% of the performance is maintained. In contrast, if we put the bridges in line with the nodes, where the electric field is weakest, we can see a good keeping of efficiency. For the bridge width of 60 nm, this structure still features an efficiency of more than 80%. Although Fp does not perform as well as ϵ, the overall trend of improvement in Fig.5.7 (d) implies a good chance to maintain Purcell enhancement if we move the bridges to further nodes. The cost of this idea is the larger voltage applied to tune QD emission, which restricts the bridges from being too far from the cavity.

5.3 Discussion and conclusion

Throughout this chapter, we demonstrated the impacts of the additional structures for the implementation of electric contacts on the source performances of the devices.

The first studied SPS candidate is the Micropillar structure, to which we implemented three contact strategies.

Strategy I: A gold ring connected to the contact is placed on top of the pillar. The investigation of the ring-pillar overlap distance reveals that the Purcell factor and source efficiency can survive when the overlap is narrower than $\sim$1/10 of the pillar diameter. Beyond this range, the figures of merit would be destroyed due to the light absorption by the gold and the complicated scattering interference in the far field.

Strategy II: The conductive ITO slab is allocated on the Micropillar and mechanically supported by BCB. This additional slab brought an extra phase shift to the system. Therefore, the spectra oscillated with the slab thickness. The absorbing property of ITO led to a reduction in collection efficiency. Nevertheless, this strategy exhibited excellent potential to maintain the source performance with a proper choice of slab thickness from the numerical perspective.

Strategy III: Put the contact onto the terminals of the bridges surrounding the pillar. Implementing the bridges caused light penetration out of the cavity, leading to a worse Purcell enhancement and source efficiency unless the bridge width is smaller than 600nm compared to the pillar diameter of 2.2 μm. However, to our knowledge, such a width is feasible in fabrications, making this strategy stand out from other alternatives.

The ITO strategy was also implemented in the nanopost structure, where we found a similar shift in the spectra. However, in such a small device, the ITO slab is much closer to the cavity than that in the Micropillar structure, and therefore this source behaved more sensitive to the change of ITO thickness. Another strategy is building a single bridge connecting to the nanopost section, which is supposed to break the symmetry of the entire device. The simulations reported a massive difference between the two in-plane polarization, where the dipole polarized perpendicular to the bridge direction behaved much less affected by the bridge. In this scenario, the device can still maintain a decent source performance despite a relatively wide bridge compared to the nanopost size.

The third structure under consideration is the bullseye, where the contact interacts with the QD under the favor of bridges. The quantities of our interest revealed good tolerance to the bridge width. However, for a more straightforward implementation of the electric contacts without constructing the arms, we preferred the new-type hole-bullseye SPS device, where plenty of space on the mesa can be utilized, and direct interaction between the contact and QD is promised.

Ultimately, we talked about the bridge strategy in the on-chip nanobeam cavity. Locating the bridges in line with the QD is the most efficient position to tune the emission. However, this idea was defeated by the significant light leakage into the bridges. The proposed solution was moving the bridges to the nodes of the fundamental cavity mode to minimize light penetration. This strategy works when the bridge width is narrower than 40nm, beyond which the efficiency still survives while the Purcell enhancement is damaged.

CHAPTER 6

Conclusion and perspective

The development of quantum technologies is inseparable from the physical components that can support the running of quantum computations or communications. As one of the building blocks, highly-efficient and tunable SPSs become the main topic of this thesis. Semiconductor QD stands out from other single-photon emitters by its high brightness, deterministic property, and narrow spectral linewidth. For stronger SE and better photon collection, the coupling between QD and the surrounding nano-cavities are intensively studied in this project.

As shown in the first part of this thesis, we separately apply three numerical methods to analyze different structures and problems. Based on the mode expansion theory, the FMM is adopted to design and investigate the rotationally symmetric nanopost system. We also implement FEM to study all the other SPS devices demonstrated in this thesis. The last method, QNM approach, is mainly used to illustrate the contributions to the QD SE from individual modes, especially working around the fundamental cavity mode. In the second part, we roughly separate the QD-based SPSs into two categories regarding the photon collection directions: vertical emitted or on-chip.

The first investigated vertical-emission device, nanopost, is welcome for its simple and fabrication-friendly configuration and broadband property, which enables a good tolerance for the spectral misalignment of QD and cavity. The well-designed nanopost also possesses a remarkable Purcell enhancement and a decent far-field collection efficiency. QNMs are applied to explain the abnormal and asymmetric performance on the spectrum, and a nearly-perfect agreement between FMM and QNM approach is observed.

On the other hand, we are also interested in the high-quality cavities which can relatively suppress the phonon sideband and thus benefit the photon indistinguishability. Compared to the traditional broadband bullseye, the new-

type hole-CBG is promising to create a high-quality cavity due to the additional degree of freedom in the angular direction. Although an ultra quality factor is not found under current optimization strategies, the combination with an additional chirped section has the potential to construct a high-quality and high-efficiency CBG cavity. The last structure studied in this category is the physically tunable open double-cavity, which consists of a bottom planar cavity and a top mirror. From the numerical point of view, the dielectric mirror is more suitable than the gold mirror due to the photon absorption of the latter. After optimizing the open cavity length, we obtained an emission-SMF coupling efficiency of 28% in the end.

Regarding the on-chip SPS, we proposed a design procedure for a round holes-based nanobeam cavity, where the enhanced Purcell factor and a near-unity coupling efficiency with waveguide fundamental mode are achieved. The scattering loss caused by the mismatch between the cavity mode and the Bloch modes in the DBRs is reckoned as the main unfavorable factor to the source efficiency. We introduced the taper section to gradually erase the mode mismatch via an adiabatic transition and eventually obtained a comparable performance to the champion design. Considering the ease of fabrication, wider waveguides and larger elliptical holes are taken into the designs despite the cost of source performance. The cavity effect favors the enhancements of SE and the mode coupling in this device. Another idea for pursuing good efficiency is to implement other sections perpendicular to the waveguide direction to inhibit unwanted dipole emission. The on-chip SPSs are well suited for the combination with SNSPD. By simulating the waveguide propagation constant, we can finally predict the detector length, which enables a 99.9% light absorption. We also find the more significant the index-contrast of waveguide and substrate, the shorter the needed SNSPD.

The spectral tunability of QD is strongly required for better coupling with the nano-cavity and also for remote QDs interference. Among all the candidates, we choose electric tuning as the object due to its ability for QD environment charge stabilization. The additional structure or section for placing electric contacts can affect the performance of the original SPSs. In the last part of this thesis, we presented our perspectives on the impacts of different contact strategies in various nano-cavities.

For the Micropillar structure, a top-placed gold ring with an overlap narrower than 1/10 of the pillar diameter is safe for maintaining the SE rate and the source efficiency. If the gold ring is replaced by the conductive ITO slab, then the figures of merit oscillate with the slab thickness. Thus, carefully

choosing this value can always keep good source performances. Another strategy is locating the contacts on the terminals of the bridges around the central pillar. The efficiency and Purcell enhancement are well protected when the bridges are narrower than 600nm compared to the pillar diameter of 2.2μm.

We also implement similar strategies to nanopost. For ITO strategy, the close distance of QD and the top slab makes this device sensitive to the change in ITO thickness. On the other hand, the interference introduced by this additional layer can also modify the spectra. However, it's still promising to maintain the source performance if ITO is thin enough. For the single-bridge strategy in the nanopost cavity, we see significant differences between the dipole polarizations parallel or perpendicular to the bridge. The latter is less affected by the bridge and thus presents stable performances even though the bridge width is comparable to the nanopost radius.

Electric contacts are also applied to the CBGs. Although the bridge strategy works well for the traditional bullseye, the new-type hole-CBG is more straightforward for connecting QD and contacts and has admirable source performances. Lastly, the electric tuning in on-chip SPS is discussed. Placing the bridges in line with the QD is the most efficient position for our target. However, severe light penetration destroys the cavity effect. This problem is solved by moving the bridges to the far nodes of the cavity to effectively reduce photon leakage.

Overall, the waveguide-based SPS is better suitable for on-chip optical operation and can afford a direct deposition with SNSPD. PC-based on-chip device is now leading this field. However, for future large-scale linear optical quantum computing, semiconductor waveguides can be a strong competitor despite the fabrication-limited source efficiency for the time being. Besides, the Micropillar device has already been proven one of the most successful SPSs and has been applied in some quantum applications. However, due to the easier fabrication and more straightforward implementation of QD tuning, we are ambitious to design a new-type hole-bullseye SPS, which is supposed to possess a quality factor and source efficiency comparable to the world-record Micropillar. In addition, playing with the distribution of the holes is also possible to break the symmetric of the structure, which leads to a promising efficiency under resonant excitation. Here, the research challenge is the natural contradiction between strong in-plane light confinement and excellent vertical propagation. However, the results of Chapter 3.2 show good potential to overcome this trade-off. Regarding the electric tuning strategies for most structures discussed in Chapter 5, the construction of bridges around

the cavity is the most feasible and practical choice.

Appendices

APPENDIX A

Hole-CBG optimization strategy II

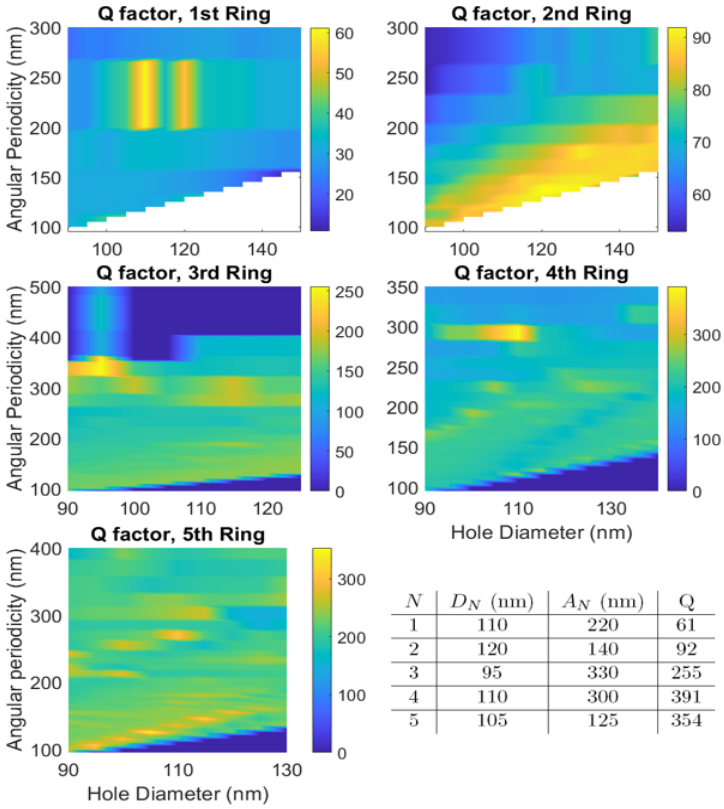

N	D_N (nm)	A_N (nm)	Q
1	110	220	61
2	120	140	92
3	95	330	255
4	110	300	391
5	105	125	354

Figure A.1. Ring-by-ring (1st-5th) optimization results of hole-CBG, the table shows the maximum Q factor and the corresponding structural parameters. All the data shown in white and purely-blue areas are none because the simulations are not carried out.

In Appendix A, we display the optimization results for the hole-bullseye structure under the optimization strategy illustrated in Chapter 3.2.1.2.

APPENDIX B

JCMsuite optimizer interface

In Appendix B, we introduce the interface of the JCMsuite optimizer, working for the chirped CBG cavity discussed in Chapter 3.2.2.

Current status	
sample computation time	20.99
acquisition time	149.2
running calculations	2
expected improvement	0.8949
probability of improvement	0.2142
number of acquisition samples	15
maximal number of GP evaluations	300
number of GP evaluations	287

Current optimum	
objective_value	-1.94
R	500
W	112
P	394.9
chirp	0.1168
shift	61.98
datetime	2023-05-19 09:53:46
iteration	1599

Figure B.1. Monitor for current optimization status and current optimum result.

Before running the optimizer, we set the target function and various ranges for the parameters of our interest, like the central radius R, trench width W, period P, chirp value, and the initial shift via Matlab. The main advantage of this optimizer is the automatic and simultaneous optimization of multiple parameters. The running status and the current optimum can be monitored via the tables shown in Fig. B.1. But we can also get an overview of all the results from the 3D plot of the objective function explorer displayed in Fig. B.2. The data of these colored dots are automatically saved in a text file, which is convenient to import into the data processing software.

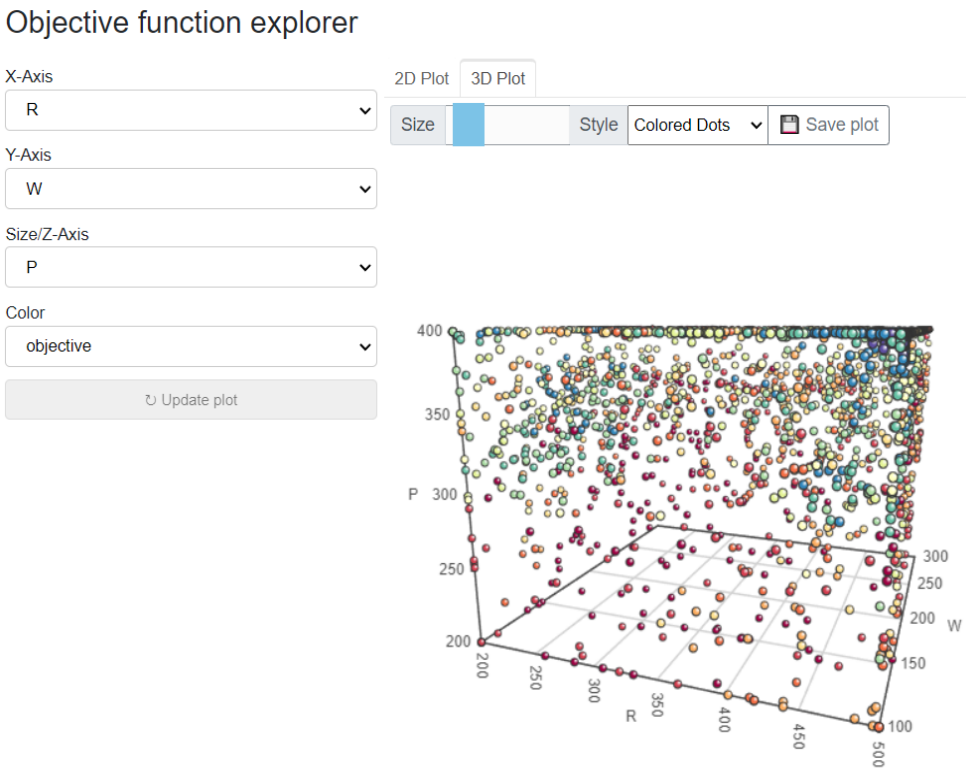

Figure B.2. 3D plot of the objective function explorer.

APPENDIX C

Manuscript under preparation

The tunable quantum-dot-based single-photon source: Strategies for implementing electrical contacts

Yujing Wang,[1,*] Claudia Piccinini,[1,*] Martin A. Jacobsen,[1] Luca Vannucci,[1] Sven Burger,[2,3] Battulga Munkhbat,[1,†] and Niels Gregersen[1,‡]

[1] *Department of Electrical and Photonics Engineering, Technical University of Denmark, 2800 Kongens Lyngby, Denmark*
[2] *JCMwave GmbH, Bolivarallee 22, D-14050 Berlin, Germany*
[3] *Zuse Institute Berlin, Takustraße 7, 14195 Berlin, Germany*

Efficient and tunable sources of single indistinguishable photons are essential for the development of future scalable optical quantum computers. However, traditional III-V semiconductor quantum dots in bulk suffer from poor photon collection, necessitating the engineering of photonic cavities to enhance extraction efficiency. Unfortunately, spectral detuning between the quantum dot and the cavity, resulting from fabrication imperfections, hinders efficient coupling and leads to unfavorable source efficiency. Achieving high indistinguishability of single photons is also challenging, because of the unstable charge environment of the emitter. Furthermore, the difference in the emission frequencies among individual quantum emitters and sources poses a bottleneck for efficient multi-photon interference processes, particularly in remote quantum interference scenarios. To address these challenges, researchers have pursued strategies for spectral tuning and charge stabilization of quantum emitters, such as strain tuning, temperature tuning, surface passivation, encapsulation, and electrical tuning and stabilizing with electrical contacts. However, the main challenge lies in finding ways to implement tuning and charge stabilization without compromising the efficiency of single-photon sources. In this Perspective, we emphasize the promising approach of electrical biasing/contact for emitter tuning and stabilizing charge noise in the device, while preserving its efficiency. Through extensive numerical simulations, we investigate various cavity geometries, including micropillar, bullseye, nanopost, and nanobeam cavities. Our simulation results provide valuable insight into the specific impacts of different strategies on the implementation of electrical contacts in single-photon source devices utilizing various electrical contact approaches, such as metal ring contacts, transparent oxide electrodes, and bridges. Additionally, drawing upon our existing knowledge of the fabrication of such devices, we provide our perspective on the practical concerns and considerations associated with implementing these strategies.

INTRODUCTION

The preparation, manipulation, control, and detection of quantum systems can be referred to as *quantum engineering*, and it has already emerged in the last two decades. Quantum computation, which includes quantum communication, quantum control, and quantum metrology, is one of its biggest challenges. Several physical platforms have been proposed for carrying out quantum computation so far; these include nuclear magnetic resonance (NMR), ion traps, cavity quantum electrodynamics (QED), quantum dots, superconducting circuits, and photonic platforms. Among them, the use of photons to encode and manipulate quantum bits, or qubits, has some advantages connected to their high-speed transmission and low degree of decoherence. Moreover, compatibility with the already mature integrated classical photonics allows the exploitation of existing foundry technology to enable large-scale processing. Photonic qubits can be encoded in different degrees of freedom, such as path [1, 2], frequency [3–5], orbital angular momentum (OAM) [6, 7] and polarization [8, 9] of light. Among several ways of generating single-photons, the spontaneous parametric down-conversion (SPDC) process represents a convenient approach [10]; however, its probabilistic nature limits the efficiency to a few percent. As an alternative, a two-level system, such as ion-traps [11], defect centers in solid-state materials [12], two-dimensional materials [13], and quantum dots [14], can provide the deterministic generation of single photons. Indeed, quantum dots [14] emerged as the most efficient source since photon emissions can be controlled one by one.

In this view, a key component in developing a scalable optical quantum computer involving thousands or millions of photons is an efficient tunable emitter of single indistinguishable photons [15]. A scalable optical quantum computer requires many individual single-photon source (SPS) devices, and all SPSs should provide single photons of identical wavelengths to enable coherent photon-photon interactions at the heart of optical quantum information processing [16, 17]. Since different SPS devices embedding different quantum dots will most likely emit single photons at different wavelengths from the outset, each device must be tunable to match very precisely with each other. Failure in generating one of the identical photon would compromise the quantum calculation. Although losses might be mitigated by quantum error correction [18], the scalability of future quantum technologies requires generating many identical photons from different emitters by individually tuning each SPS.

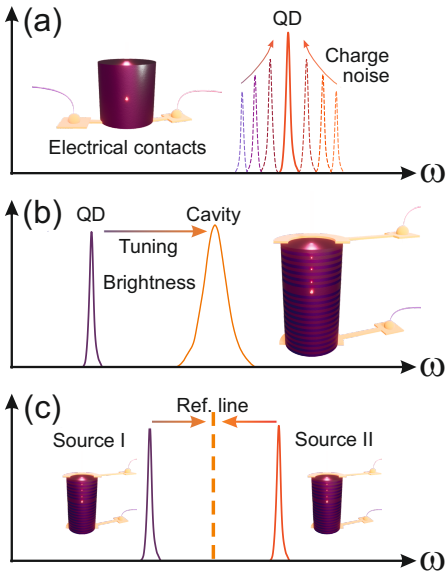

FIG. 1. (a) Stabilizing the charge environment helps reducing energy fluctuations induced by charge noise. (b) The QD emission needs to be carefully aligned with the cavity resonance, especially for high-Q factor cavities. (c) Successful quantum interference between two different emitters requires the spectral alignment of the two of them to some arbitrary reference line.

Due to the poor efficiency of a QD in a bulk material, it is necessary to place the QD inside a carefully engineered micro- or nanostructure, acting as an antenna directing all emitted photons towards the desired output channels. Currently, the most investigated structures are the photonic crystal cavity [19], micropillar cavity [20], photonic nanowire [21], and the bullseyes [22]. As depicted in Fig.1 (b), the resonant effect requires careful alignment of the QD emission line and the cavity resonance line. The most successful SPS design today for vertical emission of light into an optical fiber is the narrowband micropillar cavity [20, 23], where the cavity line is unchanged and the spectral alignment is achieved using Stark tuning of the QD line. However, active tunability of both the emitter line and the cavity resonance is essential to tune different SPS devices individually to a particular reference transition line (Fig.1 (c)). In this regard, introducing the open cavity approach [24] allowed an active control of the cavity resonance by varying the distance to the optical fiber. However, this technique requires a unique cryostat set-up equipped with expensive and high-precision piezo stages to tune the cavity resonance, which makes it challenging for future scalability.

Quantum interference between photons is required for a number of quantum protocols, such as boson sampling [25] and quantum key distribution [26]. One wait to achieve it is to rely on temporal-to-spatial demultiplexing of a single quantum emitter [27–29], even though this protocol presents limits connected to the fact that every consequent demultiplexing halves the photon flux on each channel, severely slowing down the computation rate in case of a large number of channels. On the contrary, a large-scale entanglement state can be possible by aligning several sources [30–34], potentially unlocking the quantum advantage for boson sampling and device-independent quantum key distribution with high key rates [35]. Additionally, GaAs QDs can be tuned to resonance with rubidium D1 and D2 atomic lines, offering an appealing opportunity to store photons in a rubidium-based quantum memory [36].

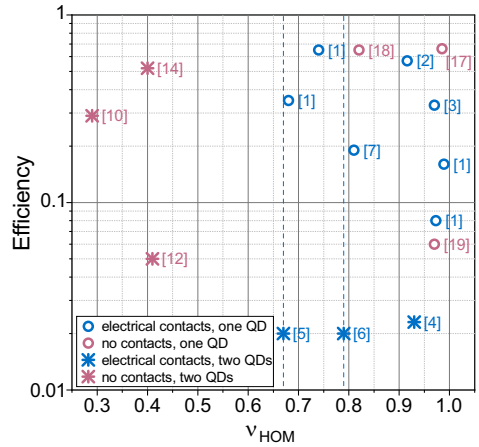

FIG. 2. Comparison between state-of-the-art SPS performances in terms of efficiency at the first lens and HOM visibility. The blue symbols correspond to electrically contacted QD SPS, while the redwood color corresponds to non-contacted structures implementing other tuning strategies such as temperature or strain. The round symbols show the performance of single photons produced from a single QD, while the stars account for the interference between two different dots. In this last case, the efficiency extracted from the references is associated with either the best efficiency among the two or the average between the efficiencies of the two SPS. The two vertical dashed line account for the fact that references [5] and [6] do not provide any value for efficiency.

The first demonstration of interference of photons from two different sources dates back to 2010, when Patel et al. applied electrical tuning to a quantum dot and tuned it into resonance with an electrically driven target quantum dot which was contained in another cryostat 1.1 m away [37]. While the most recent work demonstrates quantum interference experiments of identical photons using two completely separate electrically tunable QDs [33], exhibiting high visibility >93%. More importantly, this proves that achieving coherent photon-photon inter-

ference with multiple tunable sources is indeed possible. Although, generally, the efficiency falls short due to photon sideband filtering and the lack of Purcell enhancement, which can be improved by implementing photonic cavities. Fig. 2 reports the performances of state-of-the-art QD SPSs. The plot shows their HOM visibility degree on the x-axis and the extraction efficiency on the y-axis on a logarithmic scale. The legend tells whether the source is provided with electrical contacts and whether the photons used for the characterization come from the same QD or separate QDs. Those references non implementing electrical tuning, adopt either temperature tuning [20, 38–40], strain tuning [41] or planar cavity and no tuning at all [42]. The ideal device would be situated near the top-right corner of the graph, featuring unitary efficiency and indistinguishability. Despite recent progress, individual deterministic tuning of both the emitter and the cavity for efficient SPSs still remains an open and major challenge.

This Perspective gives an overview of the methods implemented so far to tune quantum dot single-photon sources, specifically focusing on different types of electrically contacted photonic cavities. Acknowledging the contribution of previous research, we aim to optimize specific geometries with a focus on micropillar, bullseye, nanopost, and nanobeam cavity structures and introduce our own results obtained from finite element method (FEM) simulations for geometry optimization by applying the commercial program package JCMsuite. Such optimization is crucial for boosting the collection efficiency ε of single photons and increasing their coherence time T_2 by Purcell enhancement, potentially approaching the theoretical limit $T_2 = 2\,T_1$, where T_1 is the lifetime of the neutral exciton [43]. Although the spatial and spectral alignment of the quantum emitter with the cavity is necessary, the former is not part of the scope of this manuscript. However, we want to point out that there are several strategies to deterministically position nanostructures with uncertainties below 20 nm [44, 45].

CHAPTER

Self-assembled QDs are grown via the Stranski-Krastanov growth mechanism. Epitaxial deposition of a material with a lattice parameter different from that of the underlying material will trigger the formation of island-shaped structures on top of a so-called *wetting layer*. For example, InAs has a lattice parameter that is 7.2% larger than GaAs and 3.2% larger than InP. Self-assembled QDs offer several benefits compared to other types of QDs, such as lithographically patterned QDs. One of the primary advantages is their relatively high degree of uniformity in size, shape, and composition. This uniformity results from the self-organizing nature of QDs, which allows them to pack together in a regular array with minimal defects [46]. In addition, self-assembled QDs have been shown to have higher photoluminescence quantum yields, which means they emit more light per absorbed photon [47]. However, the random nature of the nucleation process and the diffusion of material on the surface will produce an ensemble of quantum dots of slightly different sizes and compositions [48]. As a consequence, when a photonic cavity is structured around each QD, it is necessary to take into account that each one of them requires different parameters to match and enhance the emission spectra. Even in doing so, there is a very low probability that the cavity and the emitter are spectrally aligned with a precision of the order of meV, especially if the cavity has a high-quality factor (Q).

Among the post-growth tuning mechanisms, the simplest is changing the temperature; for example, by adjusting the temperature in a cryostat [49], or by implementing electrical heaters [50]. This will alter the electronic band structure and increase or decrease the bandgap. Changing the temperature of the semiconductor will also affect the lateral expansion of the material and shift the cavity resonance as well, even though the effect is much less relevant than the one on the QD.

Other methods involve the application of an external magnetic field [51], or strain [52]. However, the most promising, integrated, and scalable is electrical tuning by the Stark effect [53–56]. The quantum-confined Stark effect (QCSE) allows for fine-tuning the optical transition frequency of the QD, affecting Coulomb and exchange interactions among the charge carriers [57–59]. Moreover, by implementing additional blocking barriers and tunnel coupling to a Fermi reservoir, it is possible to load the QDs with a defined number of charges deterministically. This is typically done by embedding the QD layer in a diode structure [12] by changing the relative concentration of different elements layer after layer during the epitaxy, such that the energy band configuration facilitates the transport of carriers by applying reverse or forward bias along the growing direction of the structure. Control over the charge environment around the QD allows one to stabilize its state by Coulomb blockade [60] and drastically reduce charge noise [12, 61]. Consequently, the spectral wandering of the central frequency and the spectral broadening of the emission lines above the transform limit will be strongly reduced. This represents the third reason for applying electrical contacts to these QD-based SPS devices, as pointed out in Fig.1 (a).

However, this procedure is not trivial in terms of fabrication because of the multiple critical steps needed to etch the cavities and apply the contacts. The chip has to go through several optical and electron-beam lithography processes, dry etch processes, metal deposition, and bonding. Furthermore, it is crucial to design them in a way that does not worsen the efficiency of the source itself and the purity and indistinguishability of the generated photons. Although in the last few years there have been

many theoretical studies regarding the optimization of devices' geometries of different types [62–65], very few of them include the application of metal contacts [66, 67].

These are the motivations that led us to the study and characterization of the performances of different cavities providing the possibility to be wire-bonded at two different external pins providing the electric potential. From now on, we will provide more specific and deep insights into optimal contact design, addressing the mentioned cavities one by one. Based on the numerical simulations and the experimental knowledge, we leave our comments on the operability and the preference among all the tuning strategies discussed in this Perspective.

MICROPILLAR

Contacting a vertical micropillar structure was successfully realized already in 2008. Böckler et al. [68] fabricated and characterized an electrically pumped micropillar cavity. Working in the weak coupling regime, they obtained a Q factor as high as 16000 and a Purcell factor of about 10 from a 4 μm diameter pillar. On the other hand, Kistner et al. [69] demonstrated that electro-optical resonance tuning of the same structure can be exploited to tune the QD by QCSE and achieve strong coupling. In the following year, the same research group used the device to produce on-demand single photons, reaching a g^2 value of 0.13 for a 2 μm pillar and a high generation rate (35±7 MHz) and an overall efficiency of 34±7% for a 3 μm pillar [70]. After two more years, they demonstrated the electroluminescence of a site-controlled QD (SCQD) deterministically integrated into a micropillar resonator. One drawback of this cavity geometry that needs to be tackled is the rather inefficient extraction of light (max 34% and 50% for the latter works, respectively) due to the obstruction on the top facet of the pillar given by the gold contact lying on top of it. Moreover, the above-mentioned sources are electrically excited, but the same issue would affect the efficiency of the injection of light in case of resonant or close-to-resonance optical excitation.

Here, we report theoretically high source efficiency and Purcell enhancement from the micropillar structure using different contact strategies. The layout implemented for the following investigations considers a couple of mirrors that enclose the GaAs layer containing the QDs. Such mirrors consist of 40-layer pairs for the distributed Bragg reflector (DBR) on the bottom one and 17 pairs for the one on top. The thickness of the cavity layer is 256.1 nm, and those in DRBs are 74.8 nm ($Al_{0.85}Ga_{0.15}As$) and 64.0 nm (GaAs), respectively.

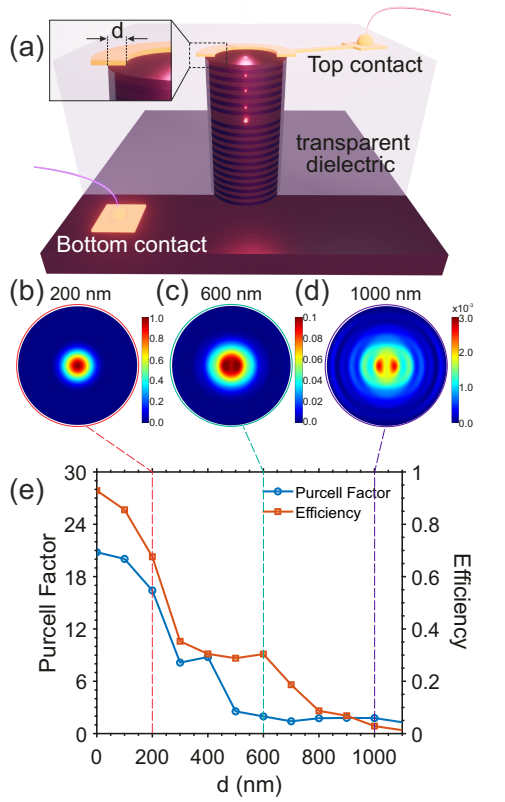

FIG. 3. (a) Sketch of the micropillar SPS surrounded by the transparent dielectric material BCB and covered by a gold ring on top. The pillar consists of two GaAs/$Al_{0.85}Ga_{0.15}As$ DBR mirrors and a GaAs cavity between them, with the QD at the center of the cavity. The inset shows the overlap distance of d between the central pillar and the gold ring. The material BCB (refractive index n=1.54) around the micropillar is mechanically used to support the gold ring. Normalized far-field emission patterns when the overlap d is (b) 200, (c) 600, and (d) 1000 nm, respectively. (e) Purcell enhancement Fp and source efficiency ε as a function of ring-pillar overlap d.

Gold ring contact

Considering the ease of connecting contacts, the gold ring scheme sketched by Fig. 3 (a), is the first strategy investigated in simulations. The pillar diameter is fixed at 2.2 μm, and the difference between the ring's inner and outer diameter is 6 μm. We tune the overlap d by changing the inner diameter and then investigate the impact of the gold ring on the source performance.

Fig. 3 (e) illustrates the response of the Purcell enhancement Fp and the source efficiency ε to the change of ring-pillar overlap. Our study reveals that they are

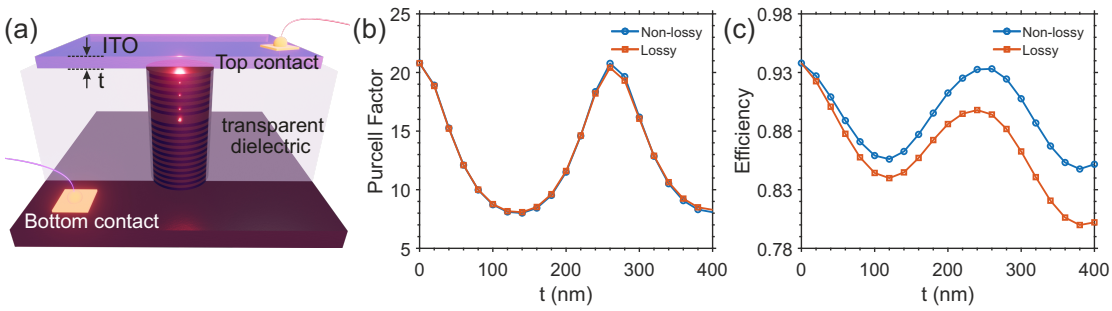

FIG. 4. (a) Sketch of the micropillar structure surrounded by BCB material and covered by an ITO slab, whose thickness is represented by t. (b) Purcell factor Fp, and (c) source efficiency ε, as a function of t, when considering/ ignoring the lossy property of ITO with a corresponding refractive index n_{ITO}=1.712+0.01i/n_{ITO}=1.712.

sensitive to implementing an additional gold ring, especially when the overlap is more than 200 nm, from where we can see a cliff-like drop in performance. Firstly, the absorbent property of the gold material can reduce the number of photons reaching the lens, and the more the ring overlaps, the more significant the reduction. Secondly, the complicated scattering and the corresponding interference introduced by the gold ring can significantly affect the far-field emission patterns of the structure, as shown in Fig. 3 (b) to (d). We can see the far field is increasingly more split towards the outer area, which directly reduces the proportion of photons within the numerical aperture (NA) of the lens and correspondingly destroys the source efficiency. Nevertheless, making the overlap around 200 nm is feasible in fabrication [70] and still can maintain a Purcell enhancement of 15 and an efficiency of 60%.

ITO planar contact

As depicted by Fig. 4 (a), the second strategy is to cover the top of the micropillar device by attaching an Indium Tin Oxide (ITO) slab, which is a type of transparent and conductive material. The central pillar is surrounded by benzocyclobutene (BCB), being used to support the ITO mechanically. Fig. 4 (b) and (c) indicate the impact of the ITO slab on the Purcell factor and the source efficiency, respectively. To figure out the influence of the lossy property of the ITO material, we consider both the lossy and non-lossy conditions; the latter is carried out by simply erasing the imaginary part in the refractive index. The ITO layer induces an additional phase-shift, resulting in periodic oscillations of F_p and ε. For non-lossy conditions, we can expect a comparable performance to the device without an ITO slab by carefully choosing the slab thickness. In this case, ITO does not generate other effects than phase change. On the other hand, Fig. 4 (b) still reveals the robustness of Fp under lossy configuration, thanks to the long distance from the ITO slab to the QD position. Conversely, we observe a decrease ε on top of the above-mentioned oscillating behavior in Fig. 4 (c). This is mainly due to the absorption of photons emitted upwards from the micropillar by the lossy ITO slab. However, even considering the intrinsic loss of the material, the peaks in Fig. 4 (c) tell a slight reduction of source efficiency from 94% to 90% when thickness t is around 250 nm, which indicates this strategy has good potential to keep the SPS performance.

Lateral bridge contact

Another solution for contacted pillar was presented in 2016 by Somaschi et al. [71]. In this case, the vertical body is connected to a surrounding circular frame by four 1.5-μm-wide wires, which allows to define the top p-contact. The devices realized featured a groundbreaking purity and indistinguishably under resonant excitation of 0.0028±0.0012 and 0.9956±0.0045, respectively. However, the brightness is estimated to be not more than 16%. When non-resonant excitation experiments the brightness scales up to about 65%, although the second-order autocorrelation and the mean wave-packet overlap decrease. These results reiterate the undeniable trade-off between these three figures of merit for SPS quality assessment.

Inspired by this idea, we introduce the third strategy under investigation: building bridges around the central micropillar and placing the electric contacts on top of the bridges' terminals. We fix the bridge length at 1 μm and change the bridge width to study the impact of the bridges on the SPS performance. As depicted in Fig. 5 (a), we initially implement a four-bridge scheme. Fig. 5 (b) and (c) are the far-field emission pattern and the vertical field propagation when the bridge width is half of the micropillar radius. Under this configuration, both

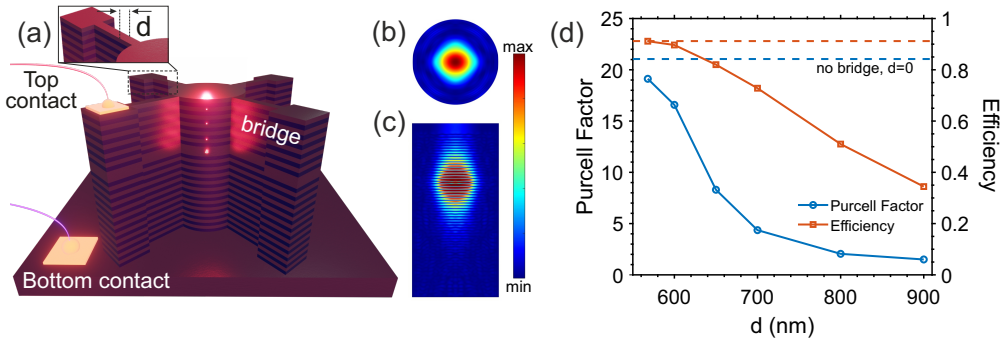

FIG. 5. (a) Sketch of the micropillar with four surrounding bridges, whose lengths are 1 μm and widths are w. (b) Normalized far-field emission pattern and (c) vertical field propagation throughout the device when the bridge width is half of the micropillar radius. (d) Purcell factor Fp and source efficiency ε as a function of bridge width. The dashed lines indicate the original Purcell factor (blue) and source efficiency (orange) of the micropillar device without the bridges.

two field profiles are slightly modified by the four bridges. To quantitatively analyze, we investigate the impact of bridge width on the Purcell factor and source efficiency. Fig. 5 (d) indicates that broadening the bridge width to over 600 nm for this configuration can significantly destroy the SPS properties, and both Fp and ε sharply drop. This deteriorates the confinement of the cavity mode via leakage of photons into the bridges. Nevertheless, a bridge width of 550 nm is promising to maintain the identical source performance and is still feasible in fabrication. One can consider another two-bridge configuration, which can naturally break the degeneration of x and y-polarized modes. This strategy leads to a total source efficiency of 50% by considering both dipole orientations. The encouraging point is that it shows the potential to break the bottleneck of 50% filtered efficiency under the resonant excitation scheme.

Fabrication challenges and discussion

To briefly summarize, the ITO strategy performs best of the three: it can keep an identical Purcell factor and a source efficiency of 90% by choosing a suitable slab thickness. ITO is a rather interesting material in both research and industry due to its good electrical conductivity and high optical transparency, the two being inversely correlated and dependent on the thickness of the layer. In the field of nanotechnology, it is mainly used in solar cells [72]. For our specific application, it is relevant to consider that BCB planarization requires a curing step at relatively high temperature (350°C), resulting in excellent dielectric and mechanical properties. Consequently, the following heating for the sputtering of ITO should not represent a problem as long as the BCB preserves its sheet resistance and transparency properties.

Regarding the gold ring realization, the same concerns about the BCB need to be addressed, however gold rings with d =?? have already been implemented [68–70, 73]. We are confident that the realization of the hereby proposed specifications can be achieved. However, it should be noted that particular attention must be paid to ensure that the ring and the pillar are carefully aligned; otherwise, both the Purcell factor and the efficiency will drastically drop. Such displacement solely depends on the e-beam lithography alignment and precision.

Nevertheless, the design including bridges that provide access to the vertical structure involves more implications for the fabrication process. Firstly, non-optimized etching recipes will most likely not give straight walls and the base of the pillar and their bridges risk being over-etched. In such a case, the whole structure becomes too fragile, especially when the bridges become narrower and narrower. In the worst case, the bridges may also become detached from the pillar and/or the pillar may collapse. One way to solve this may be to implement polymer planarization also in this case, sacrificing some optical confinement of the field mode. It should be noted that doping is necessary to realize optimal electrical control of the QD source. However, doping introduces optical losses which are not included in our numerical simulations. More recent structures are usually made by doping all the DBR layers from the bottom of the structure to its top following a gradient. The so-called δ-doping follows a gradient (lower next to the intrinsic layer and higher at the extremities), such that the optical losses due to absorption are minimized while maintaining good charges injection [68, 74, 75]. To minimize the impact of doping, we want to suggest a better strategy by moving the contacts as close to the QD layer as possible. In this way, only a few DBR layers need to be doped, and we believe this will help improve the source performance in the end. A straightforward idea is to etch down the bridges. How-

ever, this will bring unexpected asymmetry to the cavity and make it negatively change to some extent. Based on this consideration, we believe it would be better to keep the bridges but etch the connected pads down to the DBRs near the QD layer. These pads are where we locate the electric contacts. They are far from the central pillar, so the impact on the cavity would be reasonably small, and thus etching the pads or not wouldn't affect the source performance in simulations. However, from an experimental point of view, this strategy is genuinely beneficial to narrowing the doped area and reducing the photon losses. The literature has already reported an attempt to implement this idea back in 2007 [76], even though the performance of the device is no longer competitive nowadays, due to its non-optimized design.

BULLSEYE

The bullseye (or circular Bragg grating, CBG) structure is an SPS design that features a good Purcell factor, remarkable source efficiency, and a broad bandwidth, which is friendly to QD alignment. Successful electrical tuning of CBGs has only recently been realized. Among all, the work by Schall et al. describes the development of electrically controllable Quantum-Dot-Molecule (QDM) devices with excellent optical and quantum optical emission properties. They are based on stacked quantum dots in a pin-diode structure that are subsequently deterministically integrated into a CBG using in situ e-beam lithography [77]. At the same time, a team from the University of Cambridge was working on a novel design that would be compatible with carrier injection. This considers leaving four semiconductor bridges that connect the central disk, containing the QD, to some n- and p-type contacts image. The reported theoretical Purcell factor and dipole collection efficiency (DCE) are 20 and 70%, respectively. It is also shown that the presence of such bridges clearly affects the confinement of the mode in the cavity. As a consequence, the F_p and the DCE result more or less deteriorated depending on the width of the bridges [78]. A practical realization of such a tunable device with tapered lines acting as bridges to the central structure exhibited single photon emission lifetimes as short as 80 ps and lead to transparency in the cavity reflectivity of 80%.

Here, we implement four bridges to a simple regular bullseye design as shown in Fig. 6 (a), which consists of a central disk and four outer rings on top of the substrate. The disk and rings are made of GaAs. The substrate comprises a SiO_2 slab, a gold mirror, and a Si layer. In addition, the InAs QD with a dipole orientation along the bridge direction is located in the center of the central disk. The structure in our work has the following parameters: the radius of the central disk R = 360 nm, the periodicity of the rings P = 360 nm, the trench W is 108 nm, the thickness of GaAs, SiO_2, and Gold layers are 170 nm, 250 nm, and 100 nm respectively. The Purcell factor and source efficiency of this regular bullseye structure without the bridges are 20 and 88.7% when NA of the first lens is chosen as 0.82. The impact of the width of the bridges on the resonance of the cavity, Purcell enhancement, and source efficiency is reported in Fig. 6 (d), where we fix the bridge length at 3.5 μm. Without the bridges we obtain $F_P = 20$ and $\varepsilon = 88.7\%$. With the increase of bridge width, the cavity resonance starts to red-shift. Moreover, the on-resonance Purcell factor increases first and then decreases, leaving an optimum Fp of 25 when the bridges are 150 nm wide. The rise in the left part benefits from the additional pattern in the angular direction, compared to the single radial pattern in the classical bullseye structure. Although the physical reason is not clear yet, Ref.[79] has proved the remarkable enhancement of the Purcell factor resulting from the angular pattern in the bullseye. However, as the bridges are widened, the cavity mode is damaged, which leads to increased photons penetrating the bridges. Therefore, we see decreases in the right part of Fig. 6 (d). Another figure of merit is the on-resonance source efficiency ε, which is negatively affected by the widening of the bridges, as indicated by the dashed curve. ε is almost halved when the bridge width is 300 nm compared to the bare bullseye. The reduction in efficiency firstly results from the photon in-plane leakage. On the other hand, the bridges can also modify the far-field emission pattern of the whole device. The modification can be observed from the comparison between Fig. 6 (b) and (c). (b) corresponds to the bare bullseye, and (c) is obtained from the bridge-bullseye structure when the bridge width is 60 nm. We can see the implementation of the bridges causes the light to diverge in the far field beyond the NA range, which is a negative factor to the source efficiency. However, Buchinger et al. [80] proposed other strategies, including changing the number of bridges and even rotating the bridges, which are both possible to achieve higher efficiency than the four-straight-bridge scheme discussed in this work. Nevertheless, it is still promising to maintain a good SPS performance by controlling the bridge width below 150 nm in our configuration, which is a feasible value for fabrication. These results also indicate the possibility of choosing the resonance wavelength in a relatively large range by simply changing the bridges' width instead of making a new bullseye design. We also observe very similar behaviors when the dipole polarization is 45-degree to the bridge.

Recently, Jeon et al. have proposed a CBG device with gratings made of holes instead of fully-etched rings and demonstrated an impressive enhancement in F_p and Q factor compared to the regular CBG [79]. Whereas the regular CBG is made of a series of disconnected dielectric rings, this new design results in a connected dielectric structure and offers a simpler way to interact with the QD, without integrating the bridges. From the numeri-

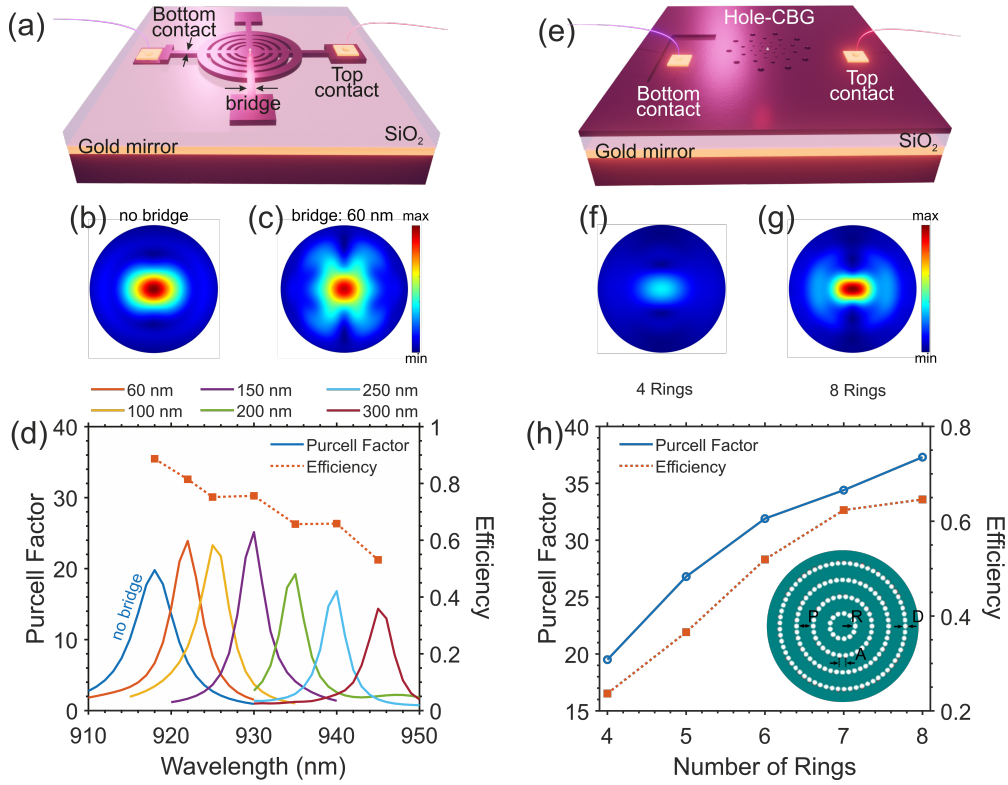

FIG. 6. (a) Sketch of the bridge-bullseye structure, with a QD embedded in the center of the central disk. Normalized far-field emission patterns (b) without/ (c) with 60 nm wide bridges. (d) Purcell factor as a function of wavelength when the bridge width varies in the range of 0-300 nm, where 0 nm refers to no bridge. The points on the dashed curve are the corresponding efficiencies when the dipole is resonant with the cavity mode. (e) Sketch of the hole-bullseye design with 3 rings. Far-field emission patterns of the (f) 4-ring, and (g) 8-ring structure, normalized by the same field intensity. (h) On-resonance Purcell factor (blue) and source efficiency (orange) as a function of ring numbers in the hole-CBG device without the boundary.

cal perspective, the efficiency of the structure with a fixed boundary, like the classical CBG, can go up to ∼80%, which is appreciated in our consideration. However, the relatively narrow boundary prevents a direct implementation of the electrical contacts, due to the lack of space. Therefore, we remove the boundary of the structure in this work, meaning that all the layers are freely extensive in the horizontal direction, which provides plenty of space for the contacts, as shown in Fig. 6 (e). In this work we use a central disk radius R = 208.2 nm, radial pitch P = 332.6 nm, hole diameter D = 95 nm, and angular periodicity A = 160 nm, all determined after a rough numerical optimization. Fig. 6 (h) demonstrates the impact of the number of air-hole rings on the Purcell enhancement and the first-lens collection efficiency within NA=0.82. Both figures of merits are enhanced by increasing the ring number and tend towards saturation for large number of rings, with F_p = 37.3 and ε=64.6% for 8 rings. The far-field profiles of 4-ring and 8-ring structures displayed in Fig. 6 (f) and (g) reveal that a larger number of rings increases the field intensity without modifying the shape. Considering the decent F_P and ε obtained here, and the ease of contacts integration, we believe the hole-bullseye device is a more promising candidate than the traditional ring-CBG structure with respect to a good tunable SPS.

Regarding the fabrication aspect, the challenges connected to the realization of these bridges are less compared to the bridges required for micropillars. Indeed, even though the optimal bridge width found is more than 3 times smaller, the etch is much shallower than what is needed for the vertically distributed mirrors and the bridges are connected all the way through the circular grating. This results in a more robust structure. On

the other hand, the hole-CBG is more troublesome because etching sizes smaller than 100 nm might not turn out successful. That is why there is a fabrication limit below which it would be risky to push because partial or non-etching of some holes will unavoidably break the circular symmetry and reduce the spatial confinement of the field.

NANOPOST

The nanopost SPS design can be seen as the truncated and, to some extent, simplified version of the tapered and inverted tapered nanowire [66], see Fig. 7 (a). Despite its simplicity it features remarkably good Purcell enhancement and source efficiency [81]. Theoretical work shows that F_P=7.9 and ε= 0.69 can be reached and similar values can be maintained over a broad spectral range [82]. Similarly to the bullseye, its main advantage compared to the high-Q cavities is that the large operating bandwidth relaxes the spectral matching requirements [83–85].

The original nanopost consists of a truncated GaAs nanowire on top of a gold mirror and a 13 nm thick SiO_2 slab. This structure is designed for an InAs QD, which can emit photons at around 930 nm. In numerical simulations, we consider the semiconductor QD an in-plane point dipole under the dipole approximation. The diameter of the truncated nanowire is 250 nm, and the height is 461 nm. We locate the on-axis dipole to the second antinode inside the cavity, which is 268.7 nm from the bottom of the post. The figures of merit considered in this work are the Purcell enhancement $Fp = P_{total}/P_{bulk}$, and the source efficiency $\varepsilon = P_{collected}/P_{total}$, where P_{total} is the power emitted by the dipole, P_{bulk} is the dipole emission in bulk material, and $P_{collected}$ is the power collected by the first lens. We perform the FEM simulations for this nanopost structure under the first lens NA of 0.75.

The first electrical tuning strategy is to suspend a slab of ITO on top of the nanopost (similar to Fig. 7 (a), but replacing the transparent dielectric material with air), using e.g. pillars away from the structure to support the ITO mechanically (not considered in numerical simulations). The upper contact is attached to the ITO, while the lower contact is directly bonded to the gold bottom mirror. The ultra-thin glass layer between the cavity and the gold allows the electrical current to reach the doped cavity. Fig. 7 (b) and (c) demonstrate the impact of ITO thickness t_{ITO} on F_p, and ε. The bare nanopost structure gives a Purcell enhancement of 7.9 and an efficiency of 40% at 930 nm. By increasing the thickness of ITO, the cavity resonance indicated by the largest Purcell factor in Fig. 7 (b) firstly redshifts and then blueshifts back, which results from the overall phase change introduced by the ITO slab. On the other hand, the on-resonance peak Fp gradually decreases in this process, which is the consequence of the absorption of ITO. Similarly, the source efficiency experiences spectral shifting and an overall decrease. However, the reduction on ε is relatively smaller than that on Fp, suggesting the efficiency is more robust than the Purcell enhancement in the ITO-Nanopost structure.

Better mechanical stability may be achieved by supporting the ITO slab with BCB material surrounding the nanowire, as depicted in Fig. 7 (a). As shown in Fig. 7 (d), we obtain much lower F_p compared to the suspended case because the refractive index contrast of GaAs with BCB is lower than GaAs-air, thereby inducing weaker optical confinement. Here, we adjust the structural parameters to ensure the nanopost-BCB design has a decent source performance, primarily targeting a reasonable collection efficiency. Nevertheless, we obtain rather good $\varepsilon \approx 0.45$ by implementing a thick ITO slab, as shown in Fig. 7 (e). By comparing Figs. 7 (d) and (e) we observe that high F_P and ε cannot be achievesd simultaneously, thereby imposing a trade-off between the two figures of merit when choosing the thickness of the ITO slab.

A different contact strategy consist in adding a single bridge directly connected to the nanopost, and attaching the metal contact to the end of the bridge[Fig. 8(a)]. This single bridge breaks the rotational symmetry of the original nanopost structure, which means the dipole orientation may significantly affect the overall source performances. Here we consider a bridge of length 1 μm along the x-axis and investigate the device's properties for dipole orientation along the x-axis and the y-axis, respectively. The comparison of the field distributions shown in Fig. 8 (b) strongly indicates that the cavity mode penetrates less into the bridge for a y-polarized dipole, i.e. when the dipole is perpendicular to the bridge orientation. Moreover, the far-field pattern from the x-polarized dipole shows clear signatures of bridge-induced scattering [see inset of Fig. 8 (c)], whereas the far field emission from a y-polarized dipole is more concentrated within the NA of the first lens [inset of Fig. 8 (d)].

From a quantitative aspect, the impact of the bridge width in the range (0, 100) nm on Fp and ε is studied in Fig. 8 (c) to (f). As shown in Fig. 8 (c) and (d), two polarization configurations both redshift with increasing bridge width w. However, the y-polarized dipole is less affected by the x-oriented bridge in terms of the resonance spectral shift (maximum 10 nm for the y dipole, compared with 100 nm for x) and reduction of the on-resonance Purcell enhancement (12.5% and 50% for y- and x-dipole, respectively). Finally, the bridge has little influence on the efficiency from a y-polarized dipole, while the x dipole shows again clear signatures of scattering [Figs. 8 (e) and (f)]. It is worth noticing that with a bridge width of 100 nm, which is comparable to the nanopost radius, we can still observe a Purcell enhancement of 7 and a source efficiency only 5% lower than the bare structure, showing that the single bridge strategy is promising to maintain good SPS properties when the

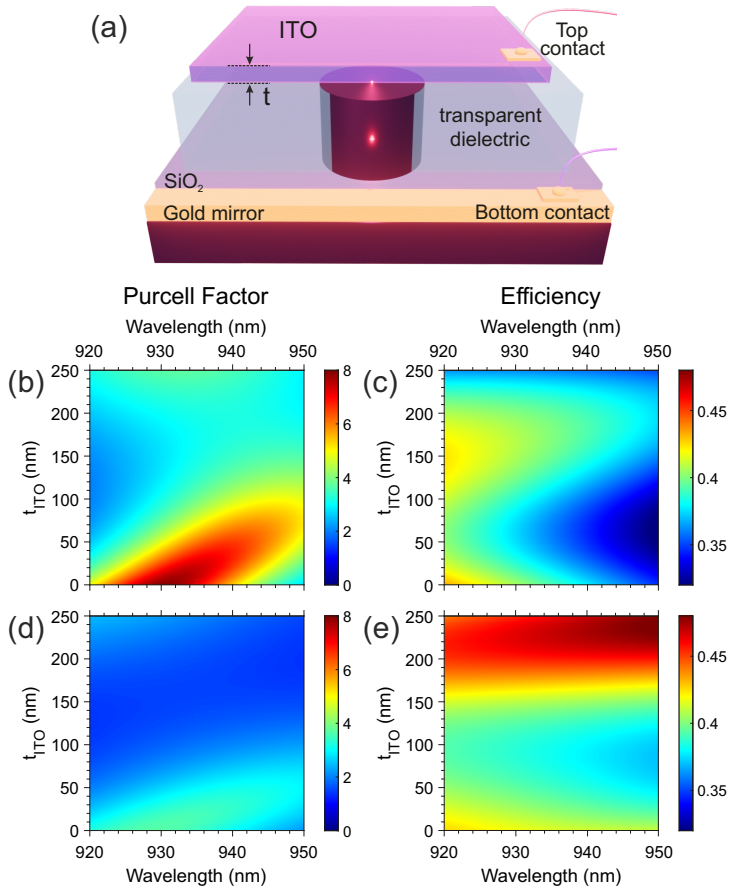

FIG. 7. (a) Schematic of the electrically tuned nanopost structure with an ITO slab mechanically supported by the BCB material surrounding the truncated nanowire. (b)/(d) Purcell enhancement Fp and (c)/ (e) source efficiency ϵ as the functions of wavelength λ and the thickness of ITO slab t_{ITO} in suspended configuration/ BCB supporting configuration.

dipole and bridge have orthogonal orientations.

The collection of single photons from this type of geometry has not been demonstrated yet, even though the experimental realization [81] of this concept promises good performances in the realm of quantum light sources.

NANOBEAM CAVITY

In the nanobeam cavity, sketched in Fig. 9 (a), the QD is sandwiched by a periodic pattern of holes defining two DBR mirrors thanks to the photonic bandgap effect. As such, it behaves essentially as a one-dimensional photonic crystal [86]. The nanobeam is thus a waveguide-based design suitable for on-chip integration of SPS sources, potentially enabling improved performances in terms of ease of operation, stability, reduced losses, size, and speed. Sources of this type have demonstrated exceptional coupling of the emission in a waveguide mode close to unity [87]. Moreover they are capable of achieving a remarkably high Q factor and extremely small volume confinement [88, 89]. The electrical contacting of such a platform has been worked out for different purposes [90–92], among which tuning a photonic crystal cavity over a surprisingly broad range without shifting the QD exciton energies [93], even though tuning the QD emission has not been significantly explored yet.

In our bare design, the bottom mirror consists of 9 regular air holes, whose radius is 40 nm, and a taper section, where the hole radius linearly decreases from 40 nm to 20 nm with a 1 nm step size. The top mirror comprises 12 regular holes with a radius of 20 nm. This nanobeam

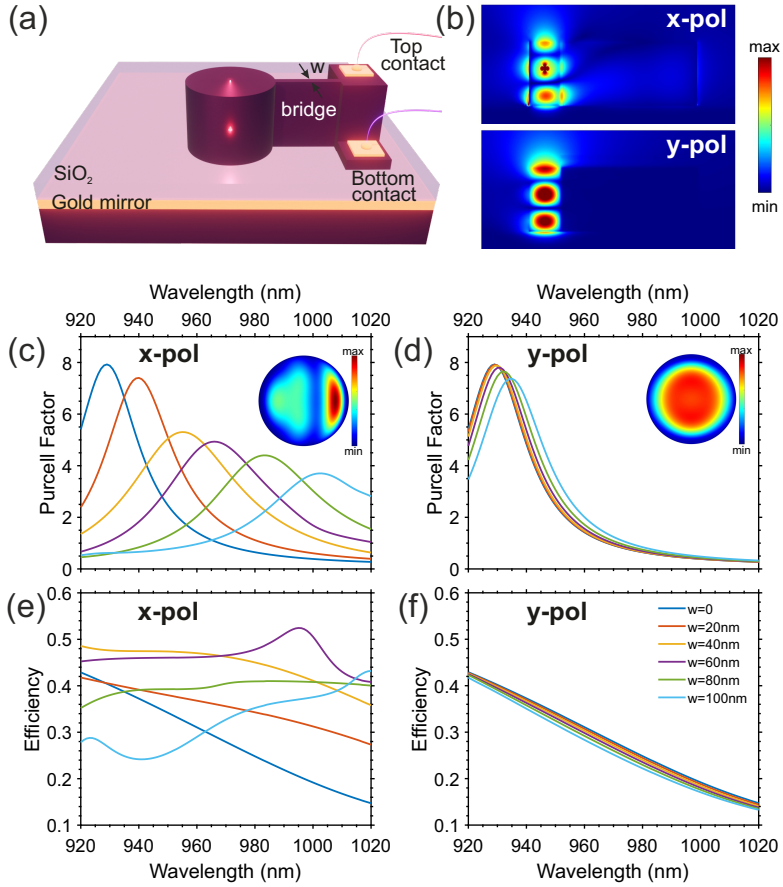

FIG. 8. (a) Sketch of the nanopost-bridge strategy. (b) Vertical field propagation in the structure with x/y-polarized dipole. (c)/(d) Purcell enhancement Fp, with insets showing the far-field emission pattern when the dipole polarization is along/perpendicular to the bridge orientation, and (e)/(f) source efficiency ϵ as a function of wavelength λ for x/y-polarized dipole when the bridge width varies between 0 nm 100 nm. Here, we assume the bridge extends along the x-axis.

cavity features a remarkable Purcell factor of 38 and an outstanding near-unity source efficiency of 97.7% when the QD is at the center of the cavity [94]. Here we add two wing bridges to the bare structure to implement the electrical tuning. A straightforward possibility is to locate the 800 nm-long bridges in line with the dipole position, which is carefully positioned at an antinode of the electromagnetic field profile. However, this will likely induce strong light penetration into the bridges as seen by the field profile in Fig. 9 (b), which would strongly deteriorate the source performance. An alternative solution is to move the bridges away from the QD and put them at a node (instead of an antinode), where the electromagnetic field intensity is minimum and losses into the bridges are likely smaller. Figure 9 (c), where we locate the bridges at the third node relative to the cavity center (in both directions) qualitatively indicates that much less light goes indeed into the wings, supporting the feasibility of this solution. In Fig. 9 (d) and (e) we analyze the impact of the bridge width on the Purcell factor and the source efficiency when putting the wings at different locations. Here, the Purcell factor is evaluated for the x-polarized dipole, and the source efficiency ε, which is defined as the proportion of the light funneled into the fundamental waveguide mode, is assessed for the xy-polarized dipole. Both F_p and ε are strongly affected by the bridges when the latter are spatially in line with the dipole position. The Purcell factor drops from 38

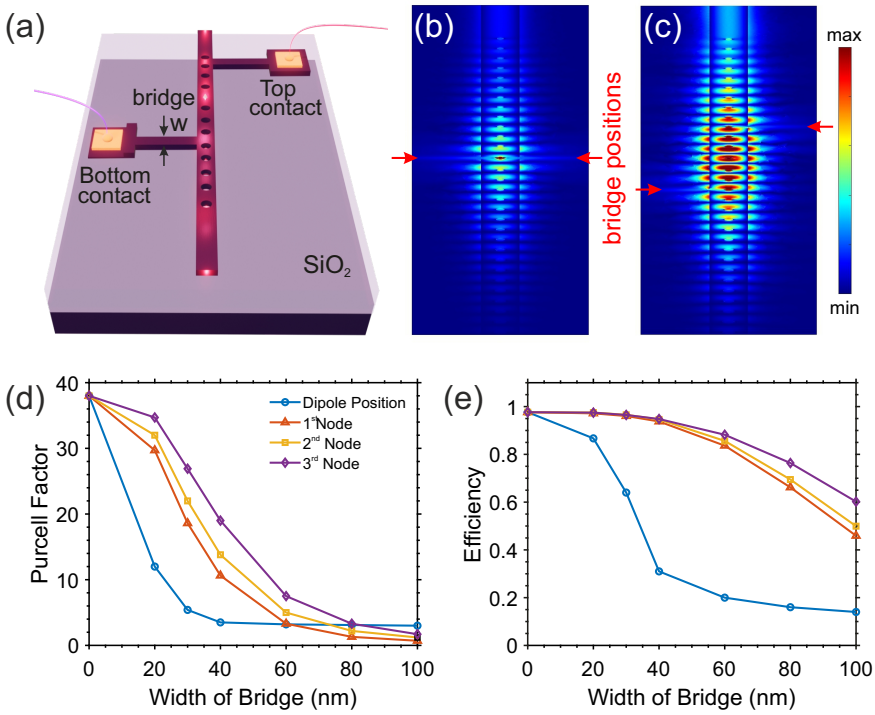

FIG. 9. (a) Sketch of the nanobeam cavity sandwiched by two DBR mirrors. The normalized electric field profile when the bridges are (b) at the dipole position / (c) at the third antinodes (one upward and one downward). (d) Purcell Factor and (e) source efficiency ε as a function of the bridge width for different bridge locations.

to 12 already at bridge width of 20 nm, while ε drops to ≈30%. In contrast, the performance remains rather good (ε >80% at bridge width of 60 nm) when the wings are aligned with the field antinode, where the electric field is weakest. Although Fp does not perform as well as ε, it is still promising to maintain a good Purcell enhancement if we move the wings to further nodes and keep the bridge width lower than 40nm, which is indicated by the overall trend of improvement on Purcell factor in Fig. 9 (d) in the range of x-axis 0∼40. The cost of this idea is the larger voltage applied to tune the QD emission, which restricts the wing from being too far from the cavity.

The main fabrication challenge, as for the hole-CBG, concerns etching the holes defining the Bragg mirror. Our champion design has a minimum hole diameter of 40 nm to control the scattering losses as much as possible. However, this size might be tough to perfectly realize. Indeed, when defining very small features with dry plasma etching (either RIE or ICP), it is important to find a good balance between the chemical reaction of the substrate with reactive radicals (the halogens F or Cl in the case of Al, Ga and As) and the ion bombardment rate. Depending on this, it is possible to have different etch profiles such as faceting, trenching, tapering, undercutting or overcutting. All of these effects would somehow redesign the profile of the holes and relevantly impact their shape due to the small sizes. Consequently, the SPS performance will be damaged. One can consider scaling up the entire geometry to twice the sizes in this work, which could help to reduce the toughness in fabrication. However, larger holes would increase the mode mismatch between the cavity mode and the Bloch modes in the DBRs, resulting in a worse efficiency. The trade-off between design and fabrication needs to be considered.

CONCLUSION AND OUTLOOK

In this Perspective, we considered the implementation of electrical contacts in different cavity-based SPS devices (which are needed for electrical tuning and charge stabilization), and we numerically investigated the impact of different contact geometries on the source performance. In the micropillar device, we studied three contact strategies.

Strategy I: Involving a gold ring attached to the contact

placed on top of the pillar. Our investigation reveals that the Purcell factor and the efficiency could be maintained when the ring-pillar overlap was narrower than approximately ∼1/10 of the diameter of the pillar. Beyond this range, figures of merit suffered as a result of light absorption by the gold as well as complicated scattering interference in the far field.

Strategy II: Incorporating a semitransparent and conductive ITO slab in the micropillar, mechanically supported by BCB. This additional slab introduced an additional phase shift to the system, leading to periodic changes in the spectra as the thickness of the slab increases. Although the absorption of ITO introduces an additional loss in collection efficiency, this strategy showed promising potential to preserve source performance with an appropriate parameter of slab thickness.

Strategy III: Implementing electrical contacts through the bridges attached to the pillar. When connecting the micropillar to four lateral bridges, Purcell factor and efficiency remain almost unaffected for bridge width up to 600 nm (compared to a pillar diameter of 2.2 μm), and then rapidly decrease for larger width due to light penetration into the bridges. Fortunately, the threshold value of 600 nm seems to be feasible in fabrication, making this strategy a standout among other alternatives.

Next, we investigated the fabrication-friendly and broadband nanopost cavity, where we explore two strategies to implement contacts.

Strategy I: Semitransparent and conductive ITO slab Similar to the micropillar device, the ITO strategy was also implemented in nanopost devices, showing similar periodic changes in the resonance of the cavity, leading to modulation of the source efficiency. In contrast to the pillar, the ITO slab is placed much closer to the antinode of the cavity mode in the nanopost device. Therefore, the performance of the device is more sensitive to changes in ITO thickness.

Strategy II: Implementing electrical contacts through a single bridge Introducing a single bridge connected to the nanopost breaks the in-plane symmetry of the entire device. Our simulations showed a substantial difference between the two in-plane polarizations, where the dipole polarized perpendicular to the bridge direction is less affected by the bridge. This approach allowed the device to maintain decent source performance despite the relatively wide bridge compared to the nanopost dimension.

In the context of the bullseye device, we found that the

The third structure under consideration is the bullseye, where the contact interacts with the QD in favor of bridges. The quantities of our interest revealed good tolerance to the bridge width. However, for a more straightforward implementation of the electric contacts without constructing the arms, we preferred the new-type hole-bullseye SPS device, where plenty of space on the mesa can be utilized, and direct interaction between the contact and QD is promised.

Lastly, we discussed the bridge strategy in the on-chip nanobeam cavity. Positioning the bridges next to the quantum dot could be an efficient approach to tuning the emission, but this idea was hampered by significant light leakage into the bridges. Our proposed solution suggests positioning the bridges at the nodes of the fundamental cavity mode to minimize light penetration. This strategy proved effective when the bridge width was narrower than 40 nm, as beyond this threshold, efficiency was still maintained while Purcell enhancement was compromised. Overall, our perspectives offer valuable insights into the feasibility and scalability of tunable single-photon sources.

Acknowledgments The authors acknowledge the European Research Council (ERC-CoG "Unity", grant no.865230) and support from the Independent Research Fund Denmark (Grant DFF-9041-00046B). Y.W. and N.G. acknowledge support from the European Union's Horizon 2020 Research and Innovation Programme under the Marie Skolodowska-Curie Grant Agreement no. 861097. B.M. also acknowledges support from the European Research Council (ERC-StG "TuneTMD", grant no. 101076437), and the Villum Foundation (grant no. VIL53033). S.B. acknowledges support from the EMPIR programme co-financed by the Participating States and by the European Union's Horizon 2020 research and innovation programme (project. 20FUN05 "SEQUME").

Authors contribution Y.W. performed all numerical simulations and data analysis. C.P. contributed to the fabrication concerns and considerations of feasibility. M.J. designed the nanopost cavities. B.M. and N.G. conceived the idea and coordinated the project. L.V. and S.B. co-supervised the project. All authors wrote the paper.

Competing interests The authors declare no competing interests.

Data and materials availability All data is available in the manuscript or the supplementary materials.

* Contributed equally to this work
† bamunk@dtu.dk
‡ ngre@dtu.dk

[1] Wang, J., Sciarrino, F., Laing, A. & Thompson, M. Integrated photonic quantum technologies. Nature Photonics **14** (2019).

[2] Li, M. et al. On-chip path encoded photonic quantum toffoli gate. Photon. Res. **10**, 1533–1542 (2022). URL https://opg.optica.org/prj/abstract.cfm?URI=prj-10-7-1533.

[3] Lukens, J. M. & Lougovski, P. Frequency-encoded photonic qubits for scalable quantum information processing. Optica **4**, 8–16 (2017). URL https://opg.optica.org/optica/abstract.cfm?URI=optica-4-1-8.

[4] Lu, H.-H. et al. A controlled-not gate for frequency-bin qubits. npj Quantum Information **24** (2019).

[5] Chuprina, I. N. & Kalachev, A. A. Generating frequency-bin qubits via spontaneous four-wave mixing in a photonic molecule. Phys. Rev. A **100**, 043843 (2019). URL https://link.aps.org/doi/10.1103/PhysRevA.100.043843.

[6] Nicolas, A. et al. A quantum memory for orbital angular momentum photonic qubits. Nature Photonics **8** (2013).

[7] Erhard, M., Fickler, R., Krenn, M. & Zeilinger, A. Twisted photons: New quantum perspectives in high dimensions. Light: Science and Applications **7** (2017).

[8] Ursin, R. et al. Entanglement-based quantum communication over 144 km. Nature Physics **3**, 481–486 (2007).

[9] Chapman, R. et al. Experimental perfect state transfer of an entangled photonic qubit. Nature Communications **7**, 11339 (2016).

[10] Kwiat, P. G. et al. New high-intensity source of polarization-entangled photon pairs. Phys. Rev. Lett. **75**, 4337–4341 (1995). URL https://link.aps.org/doi/10.1103/PhysRevLett.75.4337.

[11] Diedrich, F. & Walther, H. Nonclassical radiation of a single stored ion. Phys. Rev. Lett. **58**, 203–206 (1987). URL https://link.aps.org/doi/10.1103/PhysRevLett.58.203.

[12] Zhai, L. et al. Low-noise GaAs quantum dots for quantum photonics. Nature Communications **11** (2020).

[13] Tonndorf, P. et al. Single-photon emission from localized excitons in an atomically thin semiconductor. Optica **2**, 347–352 (2015). URL https://opg.optica.org/optica/abstract.cfm?URI=optica-2-4-347.

[14] Michler, P. et al. A quantum dot single-photon turnstile device. Science **290**, 2282–2285 (2000). URL https://www.science.org/doi/abs/10.1126/science.290.5500.2282. https://www.science.org/doi/pdf/10.1126/science.290.5500.2282.

[15] O'Brien, J. L. Optical quantum computing. Science **318**, 1567–1570 (2007). URL https://www.science.org/doi/abs/10.1126/science.1142892. https://www.science.org/doi/pdf/10.1126/science.1142892.

[16] Dusanowski, L., Kwon, S.-H., Schneider, C. & Höfling, S. Near-unity indistinguishability single photon source for large-scale integrated quantum optics. Phys. Rev. Lett. **122**, 173602 (2019). URL https://link.aps.org/doi/10.1103/PhysRevLett.122.173602.

[17] Wang, H. et al. Toward scalable boson sampling with photon loss. Phys. Rev. Lett. **120**, 230502 (2018). URL https://link.aps.org/doi/10.1103/PhysRevLett.120.230502.

[18] Devitt, S. J., Munro, W. J. & Nemoto, K. Quantum error correction for beginners. Reports on Progress in Physics **76**, 076001 (2013).

[19] Madsen, K. H. et al. Efficient out-coupling of high-purity single photons from a coherent quantum dot in a photonic-crystal cavity. Phys. Rev. B **90**, 155303 (2014). URL https://link.aps.org/doi/10.1103/PhysRevB.90.155303.

[20] Ding, X. et al. On-demand single photons with high extraction efficiency and near-unity indistinguishability from a resonantly driven quantum dot in a micropillar. Phys. Rev. Lett. **116**, 020401 (2016). URL https://link.aps.org/doi/10.1103/PhysRevLett.116.020401.

[21] Bleuse, J. et al. Inhibition, enhancement, and control of spontaneous emission in photonic nanowires. Physical Review Letters **106**, 103601 (2011).

[22] Sapienza, L., Davanco, M., Badolato, A. & Srinivasan, K. Nanoscale optical positioning of single quantum dots for bright and pure single-photon emission. Nature communications **6** (2015).

[23] Wang, B.-Y., Denning, E. V., Gür, U. M., Lu, C.-Y. & Gregersen, N. Micropillar single-photon source design for simultaneous near-unity efficiency and indistinguishability. Physical Review B **102**, 125301 (2020).

[24] Tomm, N. et al. A bright and fast source of coherent single photons. Nature Nanotechnology **16**, 399–403 (2021).

[25] Spagnolo, N. et al. Experimental validation of photonic boson sampling. Nature Photonics **8**, 615–620 (2014).

[26] Diamanti, E., Lo, H.-K., Qi, B. & Yuan, Z. Practical challenges in quantum key distribution. npj Quantum Information **2**, 1–12 (2016).

[27] Lenzini, F. et al. Active demultiplexing of single photons from a solid-state source. Laser &amp Photonics Reviews **11**, 1600297 (2017). URL https://doi.org/10.1002%2Flpor.201600297.

[28] Münzberg, J. et al. Fast and efficient demultiplexing of single photons from a quantum dot with resonantly enhanced electro-optic modulators. APL Photonics **7**, 070802 (2022). URL https://doi.org/10.1063%2F5.0091867.

[29] Pont, M. et al. Quantifying n-photon indistinguishability with a cyclic integrated interferometer. Phys. Rev. X **12**, 031033 (2022). URL https://link.aps.org/doi/10.1103/PhysRevX.12.031033.

[30] Weber, J. et al. Two-photon interference in the telecom c-band after frequency conversion of photons from remote quantum emitters. Nature Nanotechnology **14** (2019).

[31] You, X. et al. Quantum interference between independent solid-state single-photon sources separated by 300 km fiber (2021).

[32] Pont, M. et al. Two-photon interference with bright remote quantum dot sources. In Quantum Information and Measurement VI 2021, Tu2B.4 (Optica Publishing Group, 2021). URL https://opg.optica.org/abstract.cfm?URI=QIM-2021-Tu2B.4.

[33] Zhai, L. et al. Quantum interference of identical photons from remote gaas quantum dots. Nature Nanotechnology **17**, 1–5 (2022).

[34] Papon, C. et al. Independent operation of two waveguide-integrated single-photon sources (2022). URL http://arxiv.org/abs/2210.09826.

[35] Kolodynski, J. J. et al. Device-independent quantum

key distribution with single-photon sources. Quantum **4** (2018).

[36] Wolters, J. et al. Simple atomic quantum memory suitable for semiconductor quantum dot single photons. Phys. Rev. Lett. **119**, 060502 (2017). URL https://link.aps.org/doi/10.1103/PhysRevLett.119.060502.

[37] Patel, R. et al. Two-photon interference of the emission from electrically tunable remote quantum dots. Nature Photonics **4** (2010).

[38] Giesz, V. et al. Cavity-enhanced two-photon interference using remote quantum dot sources. Phys. Rev. B **92**, 161302 (2015). URL https://link.aps.org/doi/10.1103/PhysRevB.92.161302.

[39] Thoma, A. et al. Two-photon interference from remote deterministic quantum dot microlenses. Applied Physics Letters **110**, 011104 (2017). URL https://doi.org/10.1063%2F1.4973504.

[40] Gazzano, O. et al. Bright solid-state sources of indistinguishable single photons. Nature communications **4**, 1425 (2013). URL https://doi.org/10.1038/ncomms2434.

[41] Zopf, M. et al. Frequency feedback for two-photon interference from separate quantum dots. Phys. Rev. B **98**, 161302 (2018). URL https://link.aps.org/doi/10.1103/PhysRevB.98.161302.

[42] He, Y.-M. et al. On-demand semiconductor single-photon source with near-unity indistinguishability. Nature nanotechnology **8** (2013).

[43] Huber, T., Predojević, A., Föger, D., Solomon, G. & Weihs, G. Optimal excitation conditions for indistinguishable photons from quantum dots. New Journal of Physics **17**, 123025 (2015). URL https://dx.doi.org/10.1088/1367-2630/17/12/123025.

[44] Liu, J. et al. Cryogenic photoluminescence imaging system for nanoscale positioning of single quantum emitters. Review of Scientific Instruments **88**, 023116 (2017). URL https://doi.org/10.1063/1.4976578. https://doi.org/10.1063/1.4976578.

[45] Sapienza, L. et al. Combined atomic force microscopy and photoluminescence imaging to select single InAs/GaAs quantum dots for quantum photonic devices. Scientific Reports **7** (2017). URL https://doi.org/10.1038%2Fs41598-017-06566-5.

[46] Hao, Q., Lv, H., Ma, H., Tang, X. & Chen, M. Development of self-assembly methods on quantum dots. Materials **16** (2023). URL https://www.mdpi.com/1996-1944/16/3/1317.

[47] Klimov, V. I. Multicarrier interactions in semiconductor nanocrystals in relation to the phenomena of auger recombination and carrier multiplication. Annual Review of Condensed Matter Physics **5**, 285–316 (2014). URL https://doi.org/10.1146/annurev-conmatphys-031113-133900. https://doi.org/10.1146/annurev-conmatphys-031113-133900.

[48] Riel, B. J. An introduction to self-assembled quantum dots. American Journal of Physics **76**, 750–757 (2008). URL https://doi.org/10.1119/1.2907856. https://doi.org/10.1119/1.2907856.

[49] Gevaux, D. G. et al. Enhancement and suppression of spontaneous emission by temperature tuning inas quantum dots to photonic crystal cavities. Applied Physics Letters **88**, 131101 (2006). URL https://doi.org/10.1063/1.2189747. https://doi.org/10.1063/1.2189747.

[50] Faraon, A. & Vučković, J. Local temperature control of photonic crystal devices via micron-scale electrical heaters. Applied Physics Letters **95**, 043102 (2009). URL https://doi.org/10.1063/1.3189081. https://doi.org/10.1063/1.3189081.

[51] Kim, H., Shen, T. C., Sridharan, D., Solomon, G. S. & Waks, E. Magnetic field tuning of a quantum dot strongly coupled to a photonic crystal cavity. Applied Physics Letters **98**, 091102 (2011). URL https://doi.org/10.1063/1.3562344. https://doi.org/10.1063/1.3562344.

[52] Beetz, J., Braun, T., Schneider, C., Höfling, S. & Kamp, M. Anisotropic strain-tuning of quantum dots inside a photonic crystal cavity. Semiconductor Science and Technology **28**, 122002 (2013). URL https://dx.doi.org/10.1088/0268-1242/28/12/122002.

[53] Fry, P. W. et al. Inverted electron-hole alignment in inas-gaas self-assembled quantum dots. Phys. Rev. Lett. **84**, 733–736 (2000). URL https://link.aps.org/doi/10.1103/PhysRevLett.84.733.

[54] Alén, B., Bickel, F., Karrai, K., Warburton, R. J. & Petroff, P. M. Stark-shift modulation absorption spectroscopy of single quantum dots. Applied Physics Letters **83**, 2235–2237 (2003). URL https://doi.org/10.1063/1.1609243. https://doi.org/10.1063/1.1609243.

[55] Laucht, A. et al. Electrical control of spontaneous emission and strong coupling for a single quantum dot. New Journal of Physics **11**, 023034 (2009). URL https://dx.doi.org/10.1088/1367-2630/11/2/023034.

[56] Thon, S. M. et al. Independent electrical tuning of separated quantum dots in coupled photonic crystal cavities. Applied Physics Letters **99**, 161102 (2011). URL https://doi.org/10.1063/1.3651491. https://doi.org/10.1063/1.3651491.

[57] Bennett, A. J. et al. Giant stark effect in the emission of single semiconductor quantum dots. Applied Physics Letters **97**, 031104 (2010). URL https://doi.org/10.1063/1.3460912. https://doi.org/10.1063/1.3460912.

[58] Trotta, R., Zallo, E., Magerl, E., Schmidt, O. G. & Rastelli, A. Independent control of exciton and biexciton energies in single quantum dots via electroelastic fields. Phys. Rev. B **88**, 155312 (2013). URL https://link.aps.org/doi/10.1103/PhysRevB.88.155312.

[59] Aberl, J. et al. Inversion of the exciton built-in dipole moment in in(ga)as quantum dots via nonlinear piezoelectric effect. Phys. Rev. B **96**, 045414 (2017). URL https://link.aps.org/doi/10.1103/PhysRevB.96.045414.

[60] Warburton, R. et al. Optical emission from a charge-tunable quantum ring. Nature **405**, 926–929 (2000).

[61] Kuhlmann, A. V. et al. Transform-limited single photons from a single quantum dot. Nature Communications **6** (2015). URL https://doi.org/10.1038%2Fncomms9204.

[62] Claudon, J. et al. A highly efficient single-photon source based on a quantum dot in a photonic wire. Nature Photonics **4** (2010).

[63] Chen, Y., Nielsen, T. R., Gregersen, N., Lodahl, P. & Mørk, J. Finite-element modeling of spontaneous emission of a quantum emitter at nanoscale proximity to plasmonic waveguides. Phys. Rev. B **81**, 125431 (2010). URL https://link.aps.org/doi/10.1103/PhysRevB.81.125431.

[64] Ji, S., Tajiri, T., Kiyama, H., Oiwa, A. & Iwamoto, S. Design of bull's-eye optical cavity toward efficient quantum media conversion using gate-defined quantum dot. Japanese Journal of Applied Physics **60** (2021). Publisher Copyright: © 2021 The Japan Society of Applied Physics.

[65] Blokhin, S. A. et al. Design optimization for bright electrically-driven quantum dot single-photon sources emitting in telecom o-band. Optics Express **29**, 6582 (2021).

[66] Gregersen, N., Nielsen, T. R., Mørk, J., Claudon, J. & Gérard, J.-M. Designs for high-efficiency electrically pumped photonic nanowire single-photon sources. Opt. Express **18**, 21204–21218 (2010). URL https://opg.optica.org/oe/abstract.cfm?URI=oe-18-20-21204.

[67] Gregersen, N., Kaer, P. & Mørk, J. Modeling and design of high-efficiency single-photon sources. IEEE Journal of Selected Topics in Quantum Electronics **19**, 1–16 (2013).

[68] Böckler, C. et al. Electrically driven high- q quantum dot-micropillar cavities. Applied Physics Letters **92** (2008).

[69] Kistner, C. et al. Demonstration of strong coupling via electro-optical tuning in high-quality qd-micropillar systems. Opt. Express **16**, 15006–15012 (2008). URL https://opg.optica.org/oe/abstract.cfm?URI=oe-16-19-15006.

[70] Heindel, T. et al. Electrically driven quantum dot-micropillar single photon source with 34% overall efficiency. Applied Physics Letters **96** (2010).

[71] Somaschi, N. et al. Near-optimal single-photon sources in the solid state. Nature Photonics **10**, 340–345 (2016).

[72] Soleimani, E. et al. Structural properties of indium tin oxide thin films prepared for application in solar cells. Materials Research Bulletin - MATER RES BULL **40**, 1303–1307 (2005).

[73] Schneider, C. et al. Microcavity enhanced single photon emission from an electrically driven site-controlled quantum dot. Applied Physics Letters **100** (2012).

[74] Nowak, A. K. et al. Deterministic and electrically tunable bright single-photon source. Nature Communications **5** (2014).

[75] Hilaire, P. et al. Deterministic assembly of a charged-quantum-dot–micropillar cavity device. Phys. Rev. B **102**, 195402 (2020). URL https://link.aps.org/doi/10.1103/PhysRevB.102.195402.

[76] Strauf, S. et al. High-frequency single-photon source with polarization control. Nature Photonics **1**, 704–708 (2007).

[77] Schall, J. et al. Bright electrically controllable quantum-dot-molecule devices fabricated by in situ electron-beam lithography. Advanced Quantum Technologies **4** (2021).

[78] Barbiero, A. et al. Design study for an efficient semiconductor quantum light source operating in the telecom c-band based on an electrically-driven circular bragg grating. Optics Express **30**, 10919 (2022).

[79] Jeon, W. B. et al. Plug-and-play single-photon devices with efficient fiber-quantum dot interface. Advanced Quantum Technologies **5**, 2200022 (2022). URL https://onlinelibrary.wiley.com/doi/abs/10.1002/qute.202200022. https://onlinelibrary.wiley.com/doi/pdf/10.1002/qute.202200022.

[80] Buchinger, Q., Betzold, S., Höfling, S. & Huber-Loyola, T. Optical properties of circular bragg gratings with labyrinth geometry to enable electrical contacts. Applied Physics Letters **122** (2023).

[81] Kotal, S. et al. A nanowire optical nanocavity for broadband enhancement of spontaneous emission. Applied Physics Letters **118**, 194002 (2021).

[82] Jacobsen, M. A. et al. Performance of the nanopost single-photon source: beyond the single-mode model (2023). 2301.02556.

[83] Munsch, M. et al. Dielectric gaas antenna ensuring an efficient broadband coupling between an inas quantum dot and a gaussian optical beam. Phys. Rev. Lett. **110**, 177402 (2013). URL https://link.aps.org/doi/10.1103/PhysRevLett.110.177402.

[84] Claudon, J., Gregersen, N., Lalanne, P. & Gérard, J.-M. Harnessing light with photonic nanowires: Fundamentals and applications to quantum optics. ChemPhysChem **14**, 2393–2402 (2013). URL https://chemistry-europe.onlinelibrary.wiley.com/doi/abs/10.1002/cphc.201300033. https://chemistry-europe.onlinelibrary.wiley.com/doi/pdf/10.1002/cphc.201300033.

[85] Gregersen, N., McCutcheon, D. P., Mørk, J., Gérard, J.-M. & Claudon, J. A broadband tapered nanocavity for efficient nonclassical light emission. Optics Express **24**, 20904–20924 (2016).

[86] Ohta, R. et al. Strong coupling between a photonic crystal nanobeam cavity and a single quantum dot. Applied Physics Letters **98** (2011). URL https://doi.org/10.1063/1.3579535. 173104, https://pubs.aip.org/aip/apl/article-pdf/doi/10.1063/1.3579535/14448661/173104_1_online.pdf.

[87] Arcari, M. et al. Near-unity coupling efficiency of a quantum emitter to a photonic crystal waveguide. Physical Review Letters **113**, 093603 (2014).

[88] Song, B.-S., Noda, S., Asano, T. & Akahane, Y. Ultra-high-q photonic double-heterostructure nanocavity. Nature Materials **4**, 207–210 (2005).

[89] Ota, Y., Iwamoto, S., Kumagai, N. & Arakawa, Y. Spontaneous two-photon emission from a single quantum dot. Phys. Rev. Lett. **107**, 233602 (2011). URL https://link.aps.org/doi/10.1103/PhysRevLett.107.233602.

[90] Coimbatore Balram, K., Davanço, M., Song, J. & Srinivasan, K. Coherent coupling between radio frequency, optical, and acoustic waves in piezo-optomechanical circuits. Nature Photonics **10** (2015).

[91] Bentham, C. et al. Single-photon electroluminescence for on-chip quantum networks. Applied Physics Letters **109** (2016). URL https://doi.org/10.1063/1.4965295. 161101, https://pubs.aip.org/aip/apl/article-pdf/doi/10.1063/1.4965295/13326589/161101_1_online.pdf.

[92] Kiršanskė, G. et al. Indistinguishable and efficient single photons from a quantum dot in a planar nanobeam waveguide. Phys. Rev. B **96**, 165306 (2017). URL https://link.aps.org/doi/10.1103/PhysRevB.96.165306.

[93] Midolo, L. et al. Spontaneous emission control of single quantum dots by electromechanical tuning of a photonic crystal cavity. Applied Physics Letters **101** (2012).

[94] Wang, Y., Vannucci, L., Burger, S. & Gregersen, N. Near-unity efficiency in ridge waveguide-based, on-chip single-photon sources. Materials for Quantum Technology **2**, 045004 (2022).

Bibliography

[1] C. Couteau, S. Barz, T. Durt, T. Gerrits, J. Huwer, R. Prevedel, J. Rarity, A. Shields, and G. Weihs, "Applications of single photons to quantum communication and computing," *Nature Reviews Physics*, pp. 1–13, 2023.

[2] Y. Arakawa and M. J. Holmes, "Progress in quantum-dot single photon sources for quantum information technologies: A broad spectrum overview," *Applied Physics Reviews*, vol. 7, no. 2, 2020.

[3] M. Varnava, D. E. Browne, and T. Rudolph, "How good must single photon sources and detectors be for efficient linear optical quantum computation?," *Physical review letters*, vol. 100, no. 6, p. 060502, 2008.

[4] P. I. Sund, E. Lomonte, S. Paesani, Y. Wang, J. Carolan, N. Bart, A. D. Wieck, A. Ludwig, L. Midolo, W. H. Pernice, *et al.*, "High-speed thin-film lithium niobate quantum processor driven by a solid-state quantum emitter," *Science Advances*, vol. 9, no. 19, p. eadg7268, 2023.

[5] M. Benyoucef and A. Musiał, "Telecom wavelengths inp-based quantum dots for quantum communication," *Photonic Quantum Technologies: Science and Applications*, vol. 2, pp. 463–507, 2023.

[6] L. Zhou, B.-W. Xu, W. Zhong, and Y.-B. Sheng, "Device-independent quantum secure direct communication with single-photon sources," *Physical Review Applied*, vol. 19, no. 1, p. 014036, 2023.

[7] C.-Y. Lu and J.-W. Pan, "Quantum-dot single-photon sources for the quantum internet," *Nature Nanotechnology*, vol. 16, no. 12, pp. 1294–1296, 2021.

[8] M. Von Helversen, J. Böhm, M. Schmidt, M. Gschrey, J.-H. Schulze, A. Strittmatter, S. Rodt, J. Beyer, T. Heindel, and S. Reitzenstein,

"Quantum metrology of solid-state single-photon sources using photon-number-resolving detectors," *New Journal of Physics*, vol. 21, no. 3, p. 035007, 2019.

[9] K. R. Motes, R. L. Mann, J. P. Olson, N. M. Studer, E. A. Bergeron, A. Gilchrist, J. P. Dowling, D. W. Berry, and P. P. Rohde, "Efficient recycling strategies for preparing large fock states from single-photon sources: Applications to quantum metrology," *Physical Review A*, vol. 94, no. 1, p. 012344, 2016.

[10] Y. Karli, D. A. Vajner, F. Kappe, P. C. Hagen, L. M. Hansen, R. Schwarz, T. K. Bracht, C. Schimpf, S. F. C. da Silva, P. Walther, *et al.*, "Controlling the photon number coherence of solid-state quantum light sources for quantum cryptography," *arXiv preprint arXiv:2305.20017*, 2023.

[11] T. Kupko, M. von Helversen, L. Rickert, J.-H. Schulze, A. Strittmatter, M. Gschrey, S. Rodt, S. Reitzenstein, and T. Heindel, "Tools for the performance optimization of single-photon quantum key distribution," *NJP Quantum Information*, vol. 6, no. 1, pp. 1–8, 2020.

[12] M. Schmidt, M. V. Helversen, S. Fischbach, A. Kaganskiy, R. Schmidt, A. Schliwa, T. Heindel, S. Rodt, and S. Reitzenstein, "Deterministically fabricated spectrally-tunable quantum dot based single-photon source," *Optical Materials Express*, vol. 10, no. 1, pp. 76–87, 2020.

[13] B. Lounis and M. Orrit, "Single-photon sources," *Reports on Progress in Physics*, vol. 68, no. 5, p. 1129, 2005.

[14] T. Darras, B. E. Asenbeck, G. Guccione, A. Cavaillès, H. Le Jeannic, and J. Laurat, "A quantum-bit encoding converter," *Nature Photonics*, vol. 17, no. 2, pp. 165–170, 2023.

[15] Y. Chatterjee, E. Bourreau, and M. J. Rančić, "Solving various np-hard problems using exponentially fewer qubits on a quantum computer," *arXiv preprint arXiv:2301.06978*, 2023.

[16] T. B. Lehmann, *Single-photon Technologies Based on Quantum-dots in Photonic Crystals: From Sources to Application*. PhD thesis, University of Copenhagen, Faculty of Science, Niels Bohr Institute, 2016.

[17] C. You, A. C. Nellikka, I. De Leon, and O. S. Magaña-Loaiza, "Multiparticle quantum plasmonics," *Nanophotonics*, vol. 9, no. 6, pp. 1243–1269, 2020.

[18] A. McMillan, L. Labonté, A. Clark, B. Bell, O. Alibart, A. Martin, W. Wadsworth, S. Tanzilli, and J. Rarity, "Two-photon interference between disparate sources for quantum networking," *Scientific reports*, vol. 3, no. 1, p. 2032, 2013.

[19] L. Dusanowski, S.-H. Kwon, C. Schneider, and S. Höfling, "Near-unity indistinguishability single photon source for large-scale integrated quantum optics," *Phys. Rev. Lett.*, vol. 122, p. 173602, May 2019.

[20] S. Buckley, K. Rivoire, and J. Vučković, "Engineered quantum dot single-photon sources," *Reports on Progress in Physics*, vol. 75, no. 12, p. 126503, 2012.

[21] R. Li, F. Liu, and Q. Lu, "Quantum light source based on semiconductor quantum dots: A review," in *Photonics*, vol. 10, p. 639, MDPI, 2023.

[22] Y.-M. He, Y. He, Y.-J. Wei, D. Wu, M. Atatüre, C. Schneider, S. Höfling, M. Kamp, C.-Y. Lu, and J.-W. Pan, "On-demand semiconductor single-photon source with near-unity indistinguishability," *Nature nanotechnology*, vol. 8, no. 3, pp. 213–217, 2013.

[23] H. Wang, Y.-M. He, T.-H. Chung, H. Hu, Y. Yu, S. Chen, X. Ding, M.-C. Chen, J. Qin, X. Yang, R.-Z. Liu, Z.-C. Duan, J.-P. Li, S. Gerhardt, K. Winkler, J. Jurkat, L.-J. Wang, N. Gregersen, Y.-H. Huo, Q. Dai, S. Yu, S. Höfling, C.-Y. Lu, and J.-W. Pan, "Towards optimal single-photon sources from polarized microcavities," *Nature Photonics*, vol. 13, no. 11, pp. 770–775, 2019.

[24] O. Gazzano, S. Michaelis de Vasconcellos, C. Arnold, A. Nowak, E. Galopin, I. Sagnes, L. Lanco, A. Lemaître, and P. Senellart, "Bright solid-state sources of indistinguishable single photons," *Nature communications*, vol. 4, no. 1, p. 1425, 2013.

[25] X. Ding, Y. He, Z.-C. Duan, N. Gregersen, M.-C. Chen, S. Unsleber, S. Maier, C. Schneider, M. Kamp, S. Höfling, C.-Y. Lu, and J.-W. Pan, "On-demand single photons with high extraction efficiency and near-unity indistinguishability from a resonantly driven quantum dot in a micropillar," *Physical Review Letters*, vol. 116, no. 2, p. 020401, 2016.

[26] N. Somaschi, V. Giesz, L. De Santis, J. Loredo, M. P. Almeida, G. Hornecker, S. L. Portalupi, T. Grange, C. Anton, J. Demory, *et al.*, "Near-optimal single-photon sources in the solid state," *Nature Photonics*, vol. 10, no. 5, pp. 340–345, 2016.

[27] N. Tomm, A. Javadi, N. O. Antoniadis, D. Najer, M. C. Löbl, A. R. Korsch, R. Schott, S. R. Valentin, A. D. Wieck, A. Ludwig, *et al.*, "A bright and fast source of coherent single photons," *Nature Nanotechnology*, vol. 16, no. 4, pp. 399–403, 2021.

[28] K. Parto, S. I. Azzam, K. Banerjee, and G. Moody, "Defect and strain engineering of monolayer wse2 enables site-controlled single-photon emission up to 150 k," *Nature communications*, vol. 12, no. 1, p. 3585, 2021.

[29] O. Iff, D. Tedeschi, J. Martín-Sánchez, M. Moczała-Dusanowska, S. Tongay, K. Yumigeta, J. Taboada-Gutiérrez, M. Savaresi, A. Rastelli, P. Alonso-González, *et al.*, "Strain-tunable single photon sources in wse2 monolayers," *Nano Letters*, vol. 19, no. 10, pp. 6931–6936, 2019.

[30] O. Iff, Q. Buchinger, M. Moczała-Dusanowska, M. Kamp, S. Betzold, M. Davanco, K. Srinivasan, S. Tongay, C. Antón-Solanas, S. Hofling, *et al.*, "Purcell-enhanced single photon source based on a deterministically placed wse2 monolayer quantum dot in a circular bragg grating cavity," *Nano letters*, vol. 21, no. 11, pp. 4715–4720, 2021.

[31] B. Rodiek, M. Lopez, H. Hofer, G. Porrovecchio, M. Smid, X.-L. Chu, S. Gotzinger, V. Sandoghdar, S. Lindner, C. Becher, *et al.*, "Experimental realization of an absolute single-photon source based on a single nitrogen vacancy center in a nanodiamond," *Optica*, vol. 4, no. 1, pp. 71–76, 2017.

[32] N. Mizuochi, T. Makino, H. Kato, D. Takeuchi, M. Ogura, H. Okushi, M. Nothaft, P. Neumann, A. Gali, F. Jelezko, *et al.*, "Electrically driven single-photon source at room temperature in diamond," *Nature photonics*, vol. 6, no. 5, pp. 299–303, 2012.

[33] N. Kurochkin, S. Savinov, D. Bi, V. Sychev, S. Eliseev, and A. Gritsienko, "Characterization of milled high-pressure high-temperature nv-center nanodiamonds for single-photon source applications," *Journal of Russian Laser Research*, vol. 42, pp. 713–720, 2021.

[34] G.-C. Shan, Z.-Q. Yin, C. H. Shek, and W. Huang, "Single photon sources with single semiconductor quantum dots," *Frontiers of Physics*, vol. 9, pp. 170–193, 2014.

[35] J. Jurkat, S. Klembt, M. De Gregorio, M. Meinecke, Q. Buchinger, T. H. Harder, J. Beierlein, O. A. Egorov, M. Emmerling, C. Krause, *et al.*, "Single-photon source in a topological cavity," *Nano Letters*, vol. 23, no. 3, pp. 820–826, 2023.

[36] V. Remesh, R. G. Krämer, R. Schwarz, F. Kappe, Y. Karli, M. P. Siems, T. K. Bracht, S. F. C. da Silva, A. Rastelli, D. E. Reiter, *et al.*, "Compact chirped fiber bragg gratings for single-photon generation from quantum dots," *arXiv preprint arXiv:2306.11635*, 2023.

[37] X. Li, S. Liu, Y. Wei, J. Ma, C. Song, Y. Yu, R. Su, W. Geng, H. Ni, H. Liu, *et al.*, "Bright semiconductor single-photon sources pumped by heterogeneously integrated micropillar lasers with electrical injections," *Light: Science & Applications*, vol. 12, no. 1, p. 65, 2023.

[38] P. Michler, *Quantum dots for quantum information technologies*, vol. 237. Springer, 2017.

[39] L. Zhai, G. Nguyen, C. Spinnler, J. Ritzmann, M. Löbl, A. Wieck, A. Ludwig, A. Javadi, and R. Warburton, "Quantum interference of identical photons from remote gaas quantum dots," *Nature Nanotechnology*, vol. 17, pp. 1–5, 08 2022.

[40] N. Gregersen, D. P. McCutcheon, and J. Mørk, "Single-photon sources," *Handbook of Optoelectronic Device Modeling and Simulation*, pp. 585–608, 2017.

[41] G. Solomon, J. Trezza, and J. Harris Jr, "Substrate temperature and monolayer coverage effects on epitaxial ordering of inas and ingaas islands on gaas," *Applied physics letters*, vol. 66, no. 8, pp. 991–993, 1995.

[42] J. Marquez, L. Geelhaar, and K. Jacobi, "Atomically resolved structure of inas quantum dots," *Applied Physics Letters*, vol. 78, no. 16, pp. 2309–2311, 2001.

[43] C. Santori, M. Pelton, G. Solomon, Y. Dale, and Y. Yamamoto, "Triggered single photons from a quantum dot," *Physical Review Letters*, vol. 86, no. 8, p. 1502, 2001.

[44] C. Gustin and S. Hughes, "Efficient pulse-excitation techniques for single photon sources from quantum dots in optical cavities," *Advanced Quantum Technologies*, vol. 3, no. 2, p. 1900073, 2020.

[45] M. Cosacchi, F. Ungar, M. Cygorek, A. Vagov, and V. M. Axt, "Emission-frequency separated high quality single-photon sources enabled by phonons," *Physical Review Letters*, vol. 123, no. 1, p. 017403, 2019.

[46] S. L. Portalupi, G. Hornecker, V. Giesz, T. Grange, A. Lemaître, J. Demory, I. Sagnes, N. D. Lanzillotti-Kimura, L. Lanco, A. Auffèves, *et al.*, "Bright phonon-tuned single-photon source," *Nano letters*, vol. 15, no. 10, pp. 6290–6294, 2015.

[47] N. Srocka, P. Mrowiński, J. Große, M. Von Helversen, T. Heindel, S. Rodt, and S. Reitzenstein, "Deterministically fabricated quantum dot single-photon source emitting indistinguishable photons in the telecom o-band," *Applied Physics Letters*, vol. 116, no. 23, 2020.

[48] P. Holewa, A. Maryński, A. Musiał, T. Heuser, N. Srocka, D. Quandt, A. Strittmatter, S. Rodt, J. Misiewicz, S. Reitzenstein, *et al.*, "Triggered high-purity telecom-wavelength single-photon generation from p-shell-driven ingaas/gaas quantum dot," *Optics express*, vol. 25, no. 25, pp. 31122–31129, 2017.

[49] T. Heindel, S. Rodt, and S. Reitzenstein, "Single-photon sources based on deterministic quantum-dot microlenses," in *Quantum Dots for Quantum Information Technologies*, pp. 199–232, Springer, 2017.

[50] A. J. Brash, J. Iles-Smith, C. L. Phillips, D. P. McCutcheon, J. O'Hara, E. Clarke, B. Royall, L. R. Wilson, J. Mørk, M. S. Skolnick, *et al.*, "Light scattering from solid-state quantum emitters: beyond the atomic picture," *Physical Review Letters*, vol. 123, no. 16, p. 167403, 2019.

[51] P. Borri, W. Langbein, S. Schneider, U. Woggon, R. L. Sellin, D. Ouyang, and D. Bimberg, "Ultralong dephasing time in ingaas quantum dots," *Physical Review Letters*, vol. 87, no. 15, p. 157401, 2001.

[52] E. A. Muljarov and R. Zimmermann, "Dephasing in quantum dots: Quadratic coupling to acoustic phonons," *Physical review letters*, vol. 93, no. 23, p. 237401, 2004.

[53] P. Kaer, N. Gregersen, and J. Mork, "The role of phonon scattering in the indistinguishability of photons emitted from semiconductor cavity qed systems," *New Journal of Physics*, vol. 15, no. 3, p. 035027, 2013.

[54] B. Urbaszek, X. Marie, T. Amand, O. Krebs, P. Voisin, P. Maletinsky, A. Högele, and A. Imamoglu, "Nuclear spin physics in quantum dots: An optical investigation," *Reviews of Modern Physics*, vol. 85, no. 1, p. 79, 2013.

[55] A. V. Kuhlmann, J. Houel, A. Ludwig, L. Greuter, D. Reuter, A. D. Wieck, M. Poggio, and R. J. Warburton, "Charge noise and spin noise in a semiconductor quantum device," *Nature Physics*, vol. 9, no. 9, pp. 570–575, 2013.

[56] F. Albert, K. Sivalertporn, J. Kasprzak, M. Strauss, C. Schneider, S. Höfling, M. Kamp, A. Forchel, S. Reitzenstein, E. A. Muljarov, *et al.*, "Microcavity controlled coupling of excitonic qubits," *Nature communications*, vol. 4, no. 1, p. 1747, 2013.

[57] U. M. Gür, M. Mattes, S. Arslanagić, and N. Gregersen, "Elliptical micropillar cavity design for highly efficient polarized emission of single photons," *Applied Physics Letters*, vol. 118, no. 6, p. 061101, 2021.

[58] J. Claudon, J. Bleuse, N. Malik, M. Bazin, P. Jaffrennou, N. Gregersen, C. Sauvan, P. Lalanne, and J.-M. Gérard, "A highly efficient single-photon source based on a quantum dot in a photonic wire," *Nature Photonics*, vol. 4, 03 2010.

[59] B. Gaál, M. A. Jacobsen, L. Vannucci, J. Claudon, J.-M. Gérard, and N. Gregersen, "Near-unity efficiency and photon indistinguishability for the "hourglass" single-photon source using suppression of the background emission," *Applied Physics Letters*, vol. 121, no. 17, 2022.

[60] S. Kolatschek, C. Nawrath, S. Bauer, J. Huang, J. Fischer, R. Sittig, M. Jetter, S. L. Portalupi, and P. Michler, "Bright purcell enhanced single-photon source in the telecom o-band based on a quantum dot in a circular bragg grating," *Nano letters*, vol. 21, no. 18, pp. 7740–7745, 2021.

[61] N. Gregersen, P. Kaer, and J. Mørk, "Modeling and design of high-efficiency single-photon sources," *IEEE Journal of Selected Topics in Quantum Electronics*, vol. 19, no. 5, pp. 1–16, 2013.

[62] J. Bleuse, J. Claudon, M. Creasey, N. S. Malik, J.-M. Gérard, I. Maksymov, J.-P. Hugonin, and P. Lalanne, "Inhibition, enhancement, and control of spontaneous emission in photonic nanowires," *Physical Review Letters*, vol. 106, no. 10, p. 103601, 2011.

[63] J. C. Drawer, V. N. Mitryakhin, H. Shan, S. Stephan, M. Gittinger, L. Lackner, B. Han, G. Leibeling, F. Eilenberger, R. Banerjee, *et al.*, "Ultra-bright single photon source based on an atomically thin material," *arXiv preprint arXiv:2302.06340*, 2023.

[64] W. B. Jeon, J. S. Moon, K.-Y. Kim, Y.-H. Ko, C. J. K. Richardson, E. Waks, and J.-H. Kim, "Plug-and-play single-photon devices with efficient fiber-quantum dot interface," *Advanced Quantum Technologies*, vol. 5, no. 10, p. 2200022, 2022.

[65] R. Uppu, F. T. Pedersen, Y. Wang, C. T. Olesen, C. Papon, X. Zhou, L. Midolo, S. Scholz, A. D. Wieck, A. Ludwig, and P. Lodahl, "Scalable integrated single-photon source," *Science Advances*, vol. 6, no. 50, p. eabc8268, 2020.

[66] S. Hepp, F. Hornung, S. Bauer, E. Hesselmeier, X. Yuan, M. Jetter, S. L. Portalupi, A. Rastelli, and P. Michler, "Purcell-enhanced single-photon emission from a strain-tunable quantum dot in a cavity-waveguide device," *Applied Physics Letters*, vol. 117, no. 25, p. 254002, 2020.

[67] X. Chen, R. Su, J. Liu, J. Li, and X.-H. Wang, "Scalable and highly efficient approach for an on-chip single-photon source," *Photonics Research*, vol. 10, no. 9, pp. 2066–2072, 2022.

[68] T. Lund-Hansen, S. Stobbe, B. Julsgaard, H. Thyrrestrup, T. Sünner, M. Kamp, A. Forchel, and P. Lodahl, "Experimental realization of highly efficient broadband coupling of single quantum dots to a photonic crystal waveguide," *Physical Review Letters*, vol. 101, no. 11, p. 113903, 2008.

[69] A. Schwagmann, S. Kalliakos, I. Farrer, J. P. Griffiths, G. A. Jones, D. A. Ritchie, and A. J. Shields, "On-chip single photon emission from an integrated semiconductor quantum dot into a photonic crystal waveguide," *Applied Physics Letters*, vol. 99, no. 26, p. 261108, 2011.

[70] M. Arcari, I. Söllner, A. Javadi, S. L. Hansen, S. Mahmoodian, J. Liu, H. Thyrrestrup, E. H. Lee, J. D. Song, S. Stobbe, and P. Lodahl, "Near-unity coupling efficiency of a quantum emitter to a photonic crystal waveguide," *Physical Review Letters*, vol. 113, no. 9, p. 093603, 2014.

[71] I. Söllner, S. Mahmoodian, S. L. Hansen, L. Midolo, A. Javadi, G. Kiršanskė, T. Pregnolato, H. El-Ella, E. H. Lee, J. D. Song, S. Stobbe, and P. Lodahl, "Deterministic photon–emitter coupling in chiral photonic circuits," *Nature Nanotechnology*, vol. 10, no. 9, pp. 775–778, 2015.

[72] S. J. McNab, N. Moll, and Y. A. Vlasov, "Ultra-low loss photonic integrated circuit with membrane-type photonic crystal waveguides," *Optics Express*, vol. 11, no. 22, pp. 2927–2939, 2003.

[73] M. Pu, L. Ottaviano, E. Semenova, and K. Yvind, "Efficient frequency comb generation in algaas-on-insulator," *Optica*, vol. 3, no. 8, pp. 823–826, 2016.

[74] H. Inoue, K. Hiruma, K. Ishida, T. Asai, and H. Matsumura, "Low loss GaAs optical waveguides," *IEEE Transactions on Electron Devices*, vol. 32, no. 12, pp. 2662–2668, 1985.

[75] P. Stepanov, A. Delga, X. Zang, J. Bleuse, E. Dupuy, E. Peinke, P. Lalanne, J.-M. Gérard, and J. Claudon, "Quantum dot spontaneous emission control in a ridge waveguide," *Applied Physics Letters*, vol. 106, no. 4, p. 041112, 2015.

[76] S. Hepp, F. Hornung, S. Bauer, E. Hesselmeier, X. Yuan, M. Jetter, S. L. Portalupi, A. Rastelli, and P. Michler, "Purcell-enhanced single-photon emission from a strain-tunable quantum dot in a cavity-waveguide device," *Applied Physics Letters*, vol. 117, no. 25, p. 254002, 2020.

[77] U. M. Gür, Y. Yang, J. Schall, R. Schmidt, A. Kaganskiy, Y. Wang, L. Vannucci, M. Mattes, S. Arslanagić, S. Reitzenstein, and N. Gregersen, "Design and fabrication of ridge waveguide-based nanobeam cavities for on-chip single-photon sources," *Optics Express*, vol. 30, no. 7, pp. 11973–11985, 2022.

[78] P. Lalanne, S. Mias, and J.-P. Hugonin, "Two physical mechanisms for boosting the quality factor to cavity volume ratio of photonic crystal microcavities," *Optics Express*, vol. 12, no. 3, pp. 458–467, 2004.

[79] M. Lermer, N. Gregersen, F. Dunzer, S. Reitzenstein, S. Höfling, J. Mørk, L. Worschech, M. Kamp, and A. Forchel, "Bloch-wave engineering of quantum dot micropillars for cavity quantum electrodynamics experiments," *Phys. Rev. Lett.*, vol. 108, p. 057402, Jan 2012.

[80] C. Errando-Herranz, E. Schöll, R. Picard, M. Laini, S. Gyger, A. W. Elshaari, A. Branny, U. Wennberg, S. Barbat, T. Renaud, *et al.*, "Resonance fluorescence from waveguide-coupled, strain-localized, two-dimensional quantum emitters," *ACS photonics*, vol. 8, no. 4, pp. 1069–1076, 2021.

[81] X.-J. Liu, Y. Yu, D. Liu, Q.-L. Cui, X. Qi, Y. Chen, G. Qu, L. Song, G.-P. Guo, G.-C. Guo, *et al.*, "Coupling of photon emitters in monolayer ws2 with a photonic waveguide based on bound states in the continuum," *Nano Letters*, vol. 23, no. 8, pp. 3209–3216, 2023.

[82] R. Warburton, C. Schäflein, D. Haft, F. Bickel, A. Lorke, K. Karrai, J. Garcia, W. Schoenfeld, and P. Petroff, "Optical emission from a charge-tunable quantum ring," *Nature*, vol. 405, pp. 926–929, June 2000.

[83] M. C. Löbl, I. Söllner, A. Javadi, T. Pregnolato, R. Schott, L. Midolo, A. V. Kuhlmann, S. Stobbe, A. D. Wieck, P. Lodahl, *et al.*, "Narrow optical linewidths and spin pumping on charge-tunable close-to-surface self-assembled quantum dots in an ultrathin diode," *Physical Review B*, vol. 96, no. 16, p. 165440, 2017.

[84] J. Q. Grim, A. S. Bracker, M. Zalalutdinov, S. G. Carter, A. C. Kozen, M. Kim, C. S. Kim, J. T. Mlack, M. Yakes, B. Lee, *et al.*, "Scalable in operando strain tuning in nanophotonic waveguides enabling three-quantum-dot superradiance," *Nature materials*, vol. 18, no. 9, pp. 963–969, 2019.

[85] A. V. Kuhlmann, J. H. Prechtel, J. Houel, A. Ludwig, D. Reuter, A. D. Wieck, and R. J. Warburton, "Transform-limited single photons from a single quantum dot," *Nature Communications*, vol. 6, sep 2015.

[86] L. Zhai, M. C. Löbl, G. N. Nguyen, J. Ritzmann, A. Javadi, C. Spinnler, A. D. Wieck, A. Ludwig, and R. J. Warburton, "Low-noise GaAs quantum dots for quantum photonics," *Nature Communications*, vol. 11, sep 2020.

[87] W. Yujing, P. Claudia, J. Martin, V. Luca, B. Sven, M. Battulga, and N. Gregersen, "The tunable quantum-dot-based single-photon source: Strategies for implementing electrical contact," *Manuscript in preparation*, 2023.

[88] B. J. Riel, "An introduction to self-assembled quantum dots," *American Journal of Physics*, vol. 76, no. 8, pp. 750–757, 2008.

[89] P. Lodahl, S. Mahmoodian, and S. Stobbe, "Interfacing single photons and single quantum dots with photonic nanostructures," *Reviews of Modern Physics*, vol. 87, no. 2, p. 347, 2015.

[90] D. G. Gevaux, A. J. Bennett, R. M. Stevenson, A. J. Shields, P. Atkinson, J. Griffiths, D. Anderson, G. A. C. Jones, and D. A. Ritchie, "Enhancement and suppression of spontaneous emission by temperature tuning inas quantum dots to photonic crystal cavities," *Applied Physics Letters*, vol. 88, no. 13, p. 131101, 2006.

[91] A. Faraon and J. Vučković, "Local temperature control of photonic crystal devices via micron-scale electrical heaters," *Applied Physics Letters*, vol. 95, no. 4, p. 043102, 2009.

[92] R. Katsumi, Y. Ota, A. Osada, T. Tajiri, T. Yamaguchi, M. Kakuda, S. Iwamoto, H. Akiyama, and Y. Arakawa, "In situ wavelength tuning of quantum-dot single-photon sources integrated on a cmos-processed silicon waveguide," *Applied Physics Letters*, vol. 116, no. 4, 2020.

[93] H. Kim, T. C. Shen, D. Sridharan, G. S. Solomon, and E. Waks, "Magnetic field tuning of a quantum dot strongly coupled to a photonic crystal cavity," *Applied Physics Letters*, vol. 98, no. 9, p. 091102, 2011.

[94] J. Beetz, T. Braun, C. Schneider, S. Höfling, and M. Kamp, "Anisotropic strain-tuning of quantum dots inside a photonic crystal cavity," *Semiconductor Science and Technology*, vol. 28, p. 122002, nov 2013.

[95] M. Moczała-Dusanowska, Ł. Dusanowski, S. Gerhardt, Y. M. He, M. Reindl, A. Rastelli, R. Trotta, N. Gregersen, S. Höfling, and C. Schneider, "Strain-tunable single-photon source based on a quantum dot–micropillar system," *ACS Photonics*, vol. 6, no. 8, pp. 2025–2031, 2019.

[96] M. Moczała-Dusanowska, Ł. Dusanowski, O. Iff, T. Huber, S. Kuhn, T. Czyszanowski, C. Schneider, and S. Höfling, "Strain-tunable single-photon source based on a circular bragg grating cavity with embedded quantum dots," *ACS Photonics*, vol. 7, no. 12, pp. 3474–3480, 2020.

[97] P. W. Fry, I. E. Itskevich, D. J. Mowbray, M. S. Skolnick, J. J. Finley, J. A. Barker, E. P. O'Reilly, L. R. Wilson, I. A. Larkin, P. A. Maksym, M. Hopkinson, M. Al-Khafaji, J. P. R. David, A. G. Cullis, G. Hill, and J. C. Clark, "Inverted electron-hole alignment in inas-gaas self-assembled quantum dots," *Phys. Rev. Lett.*, vol. 84, pp. 733–736, Jan 2000.

[98] B. Alén, F. Bickel, K. Karrai, R. J. Warburton, and P. M. Petroff, "Stark-shift modulation absorption spectroscopy of single quantum dots," *Applied Physics Letters*, vol. 83, no. 11, pp. 2235–2237, 2003.

[99] M. J. Fernée, H. Rubinsztein-Dunlop, and G. Milburn, "Improving single-photon sources with stark tuning," *Physical Review A*, vol. 75, no. 4, p. 043815, 2007.

[100] A. Laucht, F. Hofbauer, N. Hauke, J. Angele, S. Stobbe, M. Kaniber, G. Böhm, P. Lodahl, M.-C. Amann, and J. J. Finley, "Electrical control of spontaneous emission and strong coupling for a single quantum dot," *New Journal of Physics*, vol. 11, p. 023034, feb 2009.

[101] S. M. Thon, H. Kim, C. Bonato, J. Gudat, J. Hagemeier, P. M. Petroff, and D. Bouwmeester, "Independent electrical tuning of separated quantum dots in coupled photonic crystal cavities," *Applied Physics Letters*, vol. 99, no. 16, p. 161102, 2011.

[102] A. J. Bennett, R. B. Patel, J. Skiba-Szymanska, C. A. Nicoll, I. Farrer, D. A. Ritchie, and A. J. Shields, "Giant stark effect in the emission of single semiconductor quantum dots," *Applied Physics Letters*, vol. 97, no. 3, p. 031104, 2010.

[103] R. Trotta, E. Zallo, E. Magerl, O. G. Schmidt, and A. Rastelli, "Independent control of exciton and biexciton energies in single quantum dots via electroelastic fields," *Phys. Rev. B*, vol. 88, p. 155312, Oct 2013.

[104] J. Aberl, P. Klenovský, J. S. Wildmann, J. Martín-Sánchez, T. Fromherz, E. Zallo, J. Humlíček, A. Rastelli, and R. Trotta, "Inversion of the exciton built-in dipole moment in in(ga)as quantum dots via nonlinear piezoelectric effect," *Phys. Rev. B*, vol. 96, p. 045414, Jul 2017.

[105] T. Heindel, C. Schneider, M. Lermer, S. H. Kwon, T. Braun, S. Reitzenstein, S. Höfling, M. Kamp, and A. Forchel, "Electrically driven quantum dot-micropillar single photon source with 34% overall efficiency," *Applied Physics Letters*, vol. 96, 2010.

[106] A. K. Nowak, S. L. Portalupi, V. Giesz, O. Gazzano, C. D. Savio, P. F. Braun, K. Karrai, C. Arnold, L. Lanco, I. Sagnes, A. Lemaître, and P. Senellart, "Deterministic and electrically tunable bright single-photon source," *Nature Communications*, vol. 5, 2 2014.

[107] T. Grange, N. Somaschi, C. Antón, L. De Santis, G. Coppola, V. Giesz, A. Lemaître, I. Sagnes, A. Auffèves, and P. Senellart, "Reducing phonon-induced decoherence in solid-state single-photon sources with cavity quantum electrodynamics," *Physical review letters*, vol. 118, no. 25, p. 253602, 2017.

[108] T. B. Hoang, J. Beetz, M. Lermer, L. Midolo, M. Kamp, S. Höfling, and A. Fiore, "Widely tunable, efficient on-chip single photon sources at telecommunication wavelengths," *Optics express*, vol. 20, no. 19, pp. 21758–21765, 2012.

[109] F. Liu, A. J. Brash, J. O'Hara, L. M. Martins, C. L. Phillips, R. J. Coles, B. Royall, E. Clarke, C. Bentham, N. Prtljaga, *et al.*, "High purcell factor generation of indistinguishable on-chip single photons," *Nature nanotechnology*, vol. 13, no. 9, pp. 835–840, 2018.

[110] J. L. O'Brien, "Optical quantum computing," *Science*, vol. 318, no. 5856, pp. 1567–1570, 2007.

[111] R. Patel, A. Bennett, I. Farrer, C. Nicoll, D. Ritchie, and A. Shields, "Two-photon interference of the emission from electrically tunable remote quantum dots," *Nature Photonics*, vol. 4, 07 2010.

[112] M. Pont, S. Thomas, I. M. de Buy Wenniger, A. Harouri, A. Lemaitre, I. Sagnes, N. Somaschi, and P. Senellart, "Two-photon interference with bright remote quantum dot sources," in *Quantum Information and Measurement*, pp. Tu2B–4, Optica Publishing Group, 2021.

[113] M. Pont, R. Albiero, S. E. Thomas, N. Spagnolo, F. Ceccarelli, G. Corrielli, A. Brieussel, N. Somaschi, H. Huet, A. Harouri, *et al.*, "Quantifying n-photon indistinguishability with a cyclic integrated interferometer," *Physical Review X*, vol. 12, no. 3, p. 031033, 2022.

[114] X.-L. Chu, C. Papon, N. Bart, A. D. Wieck, A. Ludwig, L. Midolo, N. Rotenberg, and P. Lodahl, "Independent electrical control of two quantum dots coupled through a photonic-crystal waveguide," *arXiv preprint arXiv:2303.00345*, 2023.

[115] C. Papon, Y. Wang, R. Uppu, S. Scholz, A. D. Wieck, A. Ludwig, P. Lodahl, and L. Midolo, "Independent operation of two waveguide-integrated single-photon sources," *arXiv preprint arXiv:2210.09826*, 2022.

[116] L. Novotny and B. Hecht, *Principles of nano-optics*. Cambridge university press, 2012.

[117] L. E. Ballentine, *Quantum mechanics: a modern development*. World Scientific Publishing Company, 2014.

[118] J. R. de Lasson, P. T. Kristensen, J. Mørk, and N. Gregersen, "Semi-analytical quasi-normal mode theory for the local density of states in coupled photonic crystal cavity–waveguide structures," *Optics Letters*, vol. 40, no. 24, pp. 5790–5793, 2015.

[119] S. Stobbe, P. T. Kristensen, J. E. Mortensen, J. M. Hvam, J. Mørk, and P. Lodahl, "Spontaneous emission from large quantum dots in nanostructures: Exciton-photon interaction beyond the dipole approximation," *Physical Review B*, vol. 86, no. 8, p. 085304, 2012.

[120] M. L. Andersen, S. Stobbe, A. S. Sørensen, and P. Lodahl, "Strongly modified plasmon–matter interaction with mesoscopic quantum emitters," *Nature Physics*, vol. 7, no. 3, pp. 215–218, 2011.

[121] P. Tighineanu, A. S. Sørensen, S. Stobbe, and P. Lodahl, "Unraveling the mesoscopic character of quantum dots in nanophotonics," *Physical Review Letters*, vol. 114, no. 24, p. 247401, 2015.

[122] A. V. Lavrinenko, J. Lægsgaard, N. Gregersen, F. Schmidt, and T. Søndergaard, *Numerical methods in photonics*. CRC press, 2018.

[123] G. Lecamp, J.-P. Hugonin, and P. Lalanne, "Theoretical and computational concepts for periodic optical waveguides," *Optics express*, vol. 15, no. 18, pp. 11042–11060, 2007.

[124] C. A. Balanis, *Antenna theory: analysis and design*. John wiley & sons, 2016.

[125] A. D. Østerkryger, *Engineering of nanophotonic structures for quantum information applications.* PhD thesis, Technical University of Denmark, DTU, 2018.

[126] J. Pomplun, S. Burger, L. Zschiedrich, and F. Schmidt, "Adaptive finite element method for simulation of optical nano structures," *physica status solidi (b)*, vol. 244, no. 10, pp. 3419–3434, 2007.

[127] J. Pomplun, S. Burger, F. Schmidt, A. Schliwa, D. Bimberg, A. Pietrzak, H. Wenzel, and G. Erbert, "Finite element simulation of the optical modes of semiconductor lasers," *physica status solidi (b)*, vol. 247, no. 4, pp. 846–853, 2010.

[128] S. Burger, F. Schmidt, and L. Zschiedrich, "Numerical investigation of photonic crystal microcavities in silicon-on-insulator waveguides," in *Photonic and Phononic Crystal Materials and Devices X*, vol. 7609, pp. 284–290, SPIE, 2010.

[129] J.-M. Jin, *The finite element method in electromagnetics*. John Wiley & Sons, 2015.

[130] A. C. Polycarpou, *Introduction to the finite element method in electromagnetics*. Springer Nature, 2022.

[131] C. Sauvan, J.-P. Hugonin, I. S. Maksymov, and P. Lalanne, "Theory of the spontaneous optical emission of nanosize photonic and plasmon resonators," *Physical Review Letters*, vol. 110, no. 23, p. 237401, 2013.

[132] B.-Y. Wang, E. V. Denning, U. M. Gür, C.-Y. Lu, and N. Gregersen, "Micropillar single-photon source design for simultaneous near-unity efficiency and indistinguishability," *Physical Review B*, vol. 102, no. 12, p. 125301, 2020.

[133] M. A. Jacobsen, Y. Wang, L. Vannucci, J. Claudon, J.-M. Gérard, and N. Gregersen, "Performance of the nanopost single-photon source: beyond the single-mode model," *Nanoscale*, vol. 15, pp. 6156–6169, 2023.

[134] W. B. Jeon, J. S. Moon, K.-Y. Kim, Y.-H. Ko, C. J. Richardson, E. Waks, and J.-H. Kim, "Plug-and-play single-photon devices with efficient fiber-quantum dot interface," *Advanced Quantum Technologies*, vol. 5, no. 10, p. 2200022, 2022.

[135] S. Xia, T. Aoki, K. Gao, M. Arita, Y. Arakawa, and M. J. Holmes, "Enhanced single-photon emission from gan quantum dots in bullseye structures," *ACS Photonics*, vol. 8, no. 6, pp. 1656–1661, 2021.

[136] N. Gregersen, D. P. McCutcheon, J. Mørk, J.-M. Gérard, and J. Claudon, "A broadband tapered nanocavity for efficient nonclassical light emission," *Optics Express*, vol. 24, no. 18, pp. 20904–20924, 2016.

[137] L. Sapienza, M. Davanço, A. Badolato, and K. Srinivasan, "Nanoscale optical positioning of single quantum dots for bright and pure single-photon emission," *Nature communications*, vol. 6, no. 1, p. 7833, 2015.

[138] S. Kotal, A. Artioli, Y. Wang, A. D. Osterkryger, M. Finazzer, R. Fons, Y. Genuist, J. Bleuse, J.-M. Gérard, N. Gregersen, *et al.*, "A nanowire optical nanocavity for broadband enhancement of spontaneous emission," *Applied Physics Letters*, vol. 118, no. 19, p. 194002, 2021.

[139] J. R. de Lasson, P. T. Kristensen, J. Mørk, and N. Gregersen, "Semianalytical quasi-normal mode theory for the local density of states in coupled photonic crystal cavity–waveguide structures," *Opt. Lett.*, vol. 40, pp. 5790–5793, Dec 2015.

[140] H. Wang, H. Hu, T.-H. Chung, J. Qin, X. Yang, J.-P. Li, R.-Z. Liu, H.-S. Zhong, Y.-M. He, X. Ding, *et al.*, "On-demand semiconductor source of entangled photons which simultaneously has high fidelity, efficiency, and indistinguishability," *Physical review letters*, vol. 122, no. 11, p. 113602, 2019.

[141] P.-I. Schneider, N. Srocka, S. Rodt, L. Zschiedrich, S. Reitzenstein, and S. Burger, "Numerical optimization of the extraction efficiency of a quantum-dot based single-photon emitter into a single-mode fiber," *Optics Express*, vol. 26, no. 7, pp. 8479–8492, 2018.

[142] N. Moll, T. Stöferle, S. Schönenberger, and R. F. Mahrt, "Ultra-high quality-factor resonators with perfect azimuthal modal-symmetry," *Optics Express*, vol. 17, no. 23, pp. 20998–21006, 2009.

[143] S. Seyfferle, T. Herzog, R. Sittig, M. Jetter, S. L. Portalupi, and P. Michler, "Wavelength-tunable open double-microcavity to enhance two closely spaced optical transitions," *arXiv preprint arXiv:2208.14790*, 2022.

[144] T. Herzog, S. Böhrkircher, S. Both, M. Fischer, R. Sittig, M. Jetter, S. Portalupi, T. Weiss, and P. Michler, "Realization of a tunable fiber-based double cavity system," *Physical Review B*, vol. 102, no. 23, p. 235306, 2020.

[145] Y. Wang, L. Vannucci, S. Burger, and N. Gregersen, "Near-unity efficiency in ridge waveguide-based, on-chip single-photon sources," *Materials for Quantum Technology*, vol. 2, no. 4, p. 045004, 2022.

[146] DTU Computing Center, "DTU Computing Center resources," 2022.

[147] P. Lodahl, S. Mahmoodian, and S. Stobbe, "Interfacing single photons and single quantum dots with photonic nanostructures," *Rev. Mod. Phys.*, vol. 87, pp. 347–400, May 2015.

[148] T. Hoehne, P. Schnauber, S. Rodt, S. Reitzenstein, and S. Burger, "Numerical investigation of light emission from quantum dots embedded into on-chip, low-index-contrast optical waveguides," *Physica Status Solidi (b)*, vol. 256, no. 7, p. 1800437, 2019.

[149] J. D. Joannopoulos, S. G. Johnson, J. N. Winn, and R. D. Meade, "Molding the flow of light," *Princeton Univ. Press, Princeton, NJ*, 2008.

[150] M. Palamaru and P. Lalanne, "Photonic crystal waveguides: Out-of-plane losses and adiabatic modal conversion," *Applied Physics Letters*, vol. 78, no. 11, pp. 1466–1468, 2001.

[151] P. Lalanne and J.-P. Hugonin, "Bloch-wave engineering for high-Q, small-V microcavities," *IEEE Journal of Quantum Electronics*, vol. 39, no. 11, pp. 1430–1438, 2003.

[152] W. Xie, P. Verheyen, M. Pantouvaki, J. Van Campenhout, and D. Van Thourhout, "Efficient resonance management in ultrahigh-Q 1d photonic crystal nanocavities fabricated on 300 mm SOI CMOS platform," *Laser & Photonics Reviews*, vol. 15, no. 2, p. 2000317, 2021.

[153] B. Aslan, M. Deng, and T. F. Heinz, "Strain tuning of excitons in monolayer wse 2," *Physical Review B*, vol. 98, no. 11, p. 115308, 2018.

[154] H. Wang, W. Li, X. Jiang, Y.-M. He, Y.-H. Li, X. Ding, M.-C. Chen, J. Qin, C.-Z. Peng, C. Schneider, M. Kamp, W.-J. Zhang, H. Li, L.-X. You, Z. Wang, J. P. Dowling, S. Höfling, C.-Y. Lu, and J.-W. Pan, "Toward scalable boson sampling with photon loss," *Phys. Rev. Lett.*, vol. 120, p. 230502, Jun 2018.

[155] N. Spagnolo, C. Vitelli, M. Bentivegna, D. J. Brod, A. Crespi, F. Flamini, S. Giacomini, G. Milani, R. Ramponi, P. Mataloni, R. Osellame, E. F. Galvão, and F. Sciarrino, "Experimental validation of photonic boson sampling," *Nature Photonics*, vol. 8, pp. 615–620, jun 2014.

[156] E. Diamanti, H.-K. Lo, B. Qi, and Z. Yuan, "Practical challenges in quantum key distribution," *npj Quantum Information*, vol. 2, no. 1, pp. 1–12, 2016.

[157] Y. Chen, T. R. Nielsen, N. Gregersen, P. Lodahl, and J. Mørk, "Finite-element modeling of spontaneous emission of a quantum emitter at nanoscale proximity to plasmonic waveguides," *Phys. Rev. B*, vol. 81, p. 125431, Mar 2010.

[158] S. Ji, T. Tajiri, H. Kiyama, A. Oiwa, and S. Iwamoto, "Design of bull's-eye optical cavity toward efficient quantum media conversion using gate-defined quantum dot," *Japanese Journal of Applied Physics*, vol. 60, Oct. 2021. Publisher Copyright: © 2021 The Japan Society of Applied Physics.

[159] S. A. Blokhin, M. A. Bobrov, N. A. Maleev, J. N. Donges, L. Bremer, A. A. Blokhin, A. P. Vasil'ev, A. G. Kuzmenkov, E. S. Kolodeznyi, V. A. Shchukin, N. N. Ledentsov, S. Reitzenstein, and V. M. Ustinov, "Design optimization for bright electrically-driven quantum dot single-photon sources emitting in telecom o-band," *Optics Express*, vol. 29, p. 6582, 3 2021.

[160] N. Gregersen, T. R. Nielsen, J. Mørk, J. Claudon, and J.-M. Gérard, "Designs for high-efficiency electrically pumped photonic nanowire single-photon sources," *Opt. Express*, vol. 18, pp. 21204–21218, Sep 2010.

[161] N. Gregersen, P. Kaer, and J. Mørk, "Modeling and design of high-efficiency single-photon sources," *IEEE Journal of Selected Topics in Quantum Electronics*, vol. 19, no. 5, pp. 1–16, 2013.

[162] A. Barbiero, J. Huwer, J. Skiba-Szymanska, T. Müller, R. M. Stevenson, and A. J. Shields, "Design study for an efficient semiconductor quantum light source operating in the telecom c-band based on an electrically-driven circular bragg grating," *Optics Express*, vol. 30, p. 10919, 3 2022.

[163] N. Somaschi, V. Giesz, L. D. Santis, J. C. Loredo, M. P. Almeida, G. Hornecker, S. L. Portalupi, T. Grange, C. Antón, J. Demory, C. Gómez, I. Sagnes, N. D. Lanzillotti-Kimura, A. Lemaítre, A. Auffeves, A. G. White, L. Lanco, and P. Senellart, "Near-optimal single-photon sources in the solid state," *Nature Photonics*, vol. 10, pp. 340–345, 5 2016.

[164] S. Kotal, A. Artioli, Y. Wang, A. Osterkryger, M. Finazzer, R. Fons, Y. Genuist, J. Bleuse, J.-M. Gérard, N. Gregersen, and J. Claudon, "A nanowire optical nanocavity for broadband enhancement of spontaneous emission," *Applied Physics Letters*, vol. 118, p. 194002, 05 2021.

[165] M. Munsch, N. S. Malik, E. Dupuy, A. Delga, J. Bleuse, J.-M. Gérard, J. Claudon, N. Gregersen, and J. Mørk, "Dielectric gaas antenna ensuring an efficient broadband coupling between an inas quantum dot and a gaussian optical beam," *Phys. Rev. Lett.*, vol. 110, p. 177402, Apr 2013.

[166] J. Claudon, N. Gregersen, P. Lalanne, and J.-M. Gérard, "Harnessing light with photonic nanowires: Fundamentals and applications to quantum optics," *ChemPhysChem*, vol. 14, no. 11, pp. 2393–2402, 2013.

[167] M. A. Jacobsen, Y. Wang, L. Vannucci, J. Claudon, J.-M. Gérard, and N. Gregersen, "Performance of the nanopost single-photon source: beyond the single-mode model," 2023.

[168] J. Schall, M. Deconinck, N. Bart, M. Florian, M. von Helversen, C. Dangel, R. Schmidt, L. Bremer, F. Bopp, I. Hüllen, C. Gies, D. Reuter, A. D. Wieck, S. Rodt, J. J. Finley, F. Jahnke, A. Ludwig, and S. Reitzenstein, "Bright electrically controllable quantum-dot-molecule devices fabricated by in situ electron-beam lithography," *Advanced Quantum Technologies*, vol. 4, 6 2021.

[169] Q. Buchinger, S. Betzold, S. Höfling, and T. Huber-Loyola, "Optical properties of circular bragg gratings with labyrinth geometry to enable electrical contacts," *Applied Physics Letters*, vol. 122, no. 11, 2023.

{2.7182818284}ϑφερτυθιοπσδφγηξκλ